

AN ADAPTIVE DUAL-OPTIMAL PATH-PLANNING TECHNIQUE  
FOR UNMANNED AIR VEHICLES  
WITH APPLICATION TO  
SOLAR-REGENERATIVE HIGH ALTITUDE LONG ENDURANCE FLIGHT

Dissertation

Presented in Partial Fulfillment of the Requirements for  
the Degree Doctor of Philosophy in the  
Graduate School of The Ohio State University

By

Clifford A. Whitfield  
B.Sc. A.A.E., M.Sc. A.A.E.

\*\*\*\*\*

The Ohio State University  
2009

Examination Committee:

G. M. Gregorek, Advisor  
J. N. Scott  
R. J. Freuler  
C. E. Hall  
J. W. Gregory

Approved By:

---

Advisor  
Aeronautical and Astronautical  
Engineering Graduate Program

Copyright<sup>©</sup> By  
C. A. Whitfield  
2009

## ABSTRACT

A multi-objective technique for Unmanned Air Vehicle (UAV) path and trajectory autonomy generation, through task allocation and sensor fusion has been developed. The Dual-Optimal Path-Planning (D-O.P-P.) Technique generates on-line adaptive flight paths for UAVs based on available flight windows and environmental influenced objectives. The environmental influenced optimal condition, known as the ‘driver’ determines the condition, within a downstream virtual window of possible vehicle destinations and orientation built from the UAV kinematics. The intermittent results are pursued by a dynamic optimization technique to determine the flight path. This sequential optimization technique is a multi-objective optimization procedure consisting of two goals, without requiring additional information to combine the conflicting objectives into a single-objective. An example case-study and additional applications are developed and the results are discussed; including the application to the field of Solar Regenerative (SR) High Altitude Long Endurance (HALE) UAV flight.

Harnessing solar energy has recently been adapted for use on high altitude UAV platforms. An aircraft that uses solar panels and powered by the sun during the day and through the night by SR systems, in principle could sustain flight for weeks or months. The requirements and limitations of solar powered flight were determined. The SR-HALE UAV platform geometry and flight characteristics were selected from an existing aircraft that has demonstrated the capability for sustained flight through flight tests. The goals were to maintain continual Situational Awareness (SA) over a case-study selected Area of Interest (AOI) and existing UAV power and surveillance systems. This was done for still wind and constant wind conditions at altitude along with variations in latitude.

The characteristics of solar flux and the dependence on the surface location and orientation were established along with fixed flight maneuvers for the SR-HALE UAV.

A sustained turn circle flight pattern, common for vehicles in loiter was selected as a baseline for comparisons.

The objectives of the D-O.P.P. Technique for SR-HALE flight were to determine the minimum required power flight paths to the predetermined location and orientation for obtaining maximum solar flux established by the ‘driver.’ The on-line path generation technique prolonged the flight duration, over the baseline by approximately two months for a year of flight over the case-study AOI. This prolonged flight was consistent for all latitude locations, including two months of available flight at 60 degree latitude – where sustained turn baseline flight was no longer capable. This was possible by increasing the total solar power by as much as 28% while decreasing the averaged power required for flight.

## Dedication

To my family

(and in memory of Sue Holtom)

## ACKNOWLEDGMENTS

I express my sincerest gratitude toward my advisor Dr. G.M. Gregorek as well as Dr. R.J. Freuler. Thank you both for providing opportunities, time, and the trust for me to gain valuable experiences in and out of the laboratory. I cannot express my gratitude enough. This also applies to Dr. J. Lee. Thank you. Acknowledgements are due to the rest of my committee, Dr. C.E. Hall, Dr. J.N. Scott, and Dr. J.W. Gregory. Thank you for your valuable help and guidance for the completion of this research.

I am deeply thankful to my family for providing a welcoming sounding board and an important source for advice during my academic career. I also cannot express my gratitude enough.

And to the rest of the OSU and AARL faculty, staff, and students that I have had the privilege to work with and learn from, thank you.

## VITA

February 12, 1981	Born, Salem Ohio, USA
June – 2004	B.Sc., Aerospace Engineering, The Ohio State University
June – 2006	M.Sc., Aerospace Engineering The Ohio State University
Jan – June – 2006	Lecturer / Lab Instructor, Aeronautical and Astronautical Engineering, The Ohio State University
September 2004 – Present	Graduate Research / Teaching Associate, Aeronautical and Astronautical Engineering, The Ohio State University
March 2005 – Present	Aircraft Design and Test Engineer Consultant, Whitfield Aerospace LLC. Columbus, OH

## PUBLICATIONS

1. Whitfield, C.A., Roscoe, J., Freuler, R.J. “General Electric Aircraft Engines (GEAC) & Japan Air Lines (JAL) 1/13.86 Scaled Jet Engine Test Cell”, Phase 1 Final Report. The Ohio State University Aeronautical and Astronautical Engineering Department; September, 2008.
2. Pearson, J., Gregorek, G.M., Whitfield, C.A., “High Altitude Morphing Aircraft (HAMAC)” AFRL-VA-WP-TR-2007-XXX– Final Report to USAF for Phase I Small Business Initiative, 2007.
3. Whitfield, C.A., “Experimental Development and Investigations of Propeller / Jet Engine Interactions” The Ohio State University Aeronautical and Astronautical Engineering Department; June, 2006.

4. Whitfield, C.A., Stevens, K., “Experimental Development and Investigations of Propeller/Jet Engine Interactions and Computational Development and Analysis of Pratt and Whitney 306B Flight Nacelle” Final Report – Orion America Technologies LLC; March 30, 2006.
5. Gregorek, G.M., Hall, C.E., Whitfield, C.A., Stevens, K., “Experimental Development and Investigations of Propeller/Jet Engine Interactions and Computational Development and Analysis of Pratt and Whitney 306B Flight Nacelle” Final Report – DOD and Snow Aviation International Inc.; March 30, 2006.
6. Whitfield, C.A., and Freuler, R.J.: "Progress Report On the GE90-115B Anti-Reingestion Tunnel Program", Interim report for OSURF Project No. 746645 to GE Aircraft Engines, The Ohio State University Research Foundation, Columbus, Ohio, January 2005
7. Janiszewska, J.M., Whitfield, C.A., and Freuler, R.J.: "Scale Model Test of the LM6000 with VBV Collector", Final report for OSURF Project No. 60002993 to GE Aircraft Engines, The Ohio State University Research Foundation, Columbus, Ohio, September 2005.

## FIELDS OF STUDY

Major Field: Aeronautical and Astronautical Engineering



## TABLE OF CONTENTS

ABSTRACT .....	ii
DEDICATION .....	iv
ACKNOWLEDGMENTS .....	v
VITA .....	vi
LIST OF FIGURES .....	x
LIST OF TABLES .....	xii
NOMENCLATURE .....	xiii

### CHAPTERS:

1. INTRODUCTION .....	1
1.1 Objective .....	4
1.2 Background .....	4
1.3 Current Multi-Objective Procedures .....	5
1.3.1 SR-HALE Applications .....	7
2. DUAL-OPTIMAL PATH-PLANNING TECHNIQUE .....	8

	<i>CASE STUDY: <u>SOLAR POWERED UAV FLIGHT</u></i> .....	12
3.	SR-HALE UAV REQUIREMENTS AND LIMITATIONS .....	14
3.1	Ephemeris .....	14
3.1.1	Equation of Time .....	14
3.1.2	Solar Coordinates .....	16
3.1.3	Daylight Hours .....	18
3.1.4	Surface Obliquity .....	20
3.2	Solar Flux .....	21
3.3	Solar Energy – Photovoltaics .....	24
3.4	Systems .....	28
3.4.1	Electric Motor .....	28
3.4.2	Energy Storage .....	28
3.4.3	Surveillance .....	30
3.5	High Altitude Winds .....	32
3.6	SR-HALE Platform .....	34
4.	SR-HALE UAV FLIGHT MANEUVERING PATTERNS .....	39
4.1	Fixed Flight Maneuvers .....	39
4.1.1	Static On-Station .....	39
4.1.2	Sustained Turn .....	48
4.2	Optimum Flight Maneuvering .....	55
4.2.1	UAV Kinematics .....	55
4.2.2	D-O.P-P. Modeling & Procedure .....	56
4.3	Results & Discussion .....	62
4.3.1	High Altitude Wind Effects .....	72
4.4	SR-HALE UAV D-O.P-P. Summary .....	73
5.	ADDITIONAL D-O.P-P. TECHNIQUE APPLICATIONS .....	76
5.1	Cooperative Tactics .....	76
5.2	Dynamic Target Pursuit .....	77
5.3	Threat Evasion .....	79
6.	SUMMARY AND CONCLUSION .....	80
	LIST OF REFERENCES .....	84
	APPENDIX .....	90

## LIST OF FIGURES

Figure 2.1: D-O.P-P. Flight Maneuvering Window (2-D) .....	10
Figure 2.2: D-O.P-P. Flight Maneuvering Window (3-D) .....	11
Figure 3.1: Equation of Time .....	15
Figure 3.2: Hours of Daylight at Latitude .....	19
Figure 3.3: Solar Flux with Surface Orientation at 60,000' .....	23
Figure 3.4: Solar Cell Array Characteristic Curves at 60,000' .....	27
Figure 3.5: Energy Storage System Mass Requirements @ 3000W Draw.	29
Figure 3.6: Case-Study Range-of-Sight for Area of Interest .....	31
Figure 3.7: Case-Study AOI Wind Roses .....	33
Figure 3.8: SR-HALE Aerodynamic Characteristics .....	36
Figure 3.9: SR-HALE Aerodynamic Efficiency Characteristics .....	37
Figure 4.1: Static On-Station Solar Flux Variation at 40 <sup>0</sup> Latitude: North.	40
Figure 4.2: Static On-Station Solar Flux Variation at 40 <sup>0</sup> Latitude: South.	41
Figure 4.3: Static On-Station Solar Flux Variation at 40 <sup>0</sup> Latitude: West..	42
Figure 4.4: Static On-Station Solar Flux Variation with Latitude: North...	43
Figure 4.5: Static On-Station Solar Flux Variation with Latitude: South...	44
Figure 4.6: Static On-Station Solar Flux Variation with Latitude: West...	45
Figure 4.7: Static On-Station Total Solar Flux and Ave Power Ava.....	46
Figure 4.8: SR-HALE Static On-Station Required Power and AoA .....	47
Figure 4.9: HALE Sustained Turn Required Power .....	49
Figure 4.10: SR-HALE Minimum Sustained Turn Power Required – 50kts .....	50
Figure 4.11: Total Sustained Turn Solar Flux and Available Power .....	51
Figure 4.12: Sustained Turn Solar Flux Variations .....	53

Figure 4.13: Total Sustained Turn Solar Flux and Available Power – Latitude Variations .....	54
Figure 4.14: SR-HALE Flight Maneuvering Window and Objectives.....	57
Figure 4.15: SR-HALE D-O.P-P. Flow Chart .....	59
Figure 4.16: D-O.P-P. Example: Flight at Sunrise .....	61
Figure 4.17: D-O.P-P. Example of Local Optimality Process: Sunrise.....	62
Figure 4.18: SR-HALE D-O.P-P. Flight Pattern – Summer Solstice.....	63
Figure 4.19: D-O.P-P. Technique Solar Flux Variation – Comparisons....	64
Figure 4.20: SR-HALE D-O.P-P. 10 Minute Time Window at Solar Noon .....	65
Figure 4.21: Driver Objective Results for 10 Minute Time Window at Solar Noon .....	66
Figure 4.22: Driver Window Projection Effects on Available Power.....	67
Figure 4.23: SR-HALE UAV Averaged Power Comparison – Year over AOI .....	70
Figure 4.24: SR-HALE UAV Averaged Power Variation with Latitude...	71
Figure 4.25: D-O.P-P. High Altitude Wind Example: Flight at Sunrise...	72

## LIST OF TABLES

Table 2.1: D-O.P-P. Technique .....	9
Table 2.2: Case-Study Location .....	13
Table 3.1: Case-Study Solar Noon .....	16
Table 3.2: Case-Study Available Daylight .....	20
Table 3.3: Average High Altitude Wind Speeds (knots) .....	32
Table 3.4: Case-Study AOI Wind Speeds (knots) .....	34
Table 3.5: SR-HALE Derivatives .....	35
Table 3.6: SR-HALE Platform Performance Summary .....	38
Table 4.1: Total Sustained Turn Solar Flux with Initial Start Location.....	52
Table 4.2: SR-HALE UAV D-O.P-P. Technique .....	58
Table 4.3: Effects of Varying SR-HALE Bank Angle Limit.....	68
Table 4.4: SR-HALE Flight Maneuvering Comparisons .....	69

## NOMENCLATURE

### Parameters

k	Boltzmann's constant
p	roll
q	pitch
r	yaw
t	time
x	Cartesian coordinate x-location
y	Cartesian coordinate y-location
z	Cartesian coordinate z-location
A	Azimuth angle
AoA	Angle-of-Attack
AR	Aspect Ratio
C	Coefficient
D	Photovoltaic characteristic constant or Direction of flight
D'	Codeclination
F	Solar flux (intensity)
H	Hour angle
J	Current
$\bar{K}$	Average responsivity parameter
L'	Colatitude
P	Power
RPDL	Revolutions per Daylight
$S_0$	Solar constant
T	Total (end) time or Temperature
V	Velocity or Voltage
W	Watts
Z	Zenith angle
$\alpha$	Angle-of-attack
$\beta$	Side slip angle
$\varepsilon_g$	Photovoltaic energy gap
$\phi$	Bank angle
$\psi$	Heading angle (local)
$\mu$	Obliquity factor ( $\cos(\theta)$ )
$\mu_0$	Solar zenith angle
$\tau$	Optical thickness

$\bar{\omega}_0$	Single scattering albedo
$\delta_e$	Elevator deflection angle
$\Psi$	Heading angle (solar)
$\theta$	Surface Obliquity angle
$\Delta$	Tilt angle

### Abbreviations

deg	degree
ft	feet
hrs	hours
kft	thousand feet
kts	knots
lbs	pounds
mb	millibar
nm	nautical-mile
pv	photovoltaic
p-n	photovoltaic junction type
rev	revolutions
sq-ft	square feet
AOI	Area of Interest
AOR	Area of Responsibility
Ava	Average
CD	Cardinal Direction
DC	Direct Current
D-O.P-P.	Dual-Optimal Path-Planning
E	East
EOT	Equation of Time
Eq	Equinox
GPS	Global Positioning Sensor
HALE	High Altitude Long Endurance
HISAR	Hughes Integrated Surveillance & Reconnaissance
ISR	Intelligence Surveillance and Reconnaissance
Long	Longitude
N	North
N.H.	Northern Hemisphere
OH	Ohio
RCS	Radar Cross Section
S	South
SA	Situational Awareness
S.H.	Southern Hemisphere
SR	Solar Regenerative
SR-HALE	Solar Regenerative High Altitude Long Endurance
SS	Summer Solstice
UAS	Unmanned Aircraft System
UAV	Unmanned Air Vehicle

UCAV	Unmanned Combat Air Vehicle
W	West
WS	Winter Solstice

*Subscripts*

c	clockwise
c-c	counterclockwise
j	junction (current)
int	initial
l	roll
k	intermediate-state
m	pitch
mx	maximum
n	yaw
loc	local
noon	solar noon
oc	open circuit
rise	sunrise
s	sunrise and sunset
sc	short circuit
set	sunset
st	standard
D	Drag
A	Available
ESS	Energy Storage System
FW	Flight Window
L	Lift
W	Wind
P	Photo (current)
Y	Side force
$\beta$	side slip
$\lambda$	wavelength

*Superscripts*

0	degree
'	minute
“	second
*	optimum
(direct)	direct component
↓ (diffuse)	downward diffuse component



## CHAPTER 1

### INTRODUCTION

Unmanned Air Vehicles (UAVs) are unpiloted aircraft that are either controlled remotely or are autonomously flown based on pre-programmed flight plans. The UAV was originally classified as Unmanned Aircraft Systems (UAS), coined by the U.S. Navy and adopted by the Federal Aviation Administration (FAA); provided that the vehicles generally require external ‘systems’ such as a ground station for use. The official acronym UAS has not expanded beyond the military circles, however, the term UAV, during their unprecedented growing rate and role expansion has become a common and popular handle. In 2005 alone, unmanned aircraft flew over 100,000 flight hours in support of Operation Enduring Freedom and Operation Iraqi Freedom.

UAVs are often utilized in missions that are considered too “dull, dirty or dangerous” for manned aircraft. The central areas, ‘dull’ (Intelligence, Surveillance and Reconnaissance ISR); the ‘dirty’ (atmospheric environment assessment); and the ‘dangerous’ (suppression of enemy air defense) are UAV tasks that can provide services in both military and civilian arenas. UAV classifications typically fall into one of six functional categories; however, recently unmanned systems have been developed for multi-role capabilities. The six functions include<sup>2</sup>:

- Target and Decoy – providing the ground and aerial gunnery a target that simulates an enemy aircraft or missile
- Reconnaissance – providing battlefield intelligence
- Combat – providing attack capability for high-risk missions
- Logistics – specifically designed for cargo and logistic operations

- Research and Development – used to further develop UAV technologies to be integrated into field deployed UAV aircraft
- Civil and Commercial – specifically designed for civil and commercial applications

The civilian applications are continually growing, including, for example firefighting.

UAVs are also commonly categorized based on the vehicles' design and performance specifications, which include miniature, handheld low altitude through large High Altitude Long Endurance (HALE), high speed hypersonic, and even low earth orbital (Mach 25+) vehicles. Similarly, the U.S. Military bases the vehicles' role in an overall usage plan for integrated operations, using a tier system for UAV categorization. Each military branch has separate parameters within the tier systems, but the concepts are similar and are based on the vehicles' size and range capability. The first tier, Tier I are micro to small UAVs such as the RQ-14 Dragon Eye that operate at low altitudes. Tier II are vehicles that fly at mid-range altitudes like the MQ-1 Predator, MQ-9 Reaper, and the ScanEagle. The conventional HALE UAVs are placed in Tier III, and operate at 60,000+ feet altitudes at low to mid airspeeds for extended periods of time. The RQ-4 Global Hawk and the solar powered Pathfinder and Helios are under Tier III operations.

The basic essentials of unmanned vehicles include communication relay between the vehicle and ground operator for maintaining Situational Awareness (SA), vehicle and payload sensors based on the UAVs function, and the use of Global Positioning Systems (GPS) to enable precise navigation. The majority of the UAV functions are in support of remote sensing, the role of providing reconnaissance. Remote sensing equipment includes electromagnetic spectrum sensors, biological sensors, and chemical sensors. Typically, spectrum sensors include visual spectrum, infrared, or near infrared cameras and radar systems. The latter systems equip the UAV with the capability to detect airborne chemical and biological factors. Other UAV functions, for example are in support of roles, but not limited to; scientific research – penetrating areas which may be to dangerous for piloted aircraft; precision strike – providing military air to ground support; and with the recent successful demonstration during the 2008 hurricanes that struck Louisiana and Texas, the increased role for UAVs in search and rescue.

Early UAVs were launched and flown in straight lines or in preset circular flight patterns, capturing video that was recorded on film and was analyzed once the vehicle ran out of fuel and landed. The vehicles, during this time were commonly called ‘drones.’ With the increase in radio frequency technology, the UAV became more sophisticated with the combined capability for remote and built-in control to perform low-level pilot duties such as flight-path stabilization. However, the term ‘drone’ was still often used in describing the more sophisticated aircraft. From this point of view, these vehicles were still not considered autonomous – commonly defined as the ability to make decisions without human intervention. UAV-autonomy technology falls under the following categories<sup>2</sup>:

- Sensor fusion – combining information from different sensors for use on-board the vehicle
- Communications – handling communications and coordination between multiple agents in the presence of incomplete and imperfect information
- Path planning – determining an optimal path for the vehicle to go while meeting certain objectives and mission constraints such as obstacles or fuel requirements
- Trajectory generation (sometimes called Motion planning) – determining an optimal control maneuver to take to follow a given path or to go from one location to another
- Trajectory regulation – the specific control strategies required to constrain a vehicle within some tolerance to a trajectory
- Task allocation and scheduling – determining the optimal distribution of tasks amongst a group of agents, with time and equipment constraints
- Cooperative tactics – formulating an optimal sequence and spatial distribution of activities between agents in order to maximize chance of success in any given mission scenario

A significant amount of effort, largely supported by the military, has been focused in this area, with the recent advances accredited to the field of control science. In fact, autonomy may continue to be the driving field for UAV development and expanding the UAV market.

## 1.1 Objective

The following introduces an adaptive multi-objective technique for UAV path and trajectory autonomy generation, through task allocation and sensor fusion. The dynamic optimization technique generates adaptive flight paths for UAVs based on available flight windows and environmental influenced objectives. Example case-studies and applications are developed and the results are discussed; including the application to the field of Solar Regenerative (SR) HALE UAV flight – demonstrating the potential of the adaptive technique.

## 1.2 Background

Path planning and trajectory generation and regulation categories in UAV flight have been investigated extensively. A number of methods that have been used include evolution-based, extremum-seeking, randomized, neural-network, direct collocation with nonlinear programming, B-spline, quadtree data structuring, probabilistic approaches, Chebyshev pseudospectral, and fast graph search methods. Within the methods, several algorithms have been developed, for example, evolutionary, random tree, Dijkstra, Reduced-State and Hierarchical Dijkstra, and A\* search. Even investigations into the problem formulation of the dynamic and objective equations have been considered, such as an  $n^{\text{th}}$  degree Lagrange polynomial approximation. Off-line and on-line approaches have been considered implementing, including others, the methods and algorithms listed – demonstrating the diversity of approaches in the path planning category of UAV-autonomy (3, 4, 18-59).

To further categorize the path planning methods and trajectory generation efforts, consider the several goals and flight conditions that were investigated. Flight in a horizontal plane 2-D was analyzed (4, 20-21, 32, 48, 59), along with considering the

effects of constant winds (17-19). Employing obstacle avoidance (3, 42-47) and target tracking (48-56) within the trajectory generation was addressed. Path planning for multiple UAV formation and collision free cooperative control and tactical applications have been considered (57-58). Expanding beyond flight vehicles, even steady turns and optimal paths for underwater gliders have been investigated (60).

The underlying commonality of the work mentioned is the single-objective analysis. Typical single-objectives to path planning include time of flight or vehicle performance, such as endurance. Conflicting objectives when determining flight trajectories are generally unaccounted for. However, there are two main existing procedures that convert the multiple conflicting objectives into a single objective problem that have been used<sup>3</sup>. One method ( $\epsilon$ -constraint method), selects one of the objectives for the analysis while the others are used as constraints, restricting the objective within a safe limit. The other, the weighted-sum approach, combines all objectives to form a single-objective. Both procedures require artificial parameters, such as limiting values in the  $\epsilon$ -constraint method or assigning relative weights in the weighted-sum procedure. Consequently, the results are dependent on the accuracy of the chosen parameters, and in the case of UAV flight tasks, choosing the parameters are not straight forward. Concerns for the procedures should be addressed. For conversion of multiple objectives into a single objective, the objective types need to be consistent; either all of minimization or maximization type. With a conversion procedure using a weighted-vector, each objective must be normalized in magnitude prior to determining the weighted average. This requires relying on past experience or guessing when assigning the relative weight (or  $\epsilon$ ) vector.

### 1.3 Current Multi-Objective Procedures

New frameworks have been developed accounting for multiple objectives to UAV flight management. The operational objectives, generally, include: platform safety; minimizing fuel, time, distance; and minimizing deviation from the current path. The

main commonalities of the recent developments have been the multiple solution paths generated based on predefined terrain criteria called meta-paths. The meta-paths, in excess of 15 or more, provide an off-line analysis and the decision, from the available generated paths, the ‘best’ possible route.

For instance; an off-line path planning investigation using multi-objective evolutionary algorithms was considered by Mittal et. al. (3). The procedure introduced a three-step hybrid algorithm. The steps of the algorithm first generated several path solutions, called Pareto-optimal, each with different trade-offs to the objective functions. With the generated solutions, eight to ten were selected providing trade-offs between the objectives; and locally searched to obtain a set of solutions close to the true Pareto-optimal front – of which a single flight path was to be selected. The off-line process required prior terrain topography information and representation in determining the UAV paths.

Similarly, Foo et al. and Swarzenruber et al. (3, 62, 63) used Particle Swarm Optimization to generate multiple solutions based on predefined criteria. A single summarized representation of the 15 total alternate paths, for a particular preference was selected to form the meta-paths in the final decision making process.

The work, here within, introduces an adaptive path generation for UAVs considering multiple independent conflicting objectives without the necessity of developing artificial or weighting parameters. The technique generates a single flight path based on an environmentally influenced objectively driven flight window for the UAV. The process is locally-optimal based and adaptive, reducing, if not eliminating the “curse of dimensionality” – which is often stated when describing the significant size in decision space required for off-line path search techniques. It is not limited by individual methods or algorithms, however, certain procedures in comparison are advantageous.

The goal was to develop a technique that did not require off-line analysis of meta-paths to determine the ‘best’ possible route; but rather a single adapting flight path furthering the UAV-autonomy. Due to the nature of the optimized condition, the path generated is locally constrained based on the influenced objectives; and may not present the ‘best’ global optimum the off-line meta-paths provide.

### 1.3.1 SR-HALE Applications

With the recent flight demonstrations of solar powered vehicles, interest in path planning and trajectory generation is increasing, with very limited current development. Recent work by Klesh et al. (4), addressed the subject by developing a power index (artificial parameter), combining both solar power and required power for flight into a single-objective, in the case of the UAV task. The combined single-objective analysis was done for a vehicle flying from initial to final position and heading over a short period of time while under the assumption that the sun was fixed.

The question was posed, can a UAV continually fly while maximizing the solar power input and minimizing the power required for flight; and maintain continual SA over an Area of Interest (AOI)? With the potential for flight extending weeks or possibly months, an off-line multi-objective meta-path analysis would be difficult in predicting such a long duration flight. The long endurance requires an adaptive process, taking advantage of the ephemeris conditions for the solar regenerative power systems on the UAV – providing a sound and novel case-study for the multi-objective technique introduced.

## CHAPTER 2

### DUAL-OPTIMAL PATH-PLANNING TECHNIQUE

The Dual-Optimal Path-Planning (D-O.P-P.) Technique utilizes dynamic optimization for determining optimal flight trajectories between continually updating optimal intermediate-states for the UAV, based on environmentally-influenced objectives. The environmentally- influenced optimal condition, known as the ‘driver’ determines the next condition, within a downstream virtual window of possible vehicle destinations and orientation built from the UAV kinematics. The step results are pursued by a dynamic optimization technique to determine the flight path – by minimizing a cost function subject to dynamic equation constraints, control inequality constraints, interior state equality/inequality constraints, and boundary conditions with initial and final states determined by the driver-optimized results.

This sequential optimization technique is a multi-objective optimization procedure consisting of two goals, without requiring additional information to combine the conflicting objectives into a single-objective. The individual goals and objective complexity are not limited in type and are determined on an individual basis. The solving technique is also algorithm independent, allowing for versatility in the process of developing the vehicle trajectory.

The technique, in general form, can be expressed mathematically and shown in Table 2.1.



Table 2.1: D-O.P-P. Technique

**Driver:**

Minimize  $f(\mathbf{x})$ ; subject to  $g_i(\mathbf{x})$ ,  $(i = 1, \dots, n)$  ,

with solution:

$$\mathbf{x}_k^*, (k = 1, \dots, N)$$

**Path:**

Minimize  $J(u) = \int_0^T f_0(\mathbf{x}(t), u(t)) dt$  ,

where

$$\mathbf{x}(t), (\mathbf{x}_{k-1}^*(t), \dots, \mathbf{x}_k^*(t)): [0, T] \rightarrow \mathfrak{R}^n$$

is the solution of the differential system with boundary conditions and with initial and final conditions

$$\frac{d\mathbf{x}_j}{dt} = f_j(\mathbf{x}, u(t)), \quad (j = 1, \dots, n);$$

$$\mathbf{x}(0) = \mathbf{x}_{k-1}^*; \quad \mathbf{x}(T) = \mathbf{x}_k^*$$

where

$$J(u^*) = \min_{u \in U} J(u)$$

with  $u^*$  and the associated path  $\mathbf{x}$  called 'optimal.'

Notice the  $\mathbf{x}_k^*$  solution to the driver-objective determines the final time solution of  $\mathbf{x}(t)$  for the path cost function. The path-objective analysis was based from classical optimal control theory and the powerful result known as the 'minimum principle of Pontryagin'.

For further clarification, a visual of the basic D-O.P-P. flight window for the technique can be seen for 2-D planar flight below, Figure 2.1.

### D-O.P-P. FLIGHT MANEUVERING WINDOW

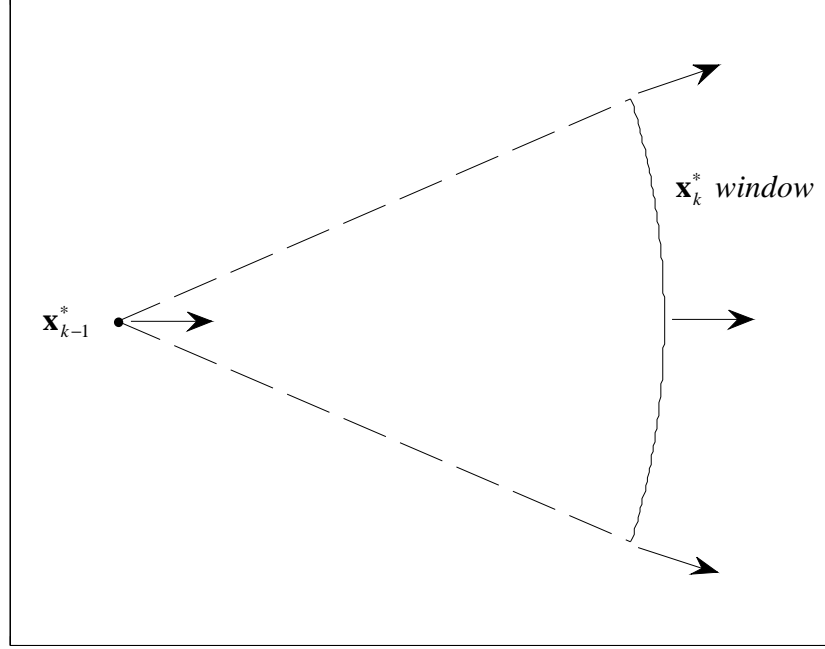


Figure 2.1: D-O.P-P. Flight Maneuvering Window (2-D)

The vehicles initial location  $\mathbf{x}_{k-1}$  ( $\mathbf{x}_{k-1}^*$  for an optimum) for 2-D flight consist of its location, velocity, bank angle, and heading;  $f(\mathbf{x}_{k-1}) = f(x_{k-1}, y_{k-1}, V_{k-1}, \phi_{k-1}, \psi_{k-1})$ . In terms of three dimensional, the vehicle's pitch angle and altitude are also required. At the initial location with the desired driver window projection distance, the available UAV flight window is projected forward of the heading direction and bounded based on the vehicle's kinematics.

For instance, looking at Figure 2.1, at the initial vehicle  $\mathbf{x}_{k-1}^*$  location, if the vehicle were to bank hard right (right wing down) would correspond to the farthest right location (with respect to initial heading) of the driver window. Similarly, a hard left bank would place the vehicle at the farthest left available position. Throughout the window, the vehicle has a  $\mathbf{x}_k$  condition with corresponding location, velocity, bank and heading. The environmentally-influenced driver-objective is optimized along this available flight window determining the  $\mathbf{x}_k^*$  location and vehicle orientation. With that

destination, the vehicle then proceeds from the initial to intermediate-state  $\mathbf{x}_k^*$  location along an optimum flight path. The vehicle's path-objective, for example could be minimizing time, maximizing endurance, or minimizing power required. The process is then continued for all intermediate-states ( $k=1, \dots, N$ ) until the overall destination or time is reached. Figure 2.2 is a visual of the basic flight window for the technique considering three-dimensional space.

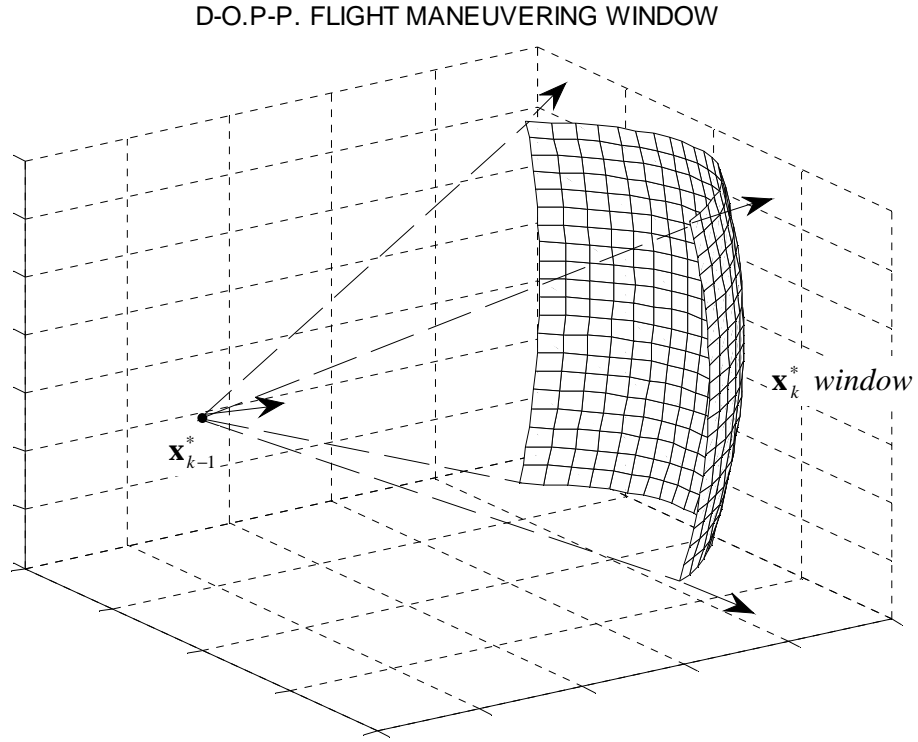


Figure 2.2: D-O.P-P. Flight Maneuvering Window (3-D)

Even though the technique is independent of algorithm, with the desire for a real-time analysis, there are methods that are more suited for on-line processing. In general, the driver-objective, due to generating the available flight window from the UAVs flight mechanics, search algorithms are advantageous. In this technique, regardless, the methods are required to be adaptive with the flight window (for all  $N$ ), a case in point is an adaptive-A\* search algorithm.

## *CASE STUDY:*

### *SOLAR POWERED UAV FLIGHT*

High altitude flight, flight at or above 60,000 feet, benefits from staying above turbulence, weather and air traffic; but comes with a price. As altitude increases the density decreases, requiring a larger lifting surface and a propulsion system that can operate in a low density atmosphere. These issues become more apparent for sustained on station persistent ISR flight. Continual surveillance over an AOI or Area of Responsibility (AOR) implies slow flight to maintain situational awareness. Slow flight in turn implies an increase in wing area and typically a decrease in wing loading, the ratio of the vehicle weight to the wings planform area. This encompasses its own challenges in vehicle design and operation. Regardless, there are current UAV platforms that reach these higher altitudes. The RQ-4 Global Hawk is one such UAV that has been used for reconnaissance, but it has a limited fuel capacity which results in a limited endurance and thus, restricted surveillance capability. Alternate methods for propulsion systems to potentially replace conventional fuel systems and increase endurance capability have been investigated. One method utilizes the photovoltaic solar panel to gather power from the sun.

Harnessing solar energy has recently been adapted for use on high altitude UAV platforms. An aircraft that uses solar panels and powered by the sun during the day and through the night by SR systems, in principle could sustain flight for weeks or months. Only mechanical wear would limit the flight duration. Aerovironment's Pathfinder has demonstrated the potential of solar powered flight with its flight demonstrations in the mid 1990's which has records of flight surpassing 60,000 feet powered by solar energy and a SR system. The high aspect ratio, flying wing vehicle has very low wing loadings, less than one pound per square foot, limiting the flight capability. The risk of damage or

even catastrophic failure when climbing through and flying below turbulent weather has been encountered and will always be a limitation for this vehicle. Due to the promising flight tests of the Pathfinder, this vehicle's configuration and flight mechanics were chosen for a representative Solar Regenerative High Altitude Long Endurance (SR-HALE) UAV for flight path-planning investigations.

A case-study location was selected; however, a discussion for harnessing solar power with varying latitudes is addressed throughout. The case-study location that was chosen was Columbus Ohio, its location and standard meridian is shown below.

Table 2.2: Case-Study Location

<b>Columbus: Ohio: United States</b>			
Longitude:	82 <sup>0</sup> 59' 56"	West	(-82.99889 W)
Latitude:	39 <sup>0</sup> 57' 40"	North	(39.96111 N)
<b>Standard Meridian: U.S. Eastern (EST)</b>			
Longitude:	75 <sup>0</sup> 00' 00"	West	(-75.00000 W)

The case-study change in ephemeris throughout the year provides a geographically neutral location to demonstrate the potential of the D-O.P-P. Technique. This demonstration is limited to a constant altitude of 60,000 feet; and a flight window is set based on existing surveillance package capabilities, restricting vehicle flight paths to provide and maintain continual SA over the AOI. The requirements and limitations of SR-HALE UAVs along with vehicle orientation in planar flight are addressed and used to gather a necessary general understanding of solar-regenerative flight. SR-HALE fixed flight patterns, within the flight windows will be analyzed to demonstrate the required and available power during flight overall performance capabilities and limitations – providing a comparable baseline.

The objectives of the D-O.P-P. Technique are to determine the minimum required power flight paths to the predetermined location and orientation for obtaining maximum solar flux established by the 'driver.' This was done for still wind and constant wind conditions at altitude over the AOI and the variations in latitude.

## CHAPTER 3

### SR-HALE REQUIREMENTS AND LIMITATIONS

#### 3.1 Ephemeris

The available solar energy for a SR-HALE UAV is determined by two main factors: the location (longitude and latitude) and the time (season) of flight. From an observer on Earth the sun's apparent motion is established by the earth's rotation about its axis and its revolution around the sun. This time interval is known as the solar day. The mean solar day is exactly 24 hours and varies slightly due to the earth's tilt on its axis. The earth's effective revolution frequency is smaller at the equinoxes of the sun where it crosses the equator at an angle of  $23.5^{\circ}$ . The seasonal deviation of the apparent solar day about the mean solar day is at its maximum of 24 hours and 30 seconds at the winter solstice and its minimum of 23 hours and 41 seconds shortly before the autumnal equinox<sup>4</sup>. There is a difference between of less than one minute, 0.07% of the mean solar day. However, this effect is cumulative and must be accounted for over a long period.

##### 3.1.1 Equation of Time

The equation of time (EOT) accounts for the cumulative effect of the variation in the solar day. The EOT curve is plotted in Figure 3.1.

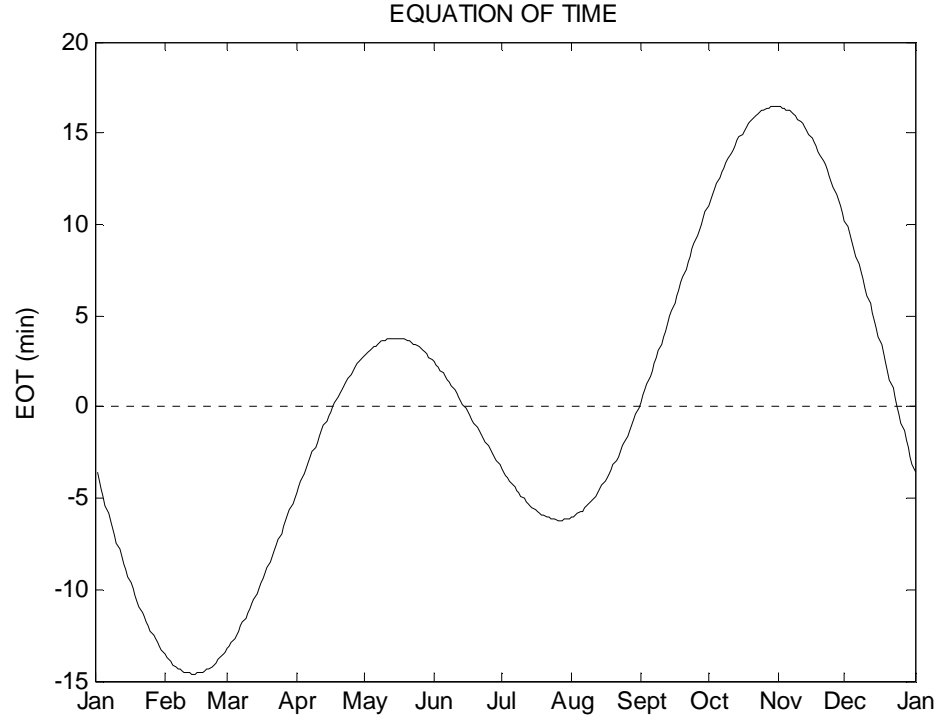


Figure 3.1: Equation of Time

The EOT time is centered with its average value at zero. Any variation in EOT is primarily due to leap years and is less than 20 seconds (1.06%). This variation is less than 0.006% of the mean solar day and was disregarded.

The meridian transit occurs when the sun crosses an imaginary line connecting the north and south poles and passes directly over an observer head, known as solar noon. Greenwich (England: Longitude  $0^0 0' 0''$ , Latitude  $51^0 28' 38''$  N.) time is set so that solar noon occurs at 12:00 noon for the EOT mean value (zero), approximately on 16-April, 14-June, 1-September, and 25-December. The local standard time at which solar noon will occur for any observer can now be conveniently determined by the following relation<sup>4</sup>.

$$\begin{aligned} \text{Solar noon (in local standard time)} \\ = 12 : 00 - 4(Long_{st} - Long_{loc}) - EOT \end{aligned} \quad (3-1)$$

$Long_{st}$  is the standard meridian for the observer's time zone and the result is in minutes. The solar time is defined as the local time shifted so that solar noon occurs at 12:00 noon.

$$Solar\ time = standard\ time + 4(Long_{st} - Long_{loc}) + EOT \quad (3-2)$$

The variation in EOT is transferred into solar noon and when necessary, as with the chosen case-study, daylight savings time must be accounted for.

Solar noon and the required shift to local time for Columbus, OH are shown in Table 3.1.

Table 3.1: Case-Study Solar Noon

<b>Columbus: Ohio: United States</b>		
Longitude:	82° 59' 56" West	(-82.99889 W)
Latitude:	39° 57' 40" North	(39.96111 N)
<b>Solar Noon</b>		
Vernal Equinox:*	12:39	app 21 Mar
Summer Solstice:*	12:30	app 21 Jun
Autumnal Equinox:*	12:25	app 21 Sept
Winter Solstice:	12:33	app 21 Dec

\* Add 1 hour for daylight savings

Solar time lags local time by 33 minutes during winter solstice and with daylight savings, by one hour and 30 minutes during the summer solstice.

### 3.1.2 Solar Coordinates

For the SR-HALE analysis and program development the technique used for tracing the sun through the sky at any given location and duration of time was the described by Weider<sup>4</sup>, and will be briefly addressed. The technique determines the local solar coordinates, the zenith angle (Z) and the azimuth angle (A) for an observer through the geocentric coordinates, the codeclination (D') and the hour angle (H). The geocentric coordinate system has an origin at the center of the earth with the z-axis as an axis



connecting the north-south poles. The other two axes lie on the equatorial plane, with the x-axis oriented toward the local (chosen) meridian. Using this coordinate system, the codeclination angle is the angle between the North Pole and the sun's rays and the hour angle is the angle between the local meridian x-axis the projection of the sun's rays onto the equatorial plane. These two angles can be determined by the following,

$$\cos D' = \sin(23.5^\circ) \sin\left(\frac{360^\circ * n}{365.25 \text{ days}}\right) \quad (3-3)$$

and

$$H = \pm \frac{360^\circ}{24 \text{ hrs}} t \quad (3-4)$$

where n is the number of days after the vernal equinox and t is the number of hours before and after solar noon.

The local coordinate system is situated at the local latitude (L) on the earth's surface with the z-axis normal (vertical) and the x-axis oriented due south. The zenith angle is then the angle between the z-axis and the sun's rays and the azimuth angle is the angle between the x-axis and the projection of the sun's rays on the horizontal x-y plane. The local coordinate Z and A can be related to the geocentric codeclination and hour angle by

$$\cos Z = \cos D' \cos L' + \sin D' \sin L' \cos H \quad (3-5)$$

and

$$\tan A = \sin D' \left( \frac{\sin H}{(\sin D' \cos L' \cos H - \cos D' \sin L')} \right) \quad (3-6)$$

where L' is the colatitude of the observer.

### 3.1.3 Daylight Hours

The zenith angle for solar noon, when the sun is the highest in the sky for any observer, is simply the magnitude of the difference between the solar declination and the observer's colatitude. Sunrise and sunset is dependent upon terrain and at which point is taken as sunset on the solar disc. For the condition of an observer on the earth's surface, sunrise and sunset will be taken when the zenith angle is 90 degrees where the sun's rays are parallel to the earth's surface at the desired location. Setting  $Z = 90$  degrees in equation (2-5), the hour angle for sunrise and sunset can be expressed

$$H_s = \pm \cos^{-1}(-\cot D' \cot L') \quad (3-7)$$

and the number of daylight hours as

$$T_{Daylight} = 2 * t_s = \frac{24 \text{ hr}}{180^\circ} H_s \quad (3-8)$$

The available daylight hours with variation in latitude from the equator to 60 degrees for both the northern and southern hemispheres are shown in Figure 3.2.

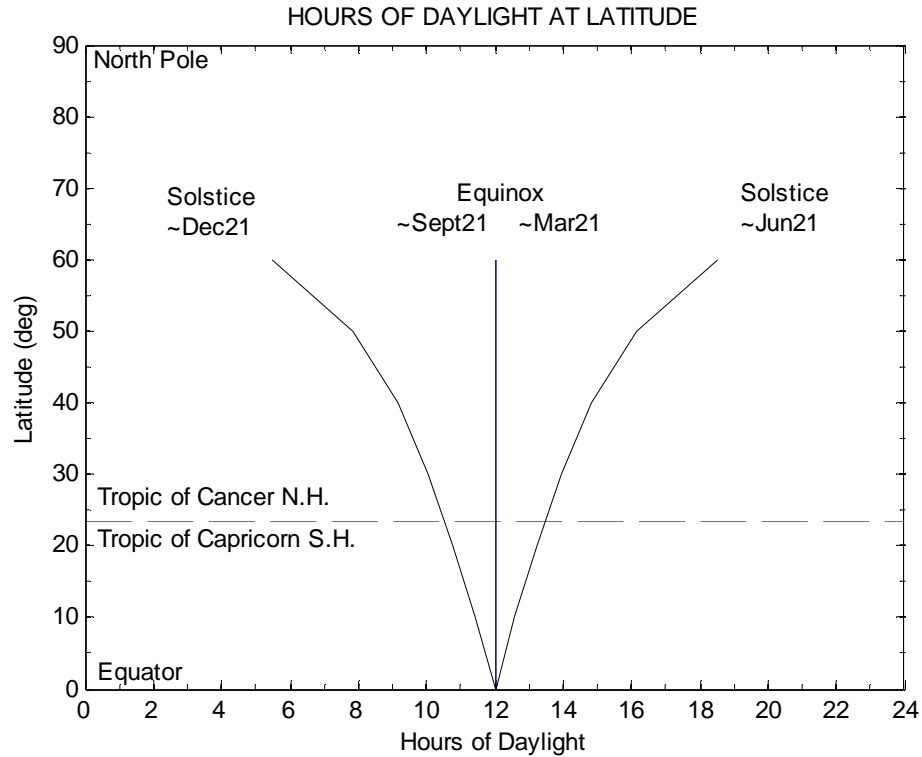


Figure 3.2: Hours of Daylight at Latitude

The figure shows the minimum available daylight at the ~21-December solstice corresponding to winter in the northern hemisphere and summer in the southern, as well as the maximum available sunlight during the ~21-June solstice.

For the Columbus Ohio case-study, at a latitude of  $39^{\circ} 57' 40''$  North has a minimum amount of daylight at the winter solstice of 9.15 hours (09:09:00) and a maximum of 14.85 hours (14:51:00) during the summer solstice.

At an altitude of 60,000 feet (11.40 miles) and taking the earth's radius in consideration the increase in "line-of-sight" for sunrise and sunset of a vehicle at that altitude is approximately  $90^{\circ} + 0.26^{\circ}$  in the longitude. This correlates to an increase of 18 miles of visibility over the earth's surface. This difference translates to an increase in

0.5<sup>0</sup> in azimuth for both sunrise and sunset and ultimately results in an approximately 2.4 minutes increase in daylight.

Table 3.2 lists the available daylight, zenith angle at solar noon and the azimuth angles for sunrise and sunset for both an observer at and a SR-HALE vehicle flying 60,000 feet over Columbus Ohio during the seasons.

Table 3.2: Case-Study Available Daylight

<b>Observer on Earth's Surface: Columbus Ohio</b>			
Season	Ava. Daylight (Hrs:Min:Sec)	Z <sub>noon</sub> (degrees)	A <sub>rise/set</sub> (degrees)
Vernal Equinox:	12:00:00	50.04	± 90.00
Summer Solstice:	14:51:00	97.04	± 121.35
Autumnal Equinox:	12:00:00	50.04	± 90.00
Winter Solstice:	9:09:00	16.46	± 58.65
<b>SR-HALE Vehicle at 60,000 ft Altitude: Columbus Ohio</b>			
Season	Ava. Daylight (Hrs:Min:Sec)	Z <sub>noon</sub> (degrees)	A <sub>rise/set</sub> (degrees)
Vernal Equinox:	12:02:24	50.04	± 90.00
Summer Solstice:	14:53:24	97.04	± 121.85
Autumnal Equinox:	12:02:24	50.04	± 90.00
Winter Solstice:	9:11:24	16.46	± 58.15

#### 3.1.4 Surface Obliquity

The orientation of a surface with respect to the sun's position is important especially in determining the amount of available solar power. This is determined by the obliquity factor ( $\cos \theta$ ) and is determined by the local solar coordinates (Z and A) and the tilt coordinates of the surface ( $\Delta$  and  $\psi$ ). The first tilt coordinate,  $\Delta$ , is the angle between surface normal and the vertical. The second,  $\psi$ , is the angle between the projection of the surface normal in the horizontal plane and due south direction. The tilt coordinates fix the direction of the surface normal. This is similar to the way solar coordinates fix the direction of the sun's rays relative to a location. The obliquity factor is given by:

$$\cos \theta = \cos Z \cos \Delta + \sin Z \sin \Delta \cos(A - \psi) \quad (3-9)$$

This equation shows that under certain circumstances, a surface with only solar panels on the upper surface will not be able to collect solar power when the obliquity factor becomes negative ( $\theta > 90^\circ$ ).

### 3.2 Solar Flux

With in earth's atmosphere the solar intensity felt on a surface is composed of the direct and diffuse components. The latter term is the radiation that is scattered due to the atmosphere and the reflected radiation due to an underlying terrain. The study of total solar intensity, direct and diffuse is one of the most advanced and complicated procedures which requires solving the equation of radiative transfer, an integrodifferential equation. For SR-HALE vehicle applications, three assumptions will be made in order to develop a semiquantitative analysis of solar flux. (1) The diffuse flux, due to the scattering of the solar intensity through the atmosphere has a significantly smaller effect than the direct flux component. This assumption is often used for approximating solar intensity at the earth's surface. The validity of this assumption increases at high altitudes with the solar radiation traveling through less of the atmosphere. (2) The downward diffuse flux on the surface due to scattering radiation is isotropic. (3) The upward diffuse flux on the surface will be considered negligible and disregarded in the formulation of the analysis. The upward diffuse flux is on the order of the reflective radiation component due to the underlying earth's surface. With increase in the altitude the earth's reflectivity radiation decreases; and for high altitude applications the effects of the upward diffuse flux will be comparatively less to its counter downward diffuse flux component. With these assumptions the following equation will be used in determine the total solar flux ( $F$ ):

$$\begin{aligned}
F &= F^{(direct)} + F^{(diffuse)} \\
&= F^{(direct)} + \left[ \frac{1 + \cos \Delta}{2} \right] F^{\downarrow (diffuse)}
\end{aligned} \tag{3-10}$$

where,

$$F^{(direct)} = S_0 \mu e^{-\tau/\mu_0} \tag{3-11}$$

and,

$$F^{\downarrow (diffuse)} = S_0 \mu_0 \left[ \frac{1}{1+G} \left( G e^{\gamma^+ \tau} + e^{\gamma^- \tau} \right) - e^{-\tau/\mu_0} \right] \tag{3-12}$$

$S_0$  is the solar constant (125.6 W/ft<sup>2</sup> or 1352 W/m<sup>2</sup>). The surface orientation parameters are the tilt angle ( $\cos \Delta$ ), obliquity of the panel to the sun's rays ( $\mu = \cos \theta$ ), and the cosine of the solar zenith angle ( $\mu_0 = \cos Z$ ). The equations include two environmental parameters, the optical thickness ( $\tau$ ) and the single scattering albedo ( $\tilde{\omega}_0$ ) with in the variables  $G$  and  $\gamma^\pm$ ;

$$G = - \left[ \frac{\gamma^- + A}{\gamma^+ + A} \right] e^{(\gamma^- - \gamma^+) \tau} \tag{3-13}$$

$$\gamma^\pm = \frac{1}{2}(C - A) \pm \frac{1}{2} \left[ (C - A)^2 - 4BD \right]^{1/2} \tag{3-14}$$

where,

$$\begin{aligned}
A &= \frac{2 - \tilde{\omega}_0}{2\mu_0} & B &= \tilde{\omega}_0 \\
C &= 2 - \tilde{\omega}_0 & D &= \frac{\tilde{\omega}_0}{2\mu_0}
\end{aligned} \tag{3-15}$$

The environmental parameters are functions of the sun's ray wavelengths. For the parameters, Rayleigh's law is commonly used in which the theory suggests that the scattering of solar energy varies smoothly with wavelength. This law is based on the altitude conditions, mean molecular mass of air, the index of refraction of the atmosphere

and the constant Avogadro's number. For a relatively clear atmosphere the averaged optical thickness and the scattering is less than 0.3 and 0.6 respectively. Considering a completely horizontal surface ( $\Delta = \mu = Z = 0^\circ$ ); the solar intensity increases with altitude from  $F = 93 \text{ W/ft}^2$  ( $1000 \text{ W/m}^2$  or 1 sun) at the earth's surface to slightly over  $121 \text{ W/ft}^2$  ( $1300 \text{ W/m}^2$  or 1.3 sun) at 82,000 ft (25 km) altitude. Also note that in terms of orientation the component of the solar intensity due to the downward diffuse flux is only a function of the cosine of the solar zenith and independent of the tilt and obliquity of the surface.

For an SR-HALE altitude of 60,000 feet and a surface oriented horizontally, the maximum solar flux is  $116.1 \text{ W/ft}^2$  ( $1250 \text{ W/m}^2$  or 1.25 suns). Of which, the direct solar flux is  $111.5 \text{ W/ft}^2$  ( $1200 \text{ W/m}^2$  or 1.2 sun) and the downward diffuse flux is  $4.6 \text{ W/ft}^2$  ( $50 \text{ W/m}^2$  or 0.05 sun), 4% of the total. The total, direct and diffuse solar flux as a function of orientation for the case-study altitude of 60,000 feet is shown in Figure 3.3.

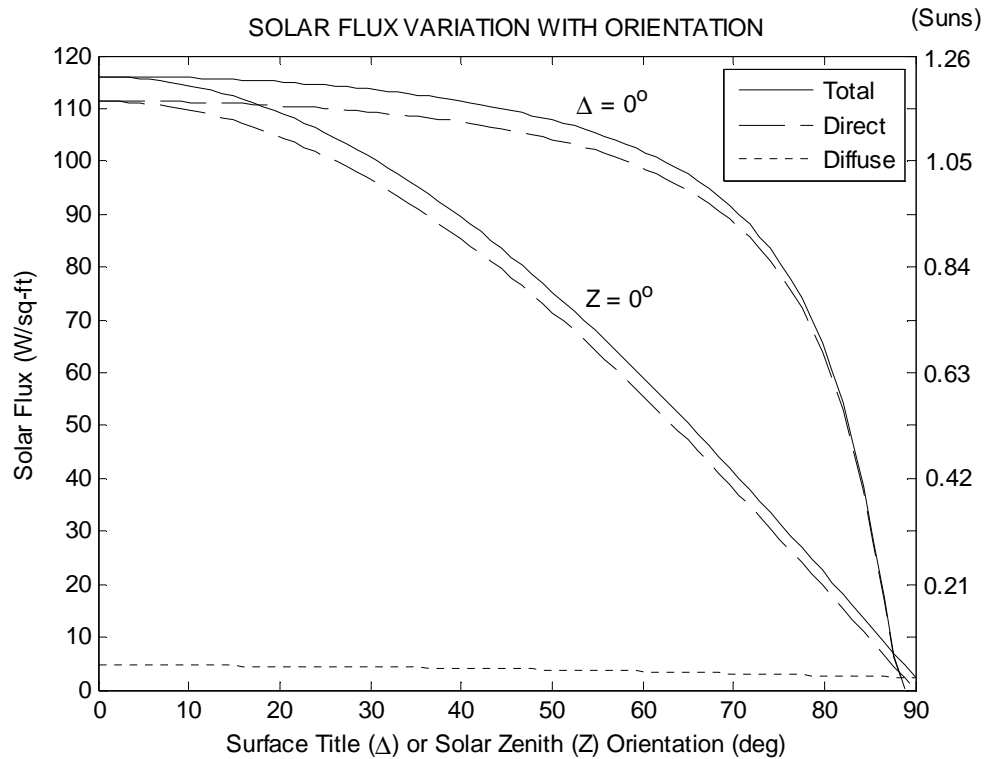


Figure 3.3: Solar Flux with Surface Orientation at 60,000'

The two conditions in Figure 3.3 are variation in surface title angle ( $\Delta$ ) with sun in a constant location, zero solar zenith angle ( $Z = 0^0$ ); and the variation in solar zenith angle from sunrise/set to solar noon with the surface normal to the sun for all zenith angles, zero surface title angle ( $\Delta = 0^0$ ).

### 3.3 Solar Energy – Photovoltaics

Harvesting solar energy with the use of photovoltaics (pv), specifically supplying current ( $J$ ) to an external load is a combination of the photocurrent ( $J_p$ ) through radiative energy or flux and the current shunted by the diodes of the photovoltaic material, the junction current ( $J_j$ );

$$J = J_p - J_j \quad (3-16)$$

To better understand the processes, a semiquantitative empirical analysis approach<sup>4</sup> will be taken for both the junction (material) and photocurrent (radiative). The focus will be on the quantitative effects and direct correlation to SR-HALE applications and the current program development.

The photovoltaic is fabricated by a p-type silicon wafer, the base, on which n-type silicon has been deposited, the surface layer. Photocurrent is generated by the effect of the photons creating hole-electron pairs in the presence of solar energy.

To better understand the p-n junction, consider an external DC voltage applied across the junction. If the positive terminal is located on the n-type material and the negative on the p-type, a current will flow from the n-type to the p-type material. In this condition, a steady-state current cannot be achieved and the maximum current occurring is called the reverse saturation of dark current. This junction is known as reverse biased and the reverse saturation current density is given by:



$$J_0 = DT^3 e^{-\epsilon_g/kT} \quad (3-17)$$

where  $D$  is a characteristic constant of the junction ( $D \propto 0.25 \text{ amp/cm}^3 \text{ K}^3$  for silicon),  $k$  the Boltzmann's constant ( $k = 1/11600 \text{ eV/K}$ ) and  $\epsilon_g$  the energy gap between the bottom conduction band and top valence band ( $\epsilon_g \propto 1.0 \text{ eV}$  for silicon).

If a forward bias is created by placing the positive pole on the p-type material, the majority of the carriers will flow toward the junction and the carriers, the junction current can be represented as;

$$J_j = J_0 (e^{V/kT} - 1) \quad (3-18)$$

where  $V$  is the applied voltage. The forward junction current is a function of both the applied DC voltage and the temperature of the material. Equation (2-18) is known as the diode equation and describes both the forward and reverse conduction. The diode is common in many electronics to resolve an alternating current.

The total photocurrent is related to the total solar flux incident on the surface layer by integrating over the entire wavelength spectrum;

$$J_p = \int J_{p,\lambda} = \bar{K}F \quad (3-19)$$

The average responsivity parameter  $\bar{K}$  is measured in amp/watts and depends on the spectral distribution of the radiation ( $\bar{K} \cong 0.25 \text{ mA/mW}$  for silicon).

Now, the load current (or the voltage) can be represented as function of material properties and the total solar flux;

$$J = \bar{K}F - J_0 [e^{V/kT} - 1] \quad (3-20)$$

or

$$V = kT \ln \left[ \frac{\bar{K}F - J}{J_0} + 1 \right] \quad (3-21)$$

When the external load is removed the short-circuit current operation and the open-circuit voltage operation are represented by;

$$J_{sc} = \bar{K}F \quad V_{oc} = kT \ln \left[ \frac{\bar{K}F}{J_0} + 1 \right] \quad (3-22)$$

The power output density, power per unit cell area is the product of the current and voltage and vanishes under either short-circuit or open-circuit operations. The available power and photovoltaic efficiency can be determined by

$$P_A = VJ \quad \eta = \frac{P_A}{F} = \frac{VJ}{F} \quad (3-23)$$

and regardless of the solar flux level, the maximum efficiency for silicon photovoltaic materials is on the order of 12 to 13 percent<sup>4</sup>.

For the case-study SR-HALE vehicle, the overall maximum power was matched to that of the Pathfinder<sup>5</sup>. Consider solar panels covering 75% of the upper wing surface that can generate 8000 Watts at solar noon. At 60,000 feet at solar noon the maximum solar flux is 1.2 suns. In order to match these parameters consider a cell array consisting of 16 cells in parallel and 75 cells in series each having a 0.5 square-feet of cell area, a total of 600 square-feet. Setting the photovoltaic parameters to  $D \cong 0.25 \text{ mA/cm}^2 - \text{sun}$ ,  $\varepsilon_g = 0.60 \text{ eV}$  and  $\bar{K} \cong 0.25 \text{ mA/mW} - \text{cell}$  the maximum power of 8000 Watts is matched with a solar flux of 1.2 suns. With these parameters, Figure 3.4 is the cell array solar energy characteristics at 60,000 feet.

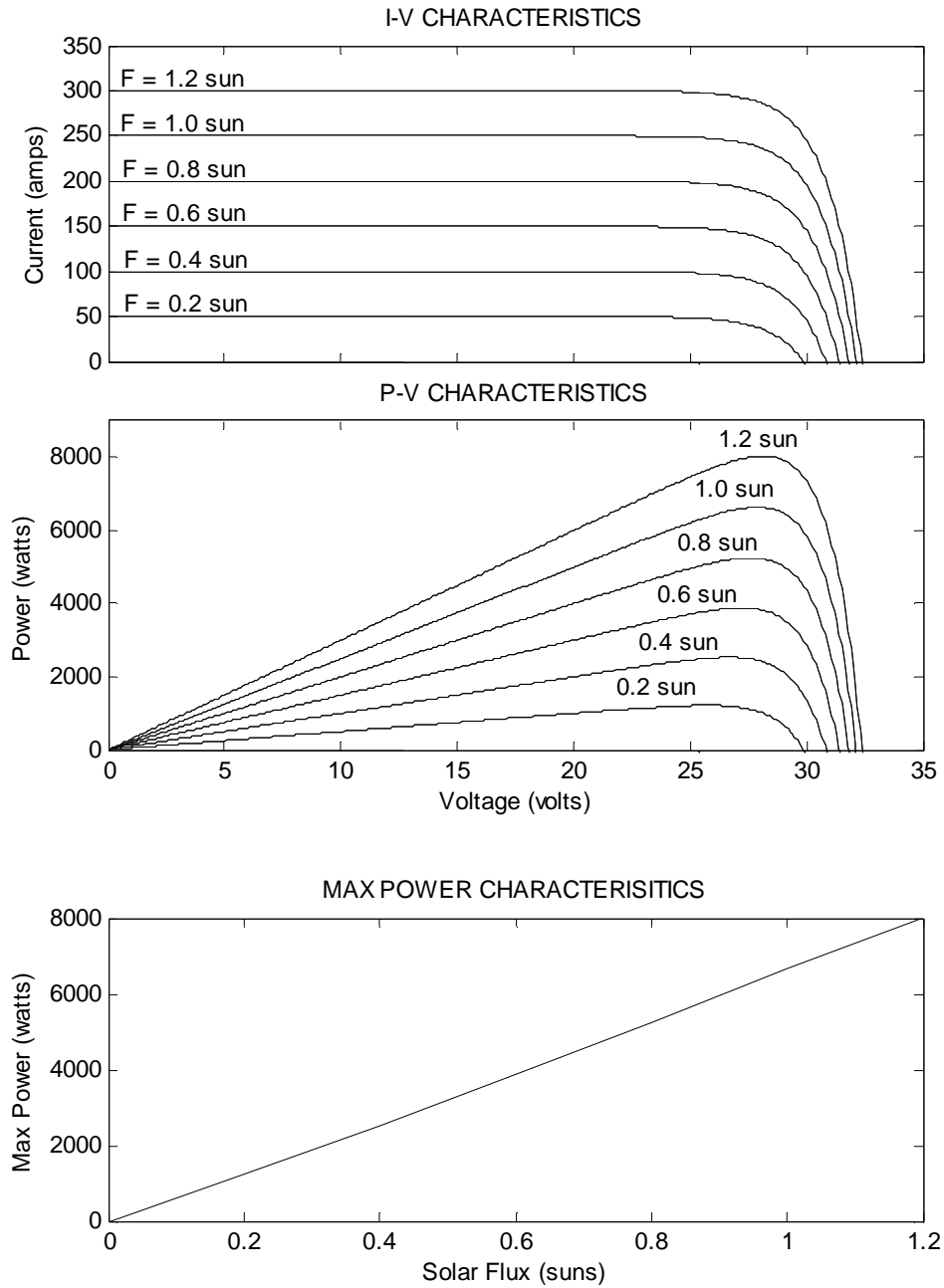


Figure 3.4: Solar Cell Array Characteristic Curves at 60,000'

The maximum available power for any orientation and solar flux level can be determined by combining the maximum power curve from Figure 3.4 with the available solar flux with surface orientation, Figure 3.3.

### 3.4 Systems

The SR-HALE systems are discussed in order to set constraints for the fixed and optimized flight pattern analysis. The general parameters of each system and the performance expected will be addressed. The systems were chosen based on existing equipment that have been proven and used in both solar-regenerative and surveillance platforms.

#### 3.4.1 Electric Motors

The electric motors that were recently outfitted on the Pathfinder and there capability demonstrated in high altitude flight tests were selected for the pattern analyses<sup>5</sup>. The lightweight brushless DC motors are gearless and capable of producing 1.5 horsepower (1.25 kWatts) each. Rare-earth permanent magnets are used to rotate the propellers. This system only requires three moving parts, eliminating over 100 moving parts of its predecessors, providing extreme simplicity. The required number of electric motors is considered a variable based on the aircraft considerations for SR-HALE platforms. This also applies to the high altitude propellers, the expected propeller efficiency and overall aircraft thrust performance.

For the case-study six electric motors equipped with fixed pitched two-bladed propellers will be used capable of producing a maximum of nine horsepower (7.5 kW), a power loading of 13.6 W/lbs and a 0.10 thrust to weight ratio.

#### 3.4.2 Energy Storage

Energy storage systems are key in sustaining 24/7 surveillance capability, in particular with the decreasing daylight hours during the winter months for the northern hemisphere. For SR-HALE vehicles, the energy per mass capacity W-hr/kg that can be stored during the daylight is critical. Lithium-sulfur batteries, from Sion Power have

reported energy/mass values of 350 W-hr/kg; while Lynntech's Gen5 fuel cell technology<sup>6</sup> has shown experimental performance of 640 W-hr/kg. Operating fuel cells at low temperatures have shown the requirement of thermally containing the system for increase in performance; with difficulties during the startup process at very low temperatures.

For the case-study SR-HALE platform the energy storage system will be selected based on mass and used throughout fixed and optimal flight maneuvering. Figure 3.5 shows the required storage system weight in order to maintain a 3,000 Watt power draw with varying energy per mass capacity and no charging.

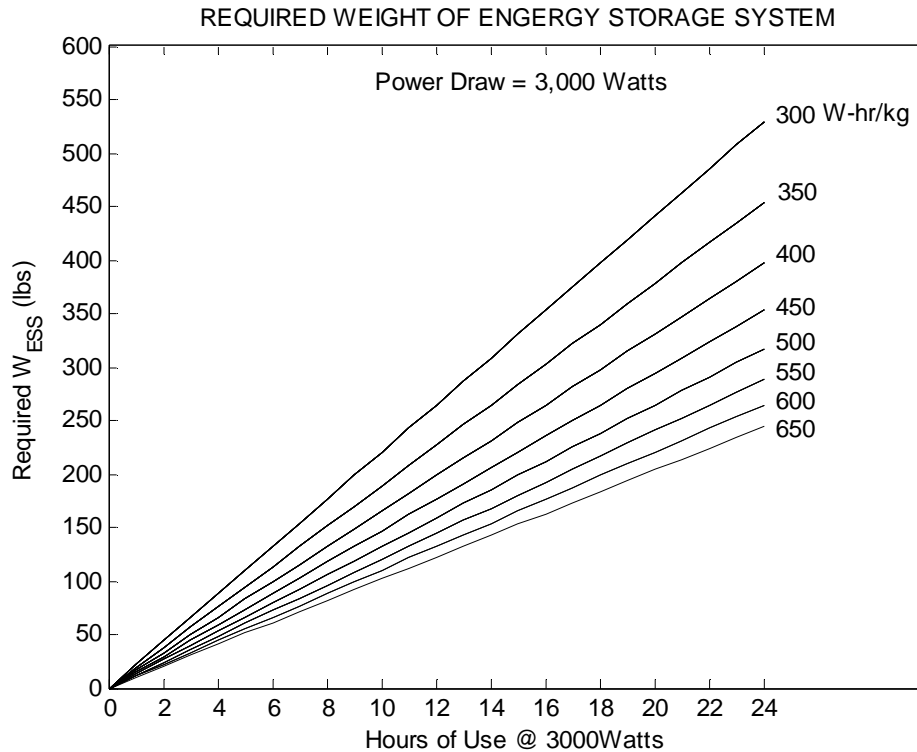


Figure 3.5: Energy Storage System Mass Requirements @ 3000 W Draw

A 3,000 Watt power draw used in Figure 2.5 was specific to the case-study vehicle and is slightly higher than the vehicles minimum power required, discussed in fixed flight

pattern analysis. For the SR-HALE platform, an assumed weight allowed for the energy storage system was 125 lbs. Using fuel cell technology at a 640 W-hr/kg energy per mass capacity allows for a total of 12.1 hours of use at a continuous 3,000 Watt draw with no charge, assuming linear characteristics in power draw with decrease in energy storage. For the SR-HALE UAV, it will be assumed that the energy storage system will not require startup at altitude and will be thermally contained for increase in performance.

### 3.4.3 Surveillance

The specifications of the surveillance equipment were used in determining the flight window constraints for the SR-HALE vehicle operation. For instance, recall for a vehicle flying at an altitude of 60,000 feet would have a line-of-sight that correlates to a 90.26 degrees (sunrise/set) in longitude, or a distance of up to 6,220 mile radius (at the equator). However, to process any detail on the earth's surface from that altitude the surveillance equipment determines the "range-of-sight" for the vehicle.

For the case-study analysis and overall program capability demonstration, the Hughes Integrated Surveillance & Reconnaissance (HISAR) sensor system was used<sup>6</sup>. This system has been carried on the Global Hawk, a UAV performing ISR missions with an on-station endurance of 24-30 hours. HISAR integrates three separate systems controlled through one processor for expanding surveillance capabilities. The operational modes are; (1) wide-area that can detect movement within a radius of 62 miles, (2) strip-mode that provides 20 foot resolution over a 23 mile wide region, and (3) spot-mode that can provide six feet of resolution over a 3.8 mile region with sea-surveillance capability. The payload weight for the SR-HALE vehicle, including the sensor system was set at 25 lbs.

The SR-HALE flight pattern analysis approach taken was to demonstrate performance for the vehicle first in range-of-sight for wide-area mode – and once a target has been acquired, and more detailed surveillance required, then a pattern-transfer would be taken to a new smaller range-of-sight window constraint for the strip-mode – and finally into the spot-mode. Figure 3.6 demonstrates the wide-area mode range-of-sight for the case-study with the vehicle located directly above the Area of Interest.

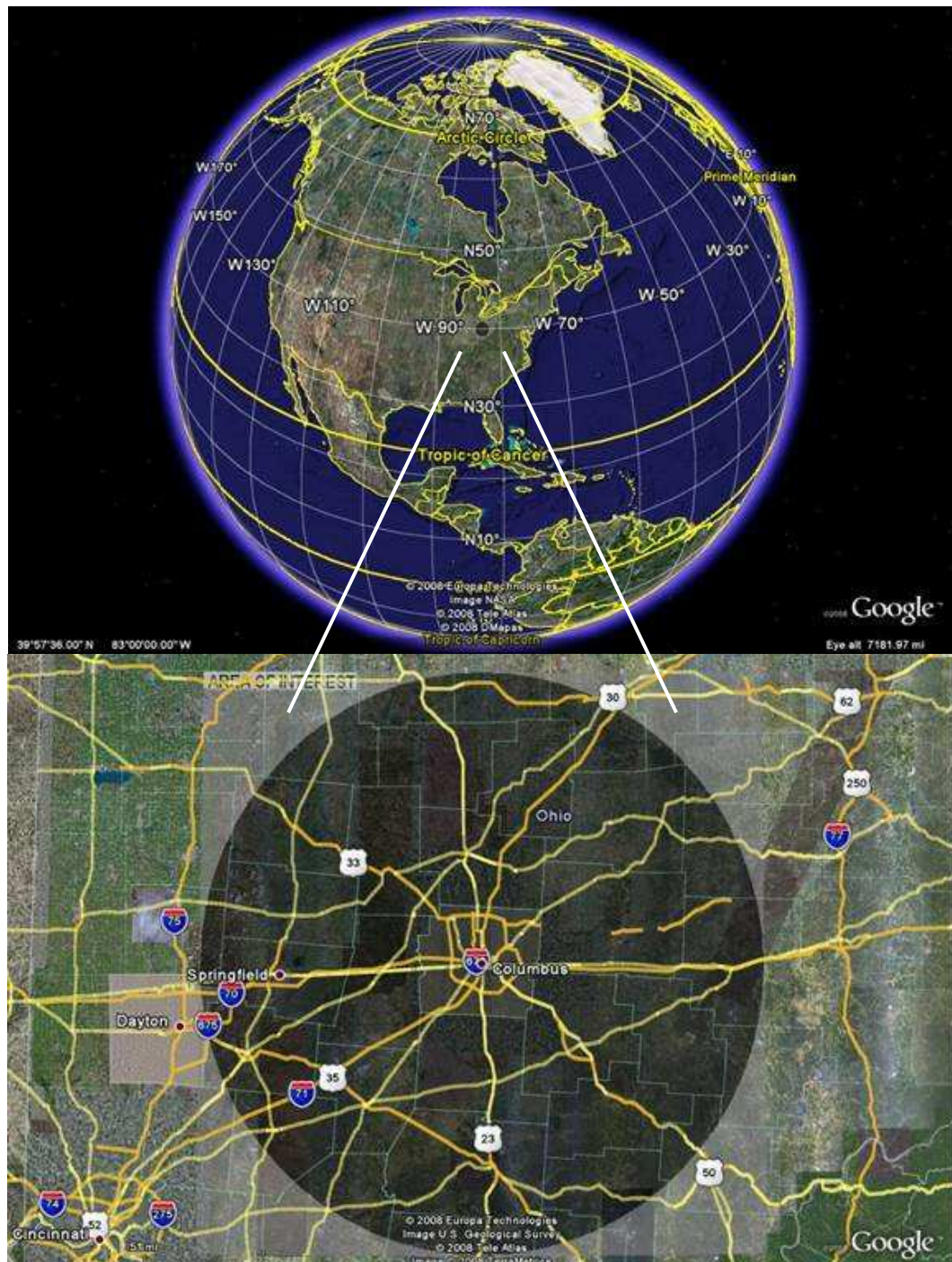


Figure 3.6: Case-Study Range-of-Sight for Area of Interest (Google Earth)

This strategy was selected only for demonstration. The flight operator has control to transfer into and out of any surveillance operational modes when desired as well as to equip the program with other surveillance equipment specifications and the corresponding constraints for range-of-sight.

### 3.5 High Altitude Winds

A study of the upper winds (ranging from 100 to 25 millibars (mb) pressure altitudes) for high altitude platform design was conducted in excess of a 20 year span over four areas of interest<sup>7</sup>. These areas include the contiguous United States, the Norwegian area, the Mediterranean area and the Pacifica area from Alaska to Japan and the surrounding regions. Results of the investigations shown that high altitude wind speeds were at a minimum for altitude ranges of 59,000 to 72,000 feet (18-22 km). Table 3.3 lists the average high altitude wind speed in the aforementioned altitudes for each of the four locations and seasons.

Table 3.3: Average High Altitude Wind Speeds (knots)<sup>8</sup>

Season	United States	Pacific Area	Norwegian Sea	Mediterranean Sea
Winter:	30	50	45	30
Spring:	15	20	30	15
Summer:	25	15	15	20
Fall:	15	30	30	20

Wind roses are provided as an appendix of the referenced report for every 10 mb pressure altitude throughout the areas of interest.

For the case-study AOI the closest locations of high altitude measurements taken and provided wind rose information was Dayton Ohio, 60.1 air miles due west. Measurements at an altitude of 60,000 feet (70 mb pressure altitude) at Dayton Ohio were



used for the case-study analysis and were recreated in Figure 3.7. The area of interest location with respect to the wind rose is shown.

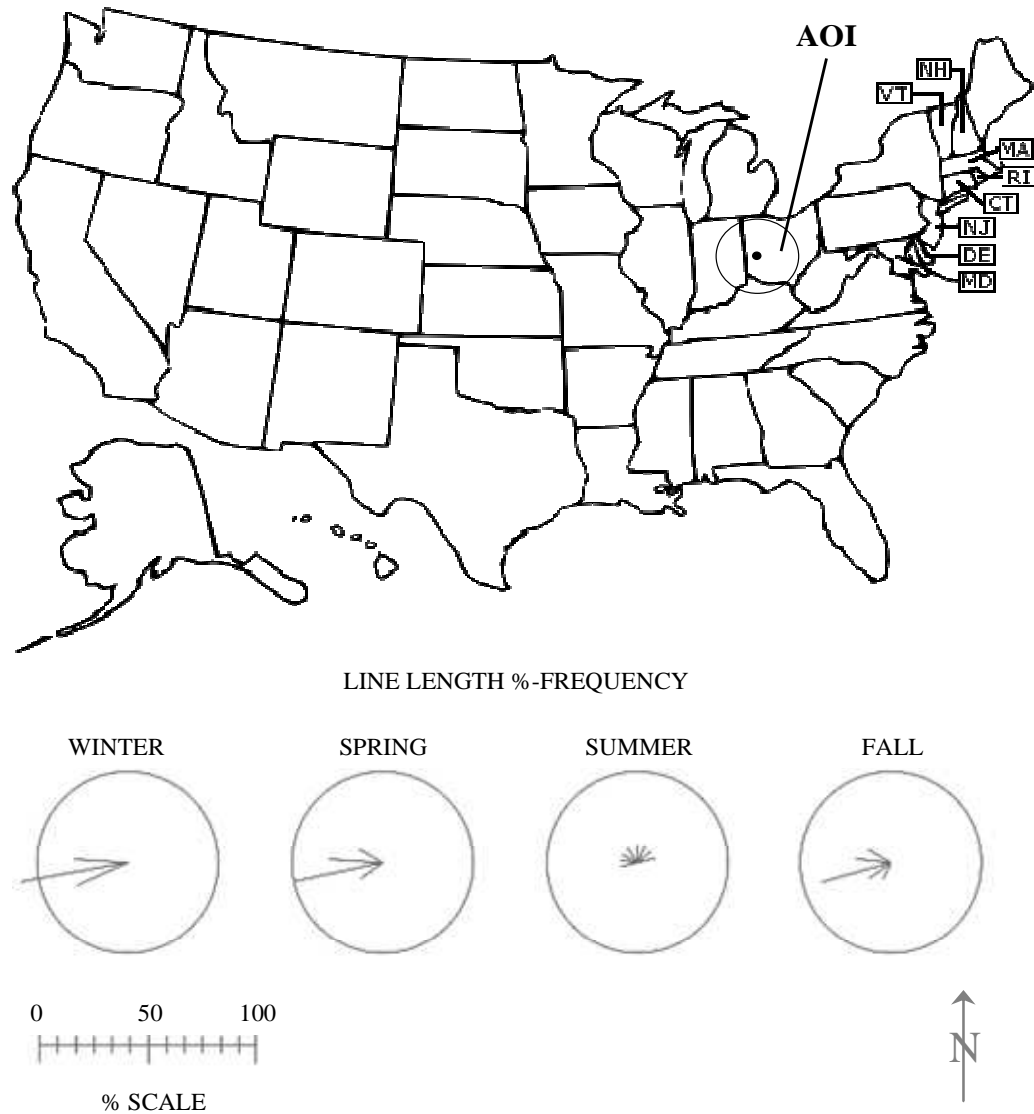


Figure 3.7: Case-Study AOI Wind Roses

The lengths of the line in the wind roses are the frequency percentage of wind direction. The conventional 16 cardinal directions are used. For example, except for the summer season the highest percentage of wind direction for the AOI comes from the West-South-West (W-S-W) direction.

From the upper wind study in that area the minimum wind speed measured was five knots occurring in the summer season and a maximum of 70 knots measured in the winter months. Table 3.4 summarizes the measured wind speeds for the AOI.

Table 3.4: Case-Study AOI Wind Speeds (knots)<sup>8</sup>

Season	Minimum	Maximum	84% level
Winter:	40	70	50
Spring:	20	50	35
Summer:	10	25	20
Fall:	20	50	35

The wind measurements for Washington D.C., 341 air miles due east of the AOI were compared to that of Dayton Ohio to determine if the high altitude winds were steady in both speed and direction through the Midwest region. Wind roses were consistent for all seasons with a slight decrease in wind speeds, supporting the expected high altitude winds for the SR-HALE UAV analysis over the case-study AOI.

### 3.6 SR-HALE Platform

An SR-HALE platform, representing the Pathfinder was selected as the case-study vehicle. With the computations, experimental wind tunnel and flight test data that has been published<sup>4</sup>, this solar powered vehicle demonstrated the capability for sustained flight. Pareto designs have been conducted to optimize the vehicle's planform making this vehicle a suitable study for continual investigations into optimizing flight energy-maneuvering patterns for SR-HALE platforms.

The case-study SR-HALE vehicle total weight is 550 lbs with a wing area of 800 square-feet. It has a maximum power to weight ratio of 14.5 Watts/lb. The total wing area covered in solar cells is 75% of the wing's planform area, or 600 square-feet. The vehicle's power loading, a ratio of vehicle weight and reference area is based from the

solar cell surface area. The wing loading of 0.7 is still based on the wing's total planform area.

The center of gravity position is at the wing's 50% point of the wing chord and the elevator as a chord ratio of 0.11 and spans the full wing (98.4 ft). Table 3.5 is the summary of the stability and controllability derivatives from the analysis.

Table 3.5: SR-HALE Derivatives (per degree)\*

	$\alpha$	$\beta$	$p$	$q$	$r$	$\delta_e$	$\delta_{e3/4}$
$C_L$	0.0860	-0.0001	-0.0010	0.1304	0.0003	0.0005	0.0008
$C_Y$	0.0010	-0.0004	-0.0012	0.0002	0.0008	0.0000	0.0000
$C_l$	0.0005	-0.0023	-0.0106	0.0006	0.0038	0.0000	0.0000
$C_m$	-0.0234	0.0000	0.0003	-0.0475	-0.0001	-0.0003	-0.0004
$C_n$	0.0000	0.0000	-0.0011	0.0000	-0.0001	0.0000	0.0000
$C_{l-\beta}C_{n-r}/C_{l-r}C_{n-\beta}$	-0.0067	*values based on Pathfinder <sup>5</sup>					

The SR-HALE platform aerodynamic performance was plotted. Figure 3.8 provides the lift, drag and pitching moment characteristics for the vehicle, while Figure 3.9 demonstrates the vehicle's aerodynamic efficiencies.

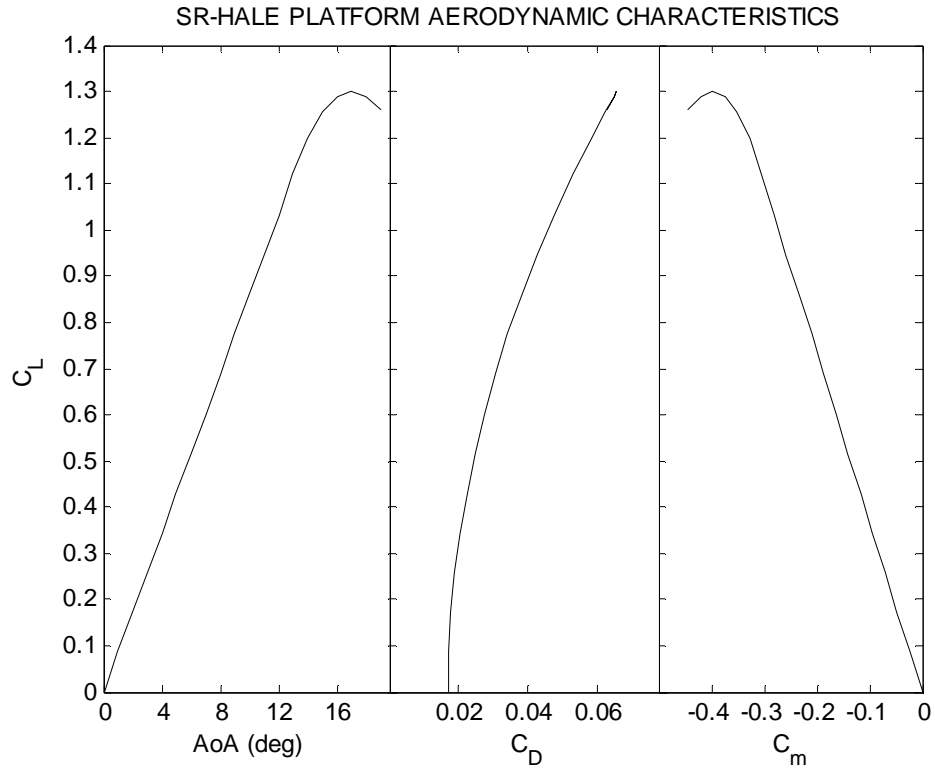


Figure 3.8: SR-HALE Aerodynamic Characteristics

The vehicle's maximum lift occurs ( $C_L = 1.3$ ) at an angle of attack of 17 degrees.

The maximum range based on aerodynamic parameters occurs at an angle of attack of 8.7 degrees with a maximum vehicle lift to drag ratio of 22.6. At this angle of attack the aerodynamic parameter for the endurance efficiency is 19.9. Aerodynamic endurance peaks at the maximum lift of the vehicle where flow stall is apparent – an unsound condition for sustained flight for any substantial amount of time.

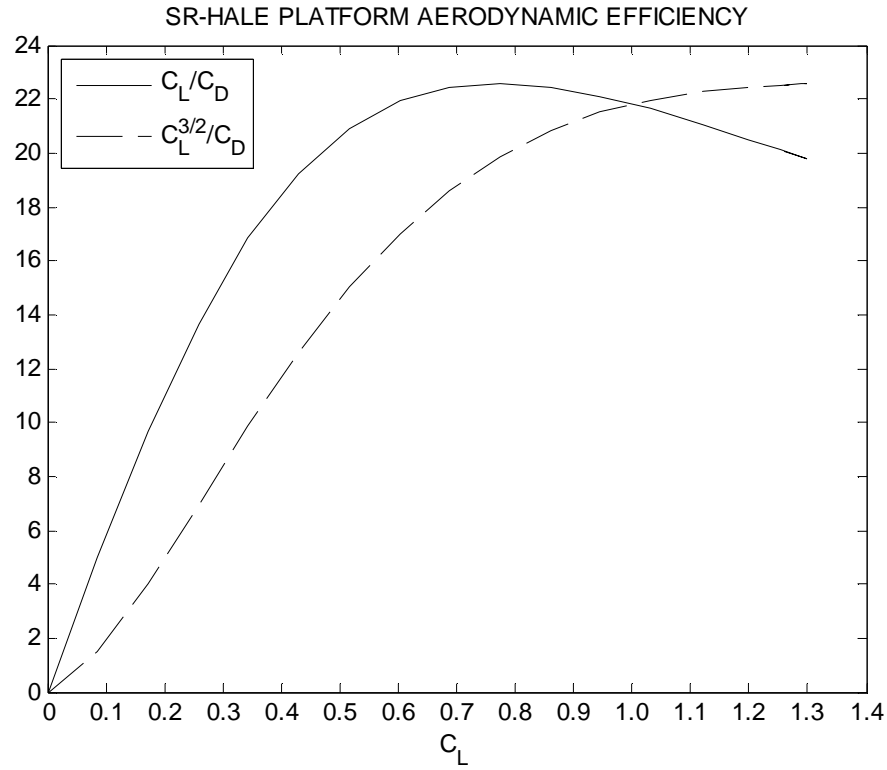


Figure 3.9: SR-HALE Aerodynamic Efficiency Characteristics

The SR-HALE flight mechanics discussed are used for the case-study platform fixed and energy-optimized flight pattern analysis.

Table 3.6 summarizes the vehicle geometry, flight conditions and selected performance parameters.

Table 3.6: SR-HALE Platform Performance Summary\*

SR-HALE Platform Performance Summary\*

Platform		Performance	
weight:	550.0 lbs	altitude:	60,000 ft
wing loading (W/S):	0.7 lbs/ft <sup>2</sup>	pressure:	151 lbs/ft <sup>2</sup>
power loading (W/S <sub>sp</sub> ) <sub>mx</sub> :	13.5 watts/ft <sup>2</sup>	temp:	-69.7 °F
		density:	0.000226 slug/ft <sup>3</sup>
Geometry		C <sub>D0</sub>	0.017
span:	98.4 ft	C <sub>Lmx</sub>	1.3
length:	12.0 ft	e	0.92
chord:	8.0 ft	(C <sub>L</sub> /C <sub>D</sub> ) <sub>mx</sub>	22.6 at C <sub>L</sub> = 0.75
AR:	12.0	(C <sub>L</sub> <sup>3/2</sup> /C <sub>D</sub> )	19.9 at C <sub>L</sub> = 0.75

\*values based on Pathfinder<sup>5</sup>

The SR-HALE vehicle has a straight wing composed of carbon composite spar, lightweight composite ribs and transparent plastic wing skin. The vehicle can withstand a maximum load factor of 3.2 g's.

## CHAPTER 4

### FLIGHT MANEUVERING PATTERNS

#### 4.1 Fixed Flight Maneuvers

Prior to determining optimal flight paths, consider two fixed flight maneuvers that can be used to obtain a general understanding of the available solar flux for flight at a constant altitude restricted within the flight window. The first maneuver consists of static on-station flight by orienting the vehicle into the high altitude winds and varying angle-of-attack. The second is sustained turning flight at a constant bank angle.

The following analysis consists of changing the latitude location and time-of-year. The summer and winter solstice, the maximum and minimum available daylight, as well as the equinoxes are shown for the variation in time-of-year. All other dependent variables, such as vehicle orientation and flight characteristics were examined at a  $40^0$  latitude, the case-study location latitude.

##### 4.1.1 Static On-Station

The static on-station maneuver correlates to a wind tunnel effect – where the vehicle is not moving relative to the AOI and the required lift for the vehicle is obtained by the oncoming high altitude winds. In order to obtain static on-station flight, the wind speeds will have to be greater than the stall velocity and not exceed the velocity for maximum available power of the HALE vehicle. However, before addressing the case-study analysis and the high altitude wind restrictions, first consider the available solar

intensity with the effects of vehicle orientation while varying the latitude and time of year.

The variation in the SR-HALE angle-of-attack angle while the platform is oriented in the four main cardinal directions are shown for a  $40^\circ$  latitude. Figure 4.1 and Figure 4.2 are with the platform facing north and south respectively.

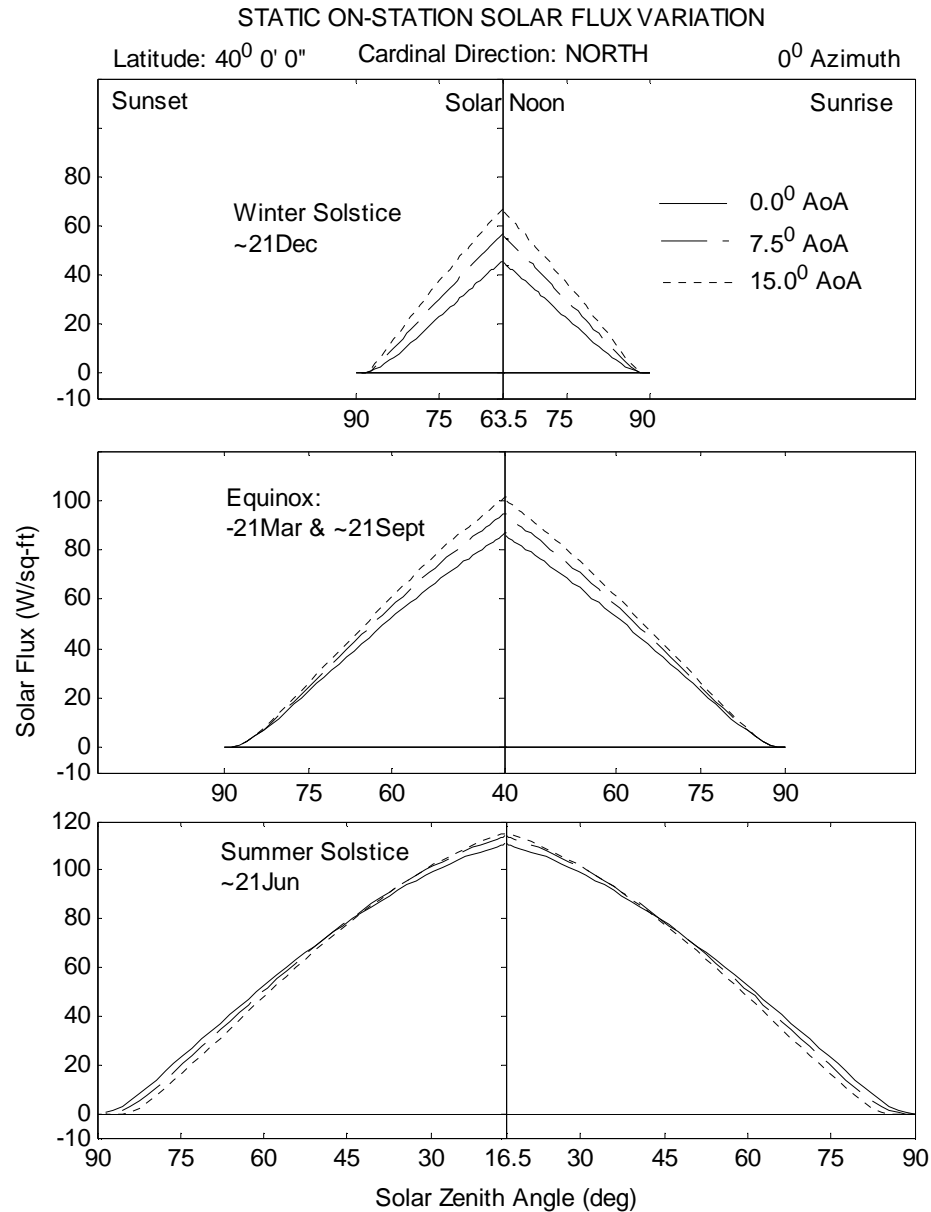


Figure 4.1: Static On-Station Solar Flux Variation at  $40^\circ$  Latitude: North



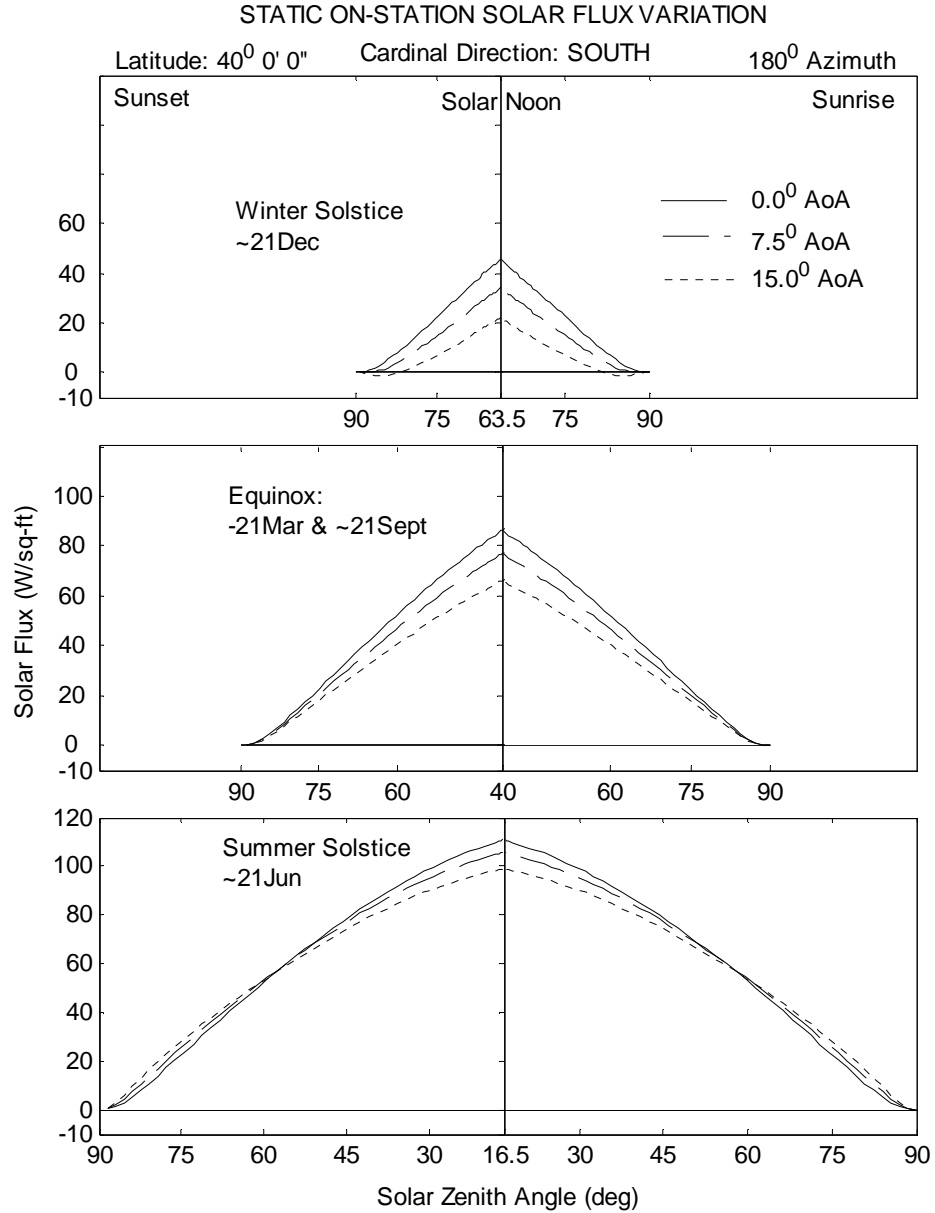


Figure 4.2: Static On-Station Solar Flux Variation at  $40^{\circ}$  Latitude: South

Figure 4.3 shows the available solar flux with the platform facing west. By rearranging the sunrise and sunset locations in Figure 4.3, the solar flux variation represents the platform facing an easterly direction.

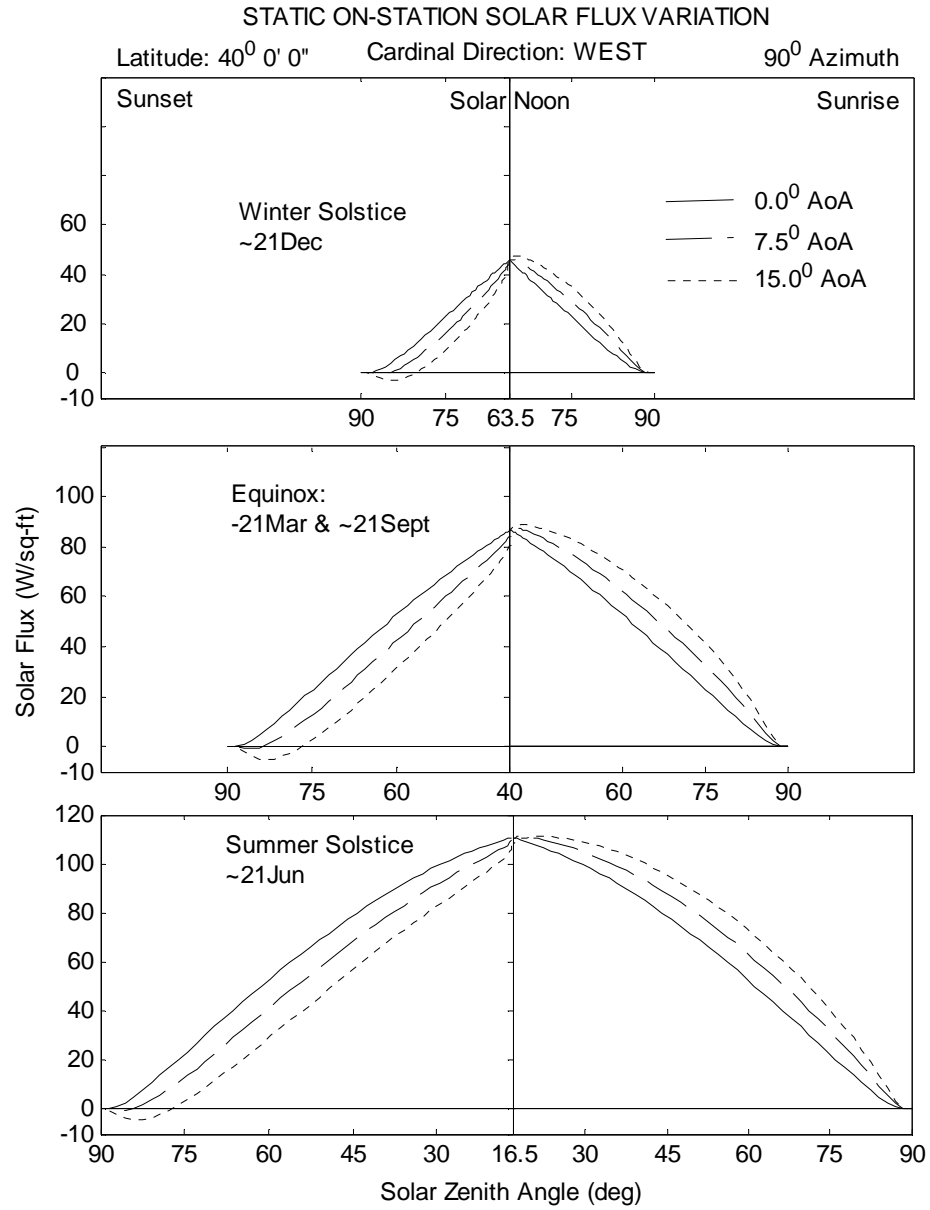


Figure 4.3: Static On-Station Solar Flux Variation at  $40^{\circ}$  Latitude: West

Figures 4.4 through 4.6 show the available solar flux for increase in latitude. To show the effects of the time-of-year, the solar flux starts at 90 degrees sunrise and returns to the same point graphically for sunset. This is evident in Figure 4.6 with the vehicle oriented toward the west. Similarly, by rearranging the sunrise and sunset line designations in the legend represents the platform facing in an easterly direction.

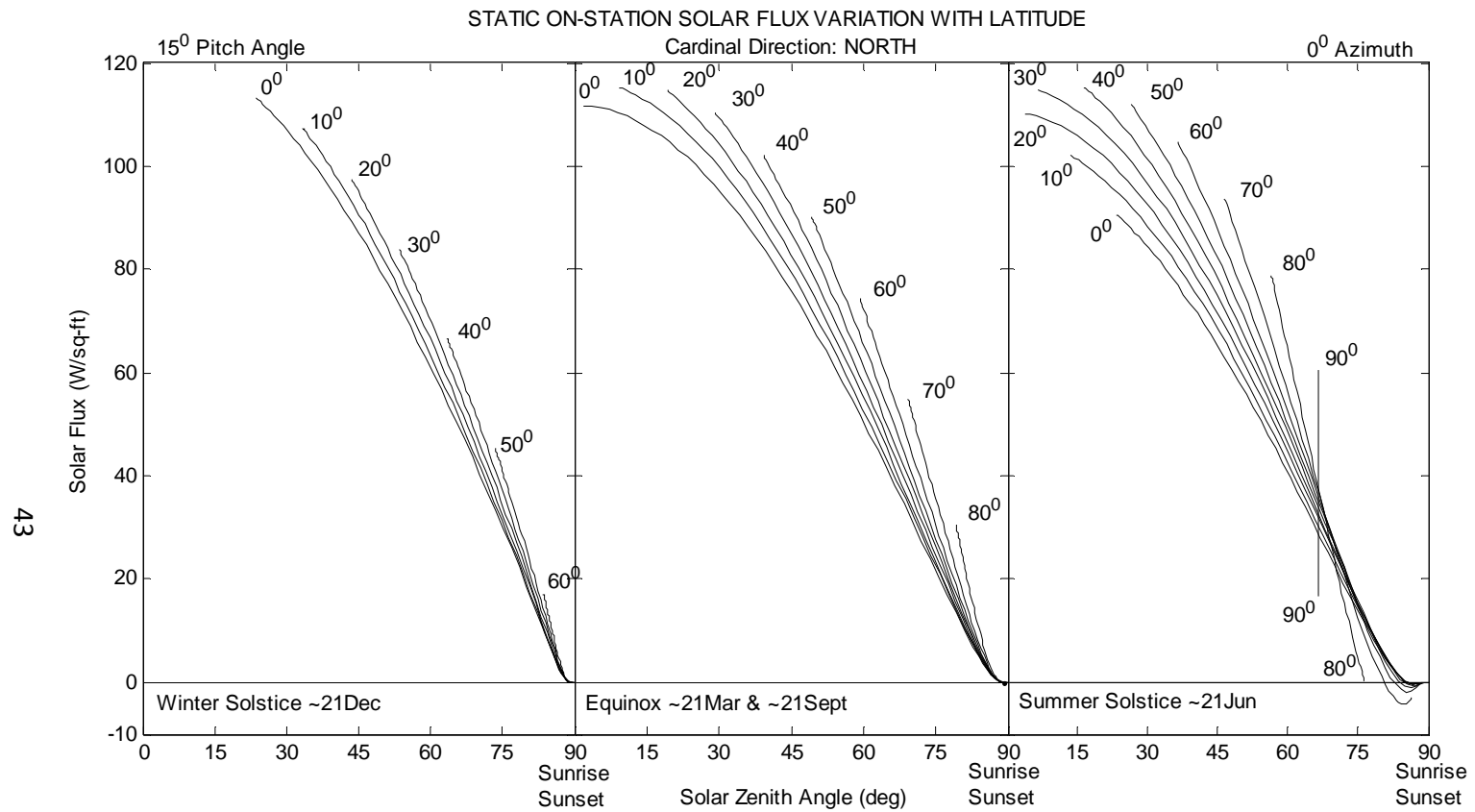


Figure 4.4: Static On-Station Solar Flux Variation with Latitude: North

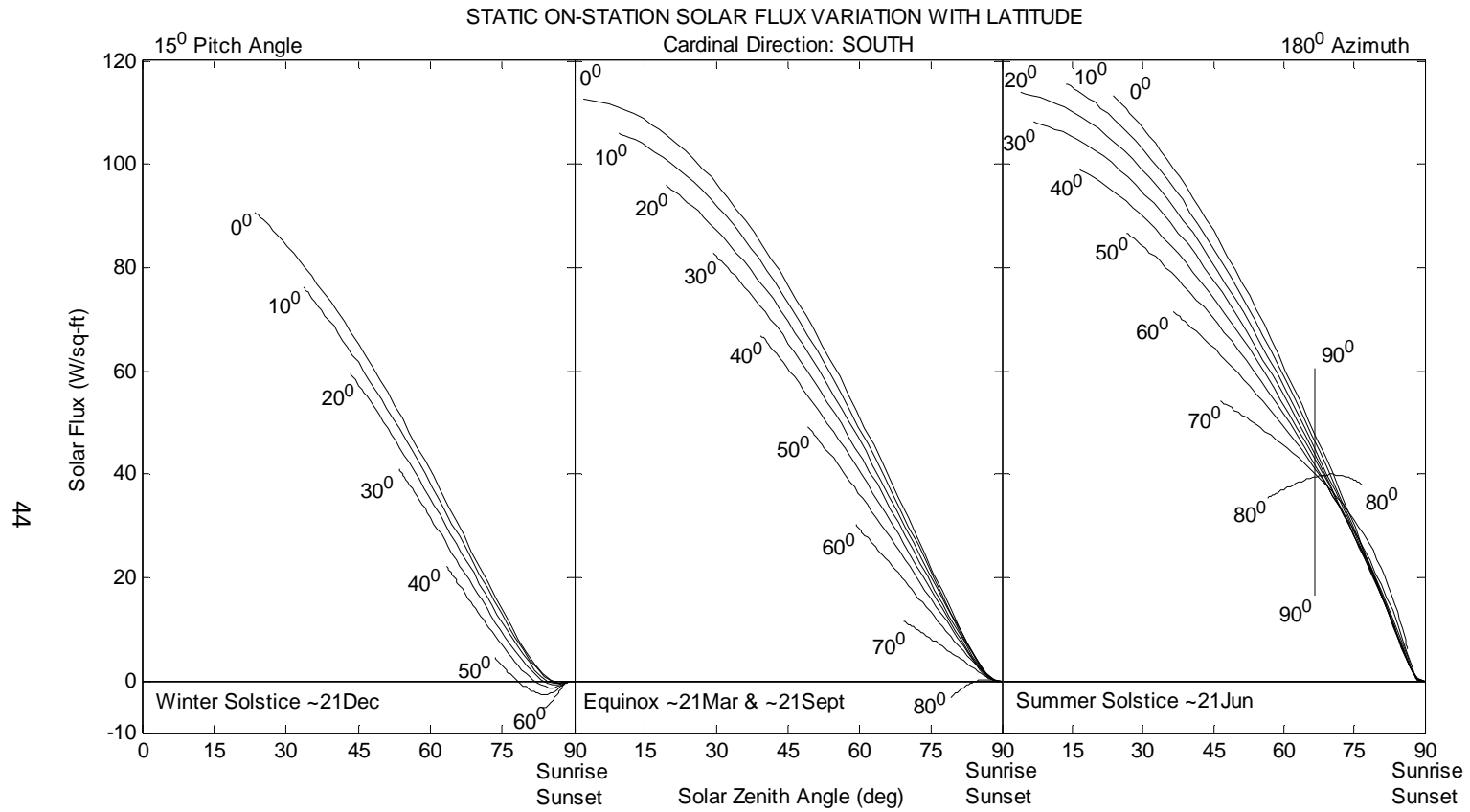


Figure 4.5: Static On-Station Solar Flux Variation with Latitude: South

Figure 4.6: Static On-Station Solar Flux Variation with Latitude: West

With the solar flux variations above, the total solar flux and averaged power available was determined for the static on-station flight, Figure 4.7.

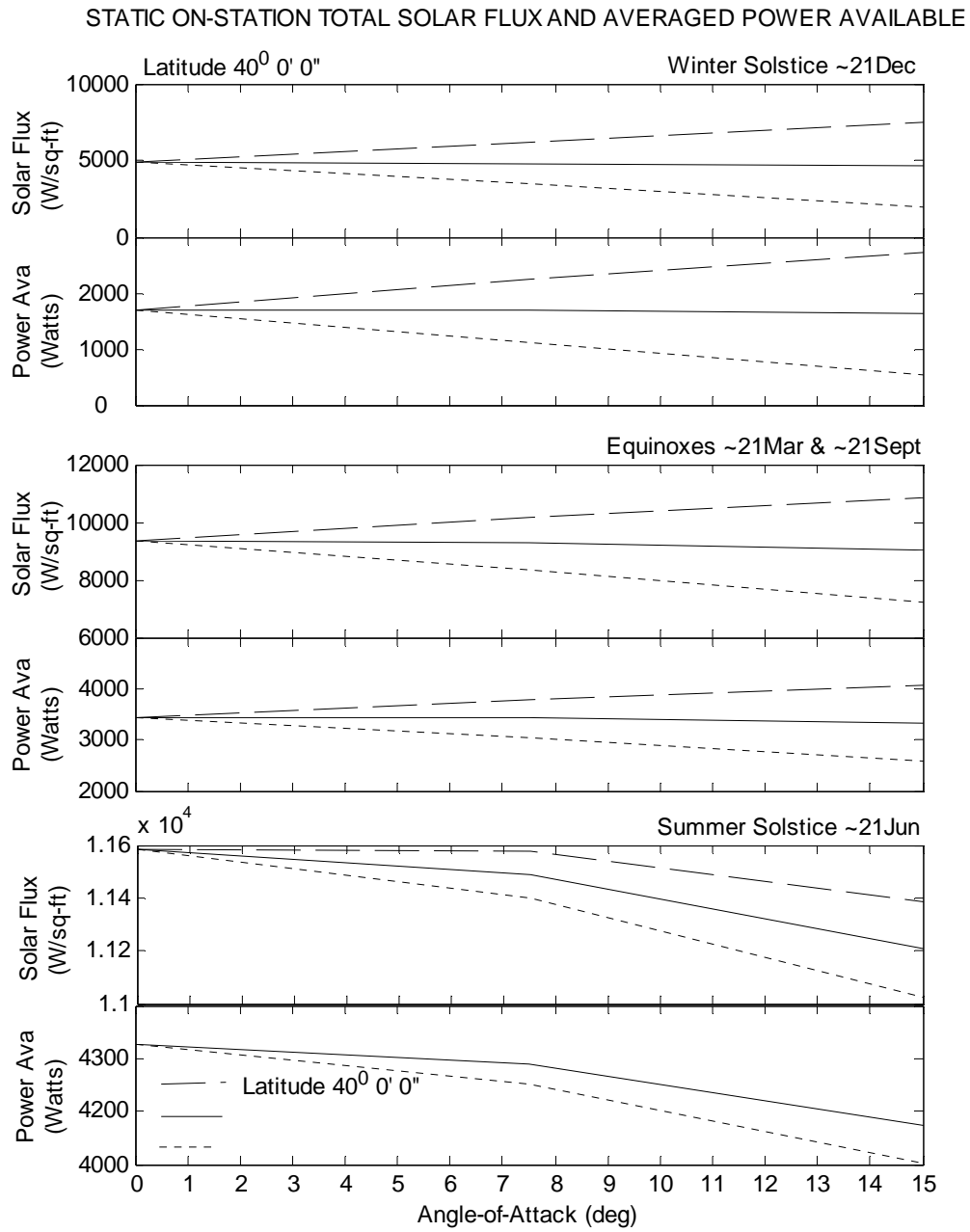


Figure 4.7: Static On-Station Total Solar Flux and Averaged Power Available

The total solar flux and averaged power available was determined for the AOI latitude of 40 degrees, with the vehicle facing the four cardinal directions. The results are equivalent for the vehicle facing east and west.

Considering the case-study SR-HALE platform, the static on-station requirements for the vehicle can be seen in Figure 4.8.

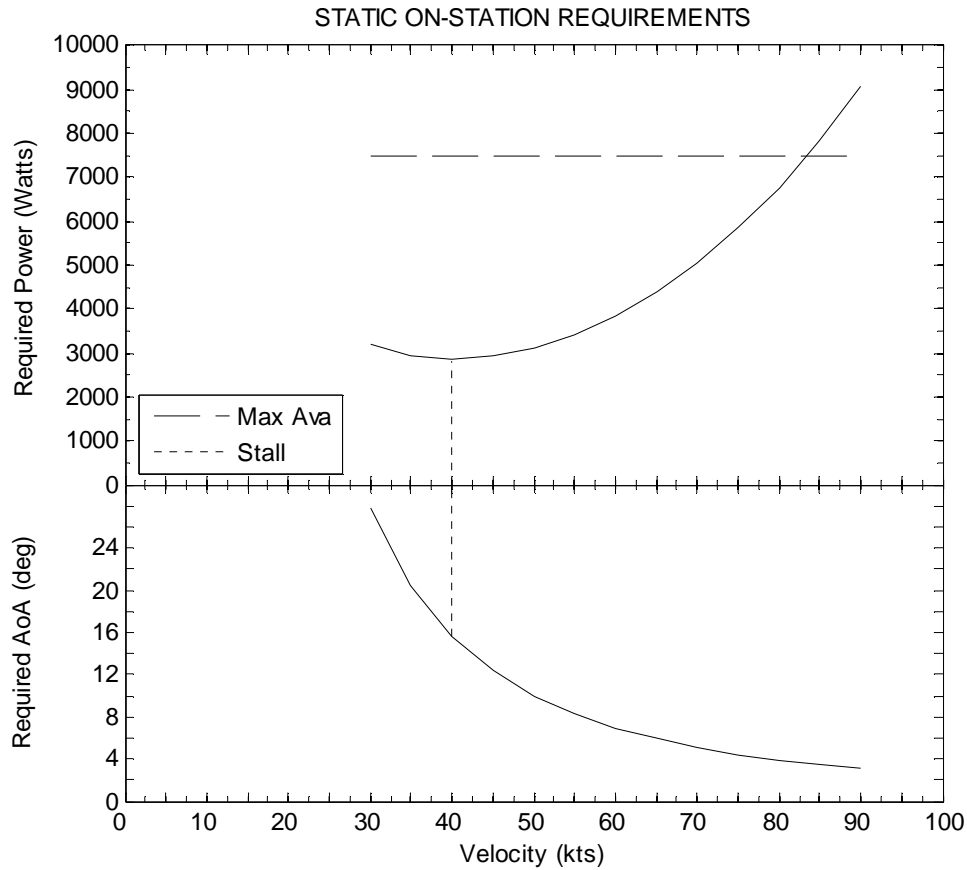


Figure 4.8: SR-HALE Static On-Station Required Power and Angle-of-Attack

The stall velocity for the vehicle is 40 knots and its maximum obtainable speed corresponding to the electric motor at full power draw at 7,500 Watts is 83 knots. Aforementioned, the high altitude wind speeds must remain within this range for the vehicle to maintain station keeping.

Referring to Table 3.4, the high altitude winds for the area of interest, it is evident that static on-station flight is possible during the winter season and only during the maximum wind speed conditions for the spring and fall seasons. The high altitude wind speed during the summer season is not sufficient in order to remain on-station.

However, the SR-HALE platform does not have enough storage system mass in order to maintain the required minimum power in order to maintain static on-station flight at a constant altitude during the winter months. Recall from section 3.4.2 that an assumed energy storage weight for the case-study vehicle was 125 lbs, allowing for 12.1 hours of use at a continuous draw of 3,000 watts. The AOI has slightly over nine hours of daylight (Table 3.2) during the winter solstice, exceeding the available stored energy during the 15 hours (night) of continuous use without solar recharge.

In summary, the case-study SR-HALE platform can only maintain static on-station flight over the AOI, during the fall and spring seasons with high altitude winds exceeding 40 knots and more than 12 hours of available daylight. Also, enough energy to maintain the necessary power during the low solar charge at sunrise is required, further limiting the static on-station flight. At all other instances the vehicle will be required to be moving forward in order to maintain flight.

#### 4.1.2 Sustained Turn Circle Pattern

The sustained turn can be considered a circle or loiter pattern and a logical choice for maintaining continual SA over an AOI. This flight pattern was selected as the baseline for D-O.P-P. Technique comparisons. The loitered flight has several dependent flight variables, such as the turn radius is set by the UAVs speed and bank angle. Therefore, consider the case-study SR-HALE platform required power in order to maintain a sustained turn, at various bank angles, shown in Figure 4.9. The maximum available power and the vehicle's stall velocity are plotted as well, showing the feasible velocity range for turning flight.



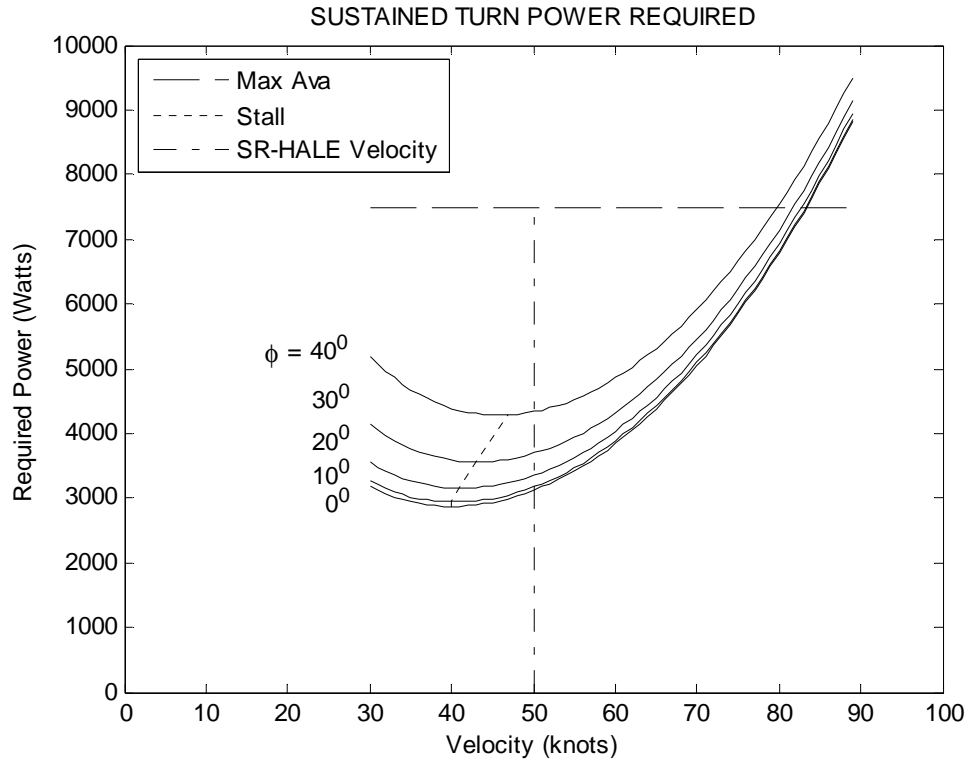


Figure 4.9: SR-HALE Sustained Turn Required Power

Referring to Figure 4.9, the minimum power required for sustained bank angles occurs at the vehicle's stall. Allowing for a 20% safety factor in vehicle speed above stall, the velocity for minimum power required for the SR-HALE UAV was set at a constant 50 knots. At this velocity the maximum aerodynamic efficiency for the vehicle was maintained at a lift coefficient of 0.85 and lift-to-drag ratio of 22 for level flight. The velocity setting also allows bank angles for the UAV up to 20 degrees without getting dangerously close to vehicle stall. With further increase in bank, the structural integrity along with vehicle stall would be of concern, especially with the vehicle's low wing loading. The minimum power required for the SR-HALE vehicle at 50 knots is shown in Figure 4.10, along with the corresponding turning radius.

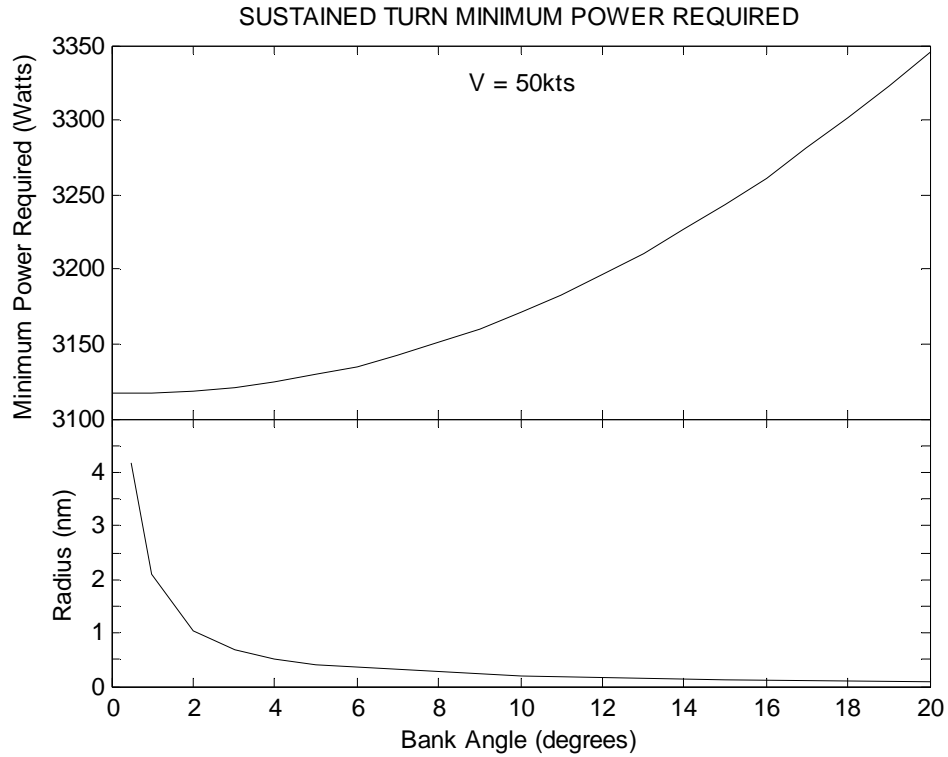


Figure 4.10: SR-HALE Minimum Sustained Turn Power Required – 50kts

At 50 knots the vehicle requires an angle-of-attack of 10 degrees. While the bank angle is increased to its maximum limit of  $\pm 20$  degrees, the required change in lift and therefore change in angle-of-attack for constant speed is less than half of degree. This minimal change was ignored for the analysis; and the angle-of-attack was assumed a constant 10 degrees and accounted for in the surface obliquity tilt angles for determining the solar flux. Figure 4.11 shows the sustained turn analysis for the SR-HALE UAV for varying the bank angle at latitude of 40 degrees, the case-study location.

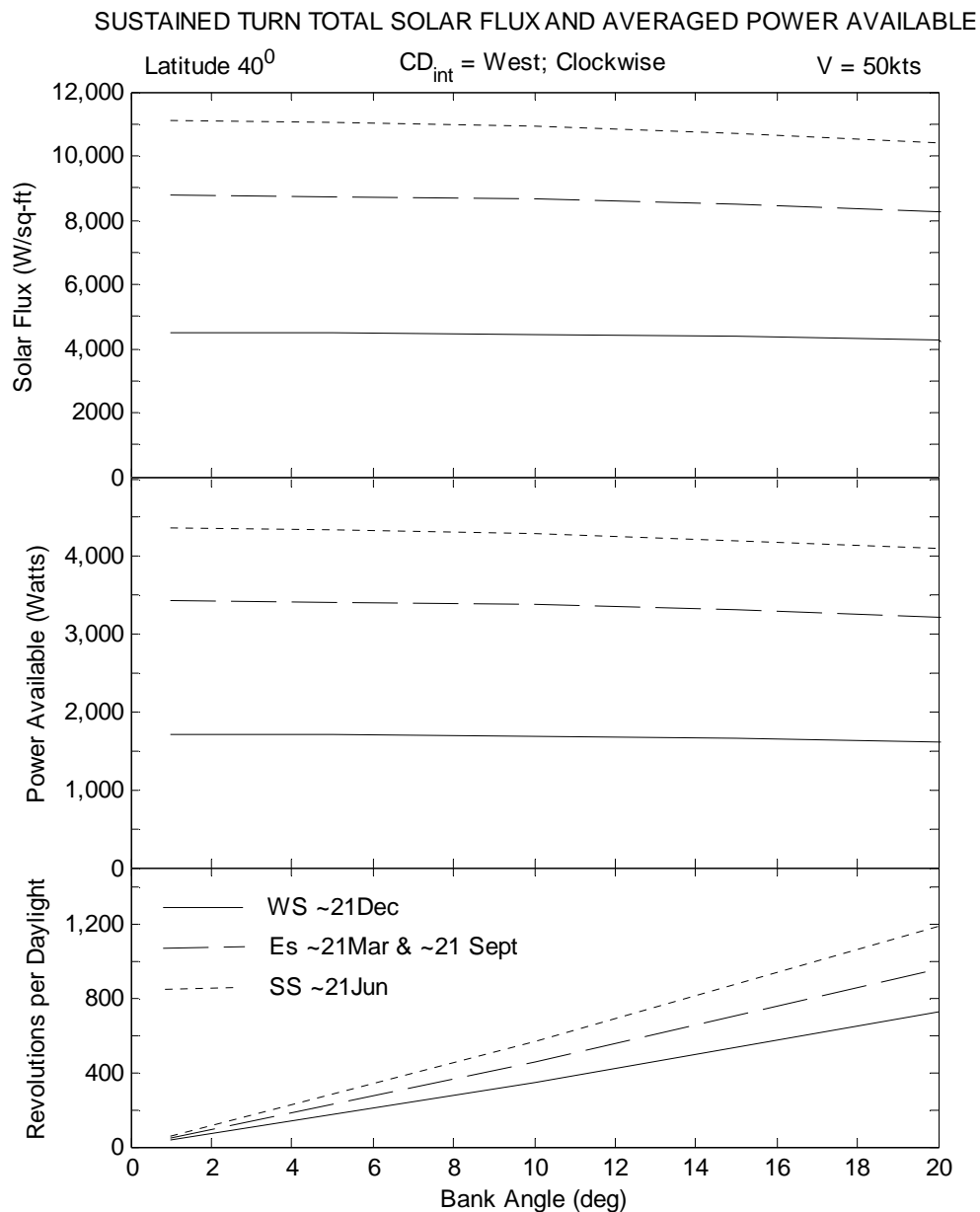


Figure 4.11: Total Sustained Turn Solar Flux and Available Power

The above figure shows the total solar flux and corresponding averaged power available for the winter and summer solstices and equinoxes; as well as the Revolutions per Daylight (RPDL) for constant speed flight. The vehicle was initially at the West Cardinal Direction ( $CD_{int}$ ) and rotating clockwise at a constant flight speed of 50 knots. Comparing the averaged available power of Figure 4.11 to the power required for flight

in Figure 4.10, it can be seen that the representative SR-HALE UAV does not gather enough solar power during the winter solstice to maintain flight; and limited during the equinox times-of-year.

The other parameters of interest when considering sustained turn circle pattern flight is the initial starting location at sunrise and the direction, clockwise ( $D_C$ ) or counterclockwise ( $D_{C-C}$ ). However when considering these parameter and due to the fact that the SR-HALE UAV has high revolutions per daylight the effects are inconsequential. This can be seen in Table 4.1 below

Table 4.1: Total Sustained Turn Solar Flux with Initial Start Location

<b>Sustained Turn Flight</b>	Latitude	40 deg		
0.10nm Radius	V	50 knts		
	φ	20 deg		
<b>Total Solar Flux (W/sq-ft) [Averaged Ava Power (Watts)]</b>				
Initial Start Location at Sunrise				
N	S	E	W	RPDL
<i>Winter Solstice ~21Dec</i>				
D <sub>C</sub>	<b>4232 [1604]</b>			728
D <sub>C-C</sub>	<b>4232 [1604]</b>			728
<i>Equinoxes ~21Mar &amp; ~21Sept</i>				
D <sub>C</sub>	<b>8240 [3216]</b>			955
D <sub>C-C</sub>	<b>8240 [3216]</b>			955
<i>Summer Solstice ~21Jun</i>				
D <sub>C</sub>	<b>10421 [4093]</b>			1182
D <sub>C-C</sub>	<b>10421 [4093]</b>			1182

The vehicle conditions were sustained 20 degree bank angle at a constant 50 knots over the case-study location. The initial vehicle locations at sunrise were the four main cardinal directions; North, South, East, and West. With a turning radius of 0.10 nautical-miles (608 ft), notice the high RPD<sub>L</sub> and range over the time-of-year for the SR-HALE UAV. This is evident by observing the solar flux variation from sunrise to sunset for the vehicle in a sustained turn. Figure 4.12 shows the solar flux variation for the solstices and equinoxes.

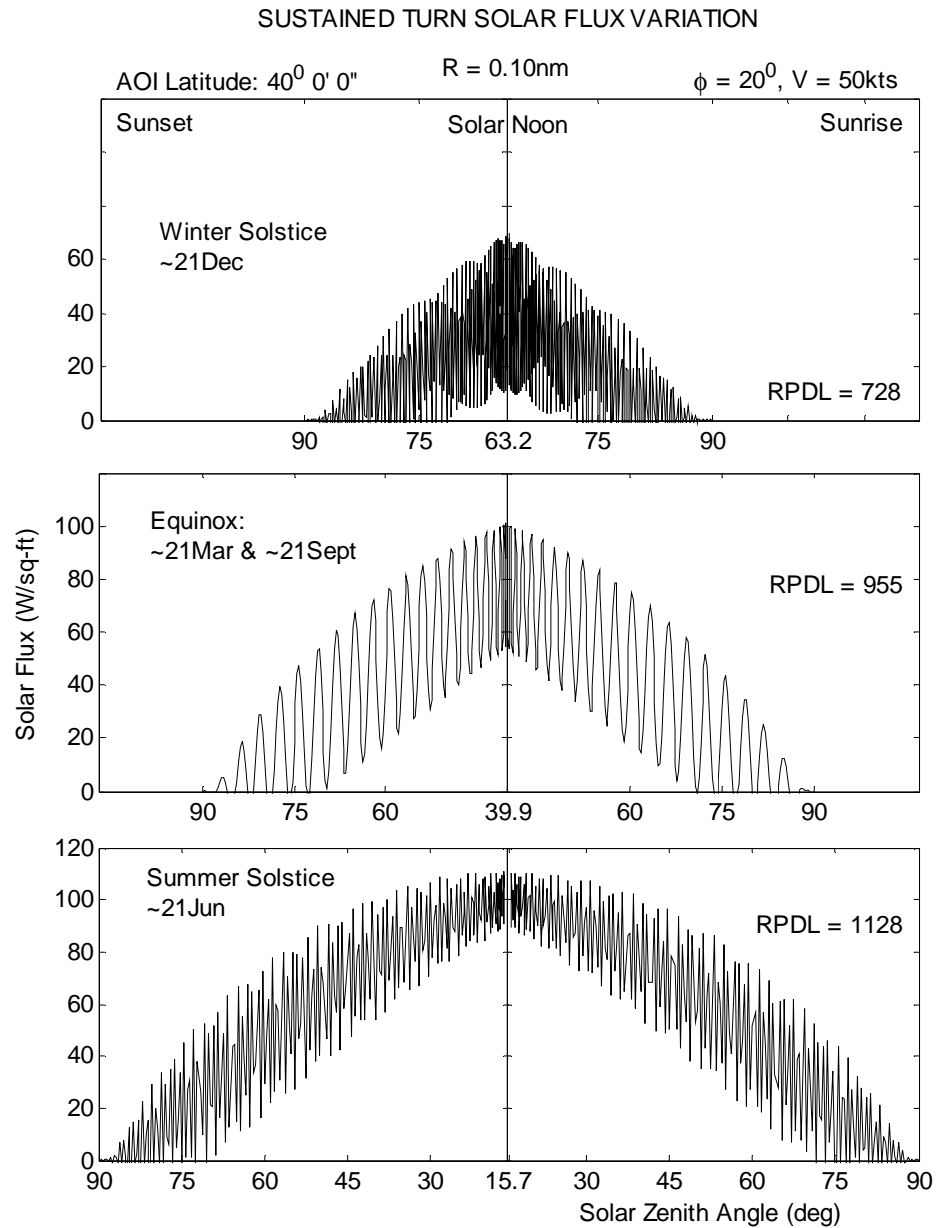


Figure 4.12: Sustained Turn Solar Flux Variations

The revolutions per daylight are shown for each time-of-year. The total solar fluxes listed in Table 4.1 are the integrand of solar flux variation of the above figure. Changing the initial cardinal direction at sunrise the solar flux frequency and peak magnitudes are maintained, with different sunrise conditions.

Considering the changes in latitude, the total solar flux and averaged available power, along with the revolutions per daylight for the SR-HALE UAV can be seen in Figure 4.13.

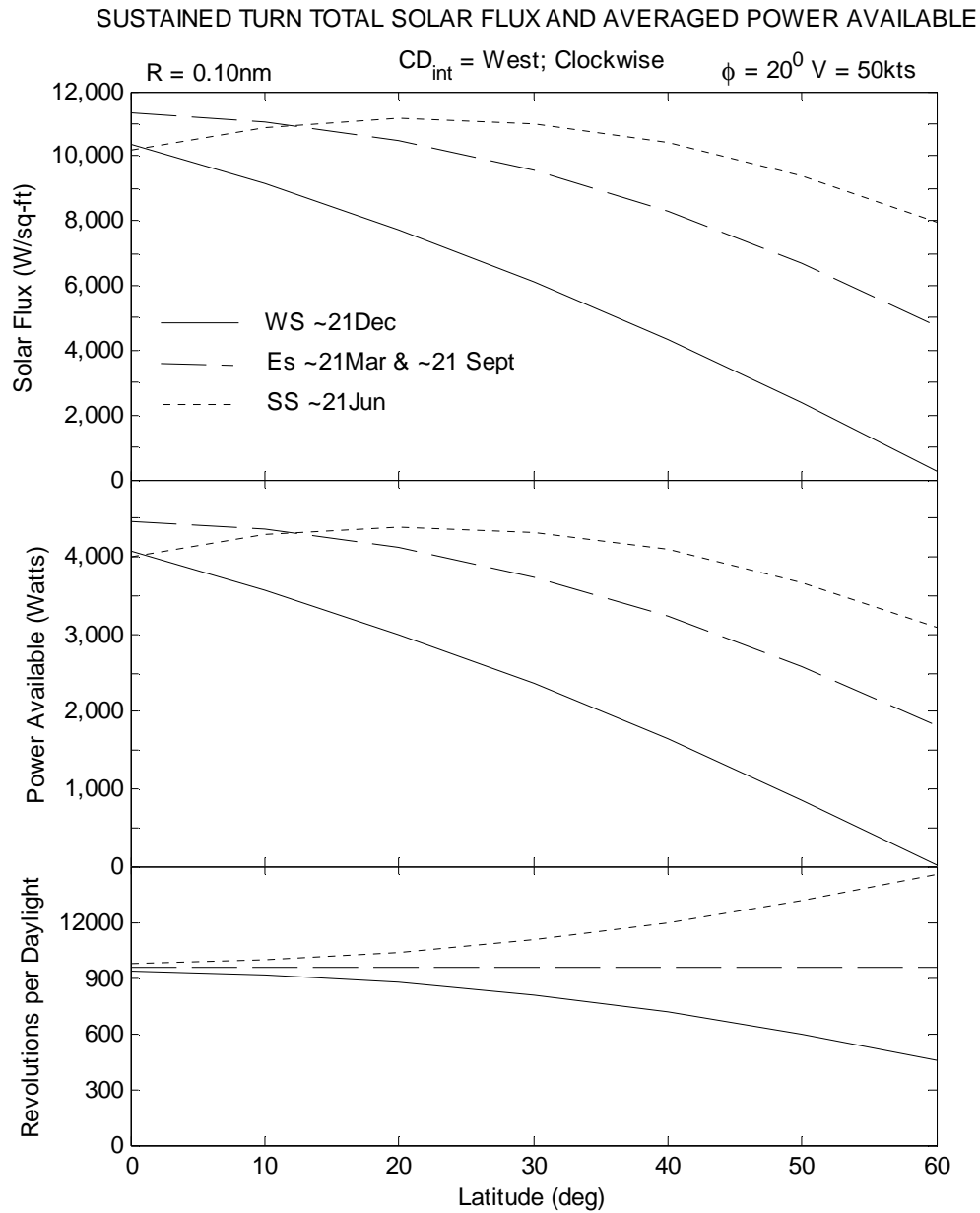


Figure 4.13: Total Sustained Turn Solar Flux and Available Power – Latitude Variations

The flight conditions are consistent with the previous analysis, 20 degree bank angle at a constant 50 knots. Recall that the power required for the vehicle, from Figure 4.9 is 3350 Watts for the bank angle. The requirement limits the possible sustained turn, loiter flight for the SR-HALE UAV in maintaining SA, especially during the winter solstice, where there is only sufficient power for latitudes ranging from the equator to approximately 15 degrees.

## 4.2 Optimum Flight Maneuvering

The vehicle kinematics and modeling techniques are developed using the previous analysis. The focus was on acquiring an accurate and simplified, when valid, model for on-line adaptive capability in determining flight paths.

### 4.2.1 UAV Kinematics

The SR-HALE kinematic modeling considered is shown below (4-1). The vehicle is at a constant altitude, speed ( $V$ ) and angle-of-attack. Analysis was done for both still air ( $V_w=0$ ) and for constant wind velocity, with  $V < V_w$ .

$$\begin{bmatrix} x \\ y \\ \psi \end{bmatrix} \quad \begin{bmatrix} \dot{x} \\ \dot{y} \\ \dot{\psi} \end{bmatrix} = \begin{bmatrix} V \cos \psi + V_{wx} \\ V \sin \psi + V_{wy} \\ (g/V) \tan \phi \end{bmatrix} \quad (4-1)$$

The position and orientation of the vehicle is given by the Cartesian coordinates,  $x$  and  $y$ , vehicle heading  $\psi$  and bank angle  $\phi$ .

By introducing the bang-level-bang technique for vehicle control, the dependence on inertial roll rate and its effect to surface obliquity is eliminated in the near time control for vehicle orientation to meet its Driven determined position and orientation. This simplification assumes that the vehicle has the ability to instantaneous reach a new bank angle and is common in flight vehicle trajectory analysis. Furthermore, the nature of the

SR-HALE flight driven window orientation for solar power does not require large changes in vehicle bank angle, eliminating the need for large roll rates, further validating the assumption made.

#### 4.2.2 D-O.P-P. Modeling & Procedure

Recall that the objective was to determine the minimum required power flight paths to the predetermined location and orientation for obtaining maximum solar flux established by the ‘driver.’ Along the available window of flight of longitude and latitude location in the inertial frame of reference, the solar flux was maximized for the corresponding vehicle bank angle and heading angle. The direct effect of solar flux was used, not accounting for the small contribution of diffusion. However, by maximizing the direct flux, the flux due to diffusion is inherently maxed, refer to Figure 3.3. The heading angle was transformed into the inertial frame of reference, including the effects of vehicle angle-of-attack. The flight window and objectives can be seen below in Figure 4.14.



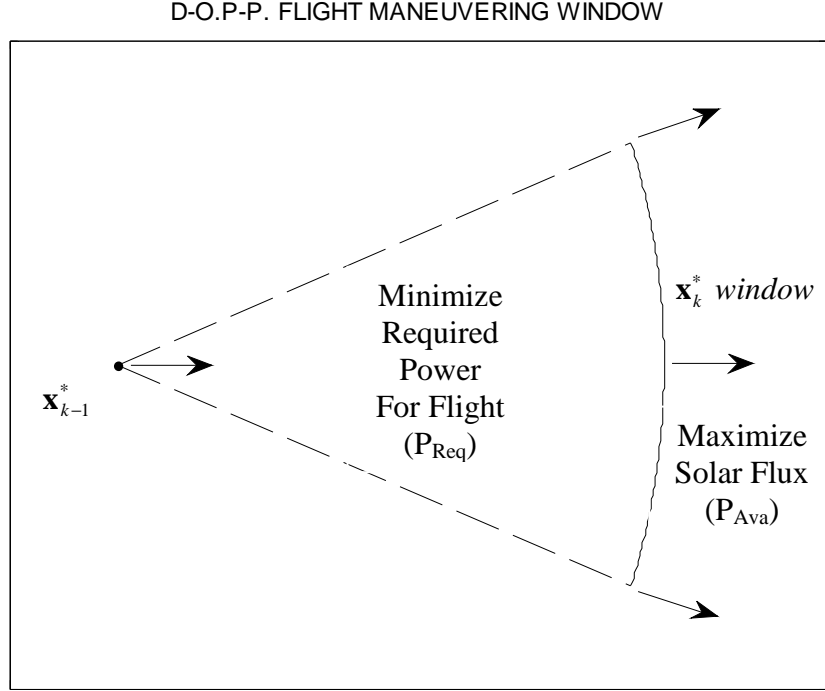


Figure 4.14: SR-HALE Flight Maneuvering Window and Objectives (2-D)

Referring to Figure 4.9 and allowing for a 20% safety factor in vehicle speed above stall, the velocity for minimum power required for the SR-HALE UAV was set at a constant 50 knots, consistent with sustained turn loiter flight. The constant velocity flight satisfies the minimum power required, simplifying the path-planning process; and maximizing aerodynamic efficiency for the vehicle in level flight with a constant angle-of-attack of 10 degrees. The minimum power required for the SR-HALE vehicle at 50 knots was shown in Figure 4.10.

Considering the discussed modeling for the vehicle path-planning, Table 4.2 below is the D-O.P-P. Technique for the representative SR-HALE UAV.

Table 4.2: SR-HALE UAV D-O.P-P. Technique

**Driver:**

$$\text{Maximize } F^{(direct)} = S_0 \mu e^{-\tau/\mu_0} ;$$

$$S_0 \equiv \text{Solar Constant}$$

$$\tau \equiv \text{Optical Thickness}$$

$$\mu_o = \cos Z \equiv \text{Solar Zenith}$$

$$\mu = \cos \theta \equiv \text{Surface Obliquity}$$

$$\cos \theta = \cos Z \cos \Delta + \sin Z \sin \Delta \cos(A - \psi)$$

$$\text{Subject to: } g_1 = |\phi_{mx} - \phi| \geq 0 ;$$

with b.c.

$$g_2 = (\text{Longitude} - \text{Longitude}_{AOI})^2 - (\text{Latitude} - \text{Latitude}_{AOI})^2 \leq R_{R-o-S}^2$$

with solution:

$$\mathbf{x}_k^* = (\phi_k^*, \psi_k^*, \Psi_k^*, \text{Longitude}_k^*, \text{Latitude}_k^*), \quad (k = 1, \dots, N)$$

**Path:**

$$\text{Minimize } P_{req}(u) = J(u) = \int_0^T f_0(\mathbf{x}(t), u(t)) dt ,$$

where

$$\mathbf{x}(t), (\mathbf{x}_{k-1}^*(t), \dots, \mathbf{x}_k^*(t)): [0, T] \rightarrow \mathfrak{R}^n$$

is the solution of the differential system with boundary conditions and with initial and final conditions

$$\frac{d\mathbf{x}_j}{dt} = f_j(\mathbf{x}, u(t)), \quad (j = 1, \dots, n);$$

$$\mathbf{x}(0) = \mathbf{x}_{k-1}^*; \quad \mathbf{x}(T) = \mathbf{x}_k^*$$

where

$$J(u^*) = \min_{u \in U} J(u)$$

with  $u^*$  and the associated path  $\mathbf{x}$  called 'optimal.'

The ‘driver’ conditions are constrained by the bank angle ( $g_1$ ); with the objective of maximizing solar flux (solar power) throughout the vehicle’s flight window when considering surface tilt ( $\mu$ ) at that specific time of day ( $\mu_0$ ). The second constraint, boundary condition, assures that the vehicle stays within the defined range-of-sight window over AOI. The maximum solar power is determined and sets the destination for the vehicle’s path. The ‘path’, in the case of the SR-HALE UAV is simplified by the constant velocity condition for minimizing power required for flight. The initial ( $\mathbf{x}_{k-1}^*$ ) and final (step,  $\mathbf{x}_k^*$ ) destination for the vehicle is flown by a constant radius of curvature trajectory set by the ascertained bank angle ( $\phi_k^*$ ) for the vehicle’s ‘driver’ optimum destination.

The procedure for the on-line analysis requires a total of six updating adaptive processes from sunrise to sunset. The flow of processes can be seen below, Figure 4.15.

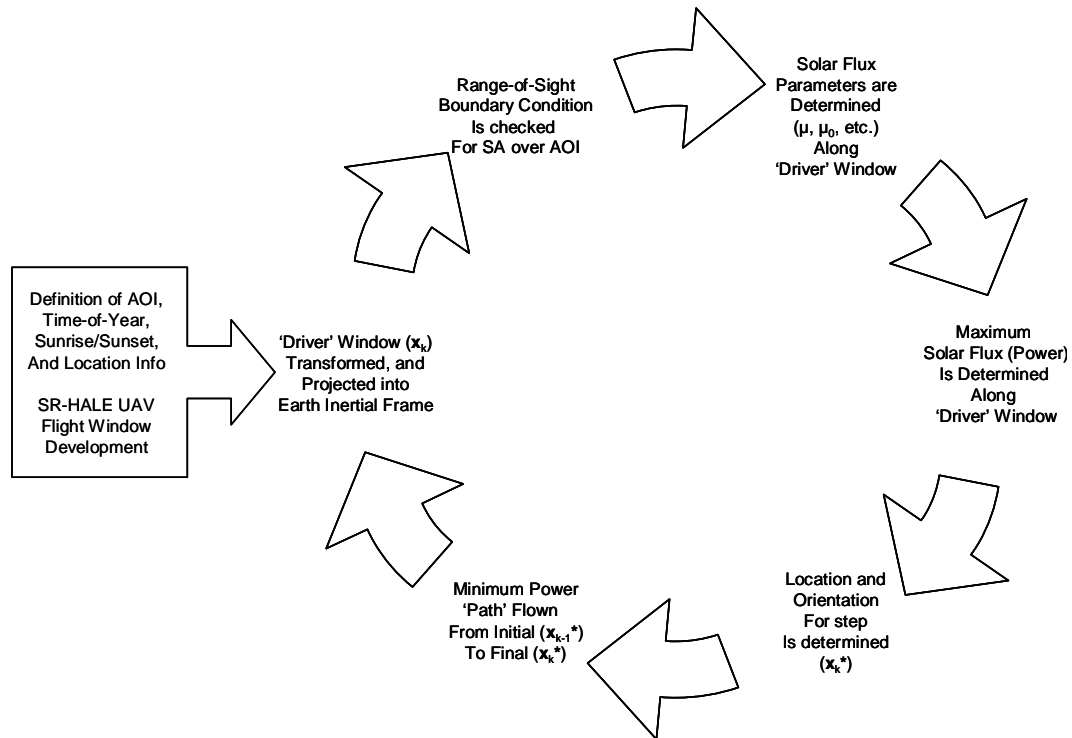


Figure 4.15: SR-HALE D-O-P-P. Flow Chart

The first requires the definition of AOI, with equation of time, the solar and geocentric coordinates, and hours of daylight including sunrise/sunset location for the time-of-year of interest. The second, independent process is the definition of the available flight window based on the SR-HALE UAV kinematics and the user defined radius of flight window for the ‘driver’ window objective analysis. The first ‘driver’ objective constraint ( $g_1$ ) limits the maximum bank angle of the vehicle. Next, the flight window, AOI, and time-of-year information is combined and transferred into the Earth inertial frame of reference. The second boundary condition constraint ( $g_2$ ) for the ‘driver’ objective insures that the UAV stays within the available range-of-sight for continual surveillance over the AOI. Parameters for solar flux measurements are determined along ‘driver’ window. Following, the available solar flux along with the vehicle flight window is determined. The SR-HALE UAV maximum solar flux ‘driver’ objective is then determined using an adaptive-A\* search procedure in determining the necessary parameters  $\mathbf{x}_k^*$  conditions to be met. That information is then used to determine flight path for minimum power required in order to meet the forward step destination and vehicle orientation. This process is iterated from initial location at sunrise through sunset.

This process is ‘locally’ optimal for increasing the adaptability and on-line capability for multi-objective approach for SR-HALE flight. It is possible for a ‘best’ path from an off-line analysis, using PSO or Evolutionary approaches that can be selected for the vehicle’s path. The D-O.P-P. Technique only projects forward one step at a time until the overall goal is met. The D-O.P-P. Program Interface and further discussion is within the attached Appendix.

As an example of the local optimality and the pros and cons consider the SR-HALE UAV directly over the AOI and initially heading north at sunrise. Figure 4.16 below shows path of the vehicle for the first few 50 minutes of flight. Further discussion on the ‘driver’ window projection distance, i.e. number of ‘driver’ objective iterations, and the effects are addressed in the following section.

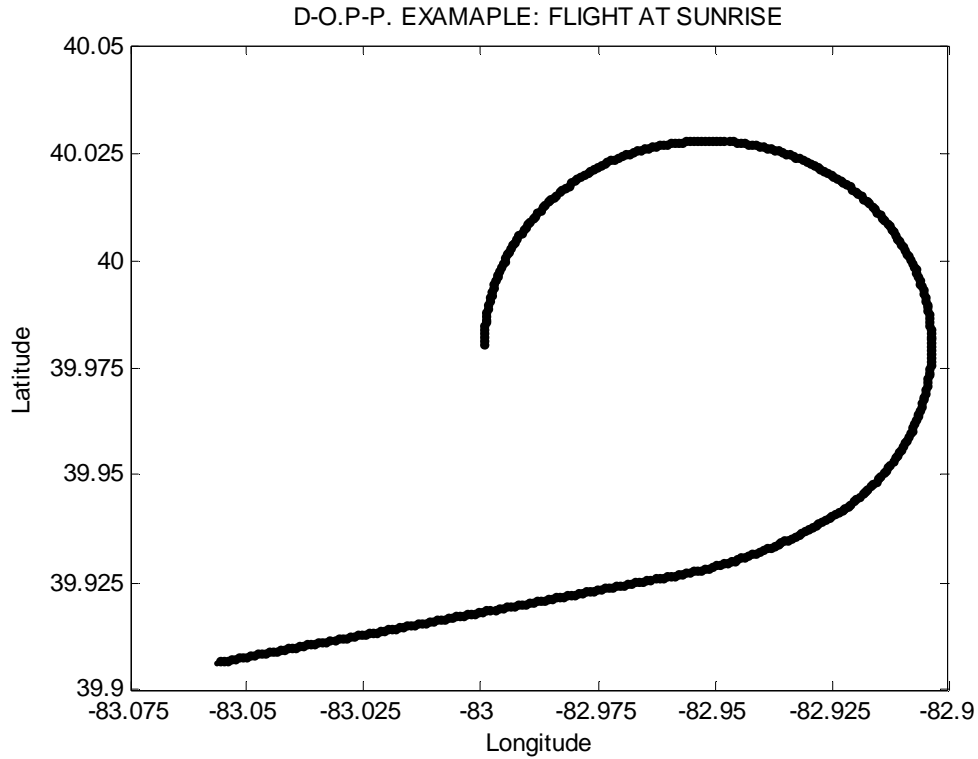


Figure 4.16: D-O.P-P. Example: Flight at Sunrise

The vehicle has a Northerly initial heading for the example figure, during sunrise. In order to obtain a maximum amount of solar flux, the SR-HALE UAV banks a positive 20 degrees, leaning the upper solar panel wing surface into the sun's intensity. Even though the technique is maximizing solar flux at each step, because it does not project meta-paths, like an off-line analysis, it is limited to a single flight trajectory. The result with starting on a single path may require compromise to reach the end goal. Within the SR-HALE flight, this was shown with solar flux. For the flight duration shown above the vehicle starts a sustained turn flight banking the solar panel surface into the sun, but as it projects further along the flight path there is a decrease in maximum solar flux. However, the D-O.P-P. Technique adapts and quickly brings a change to the flight trajectory to further increase the maximum solar flux. This can be seen in Figure 4.17, below, in the maximum solar flux variation for the example flight of Figure 4.16.

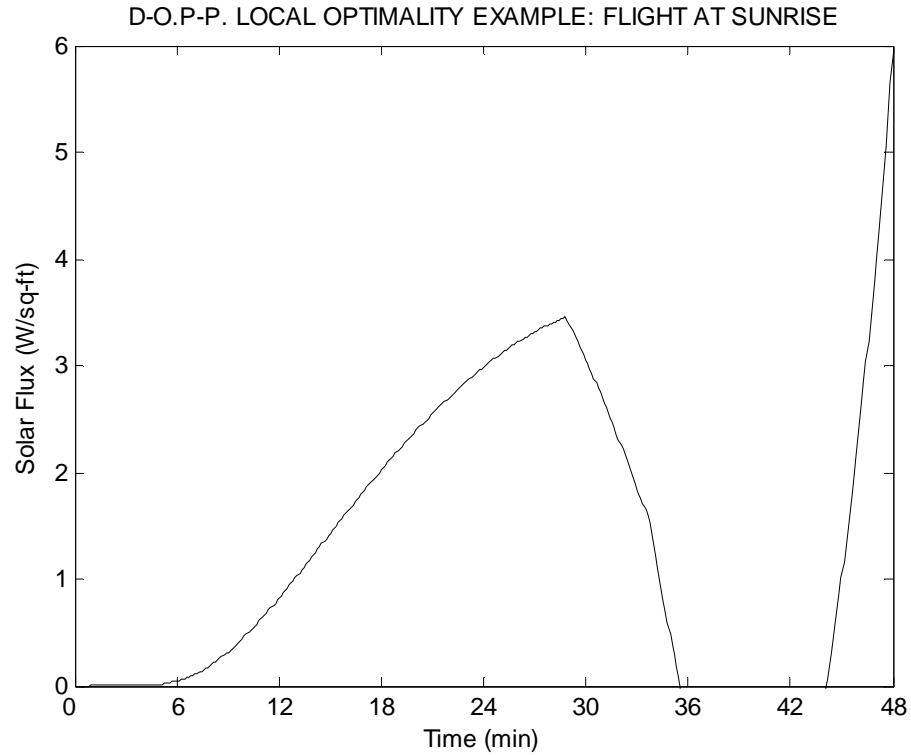


Figure 4.17: D-O.P-P. Example of Local Optimality Process: Sunrise

The small amount of max obtained solar flux is due to the nature of the given example during sunrise when the sun is low in the sky, or at a near 90 degree zenith angle.

Predicting further steps ahead, to determine, by selecting an alternate (non-optimal) destination that there may be alternate paths in which overall produces more solar power, would require an off-line analysis. This process voids the purpose of introducing adaptability in furthering UAV-autonomy.

### 4.3 Results & Discussion

Further the example sunrise flight given above, consider the full day of flight on the summer solstice ~21 June. The initial location of the vehicle was set directly over the AOI and heading north. Figure 4.18 below shows the flight pattern, with and without the

range-of-sight boundary correction of the SR-HALE UAV for the entire day. The path in red is in violation of the second boundary condition constraint. Implementing the constraint requires the vehicle to bank hard right and maintains continual SA over the AOI.

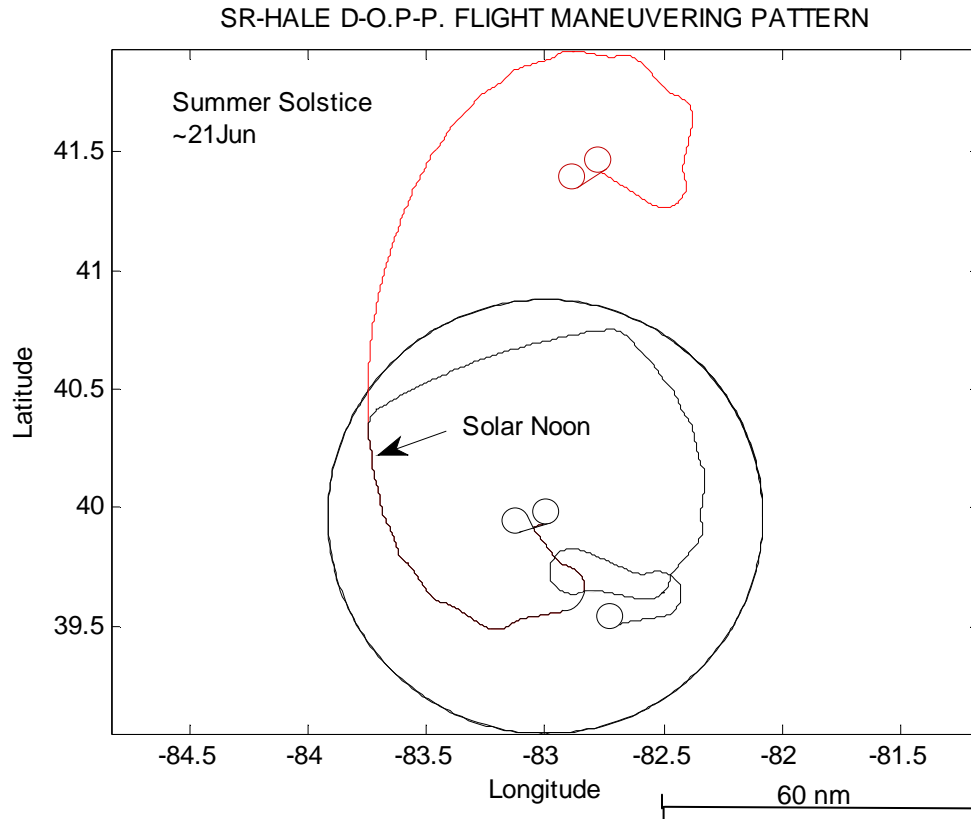


Figure 4.18: SR-HALE D-O.P-P. Flight Pattern – Summer Solstice

As discussed previously, the figure shows that during sunrise ( $Z = 90^\circ$ ) the vehicle is in a sustained bank. As the solar zenith angle decreases the vehicle path requires less sustained banking flight to orient the solar panel surface into the sun's rays for solar power. The total solar flux gather for the day was 12,838 Watts/sq-ft, an averaged available power of 5,100 Watts. When compared to the baseline loiter, sustained turn flight at a 20 degrees bank angle, this resulted in a 19.7% increase in averaged available power; and a -2.0% decrease in power required for flight.

To obtain a better understanding, consider the solar flux variation from sunrise to sunset for the D-O.P-P. flight pattern compared to the baseline sustained turn, Figure 4.19. The winter and summer solstice and equinox(s) times-of-year were considered.

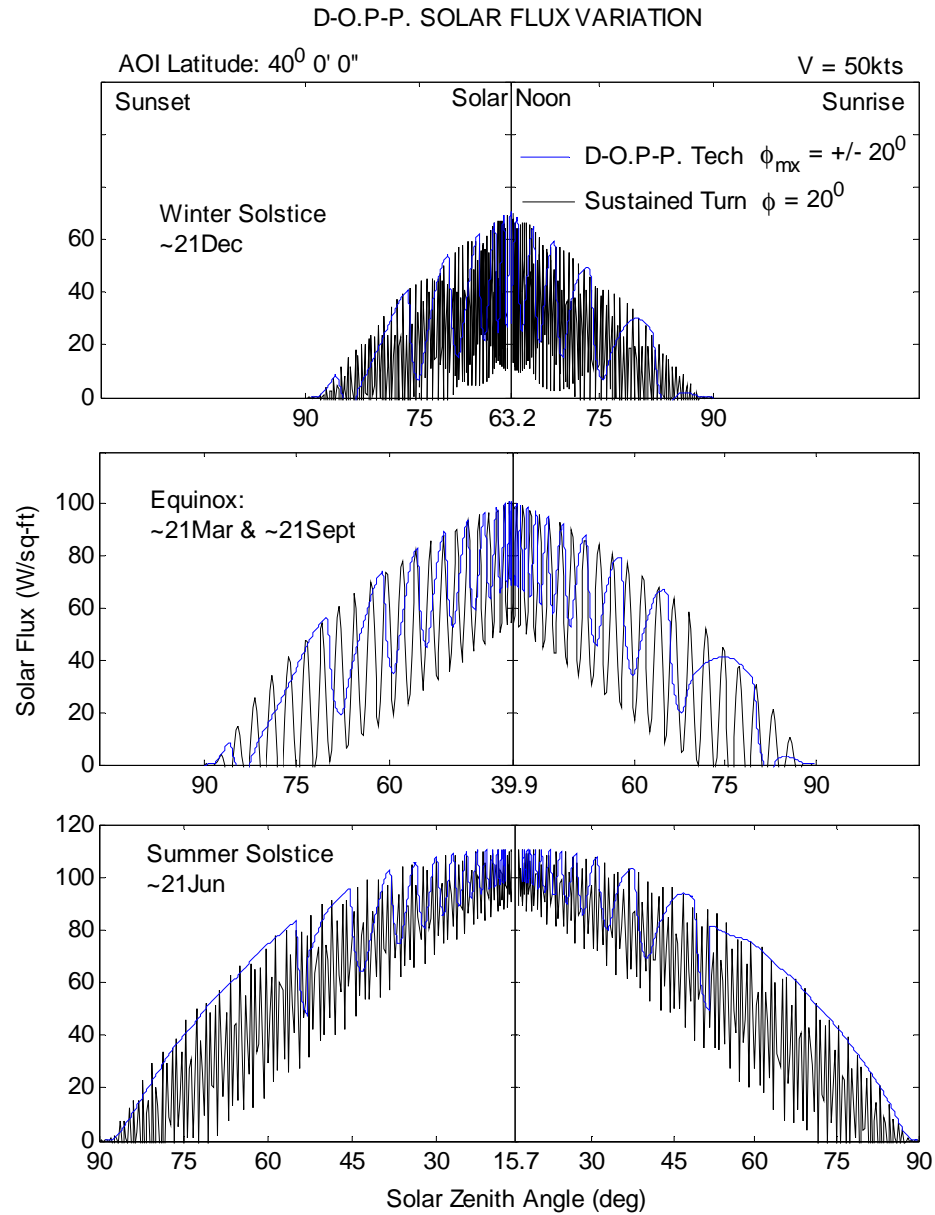


Figure 4.19: D-O.P-P. Technique Solar Flux Variation – Comparisons



Figure 4.19 shows that as the sun approaches solar noon, the vehicle's bank angle becomes more sensitive since the variation of solar flux across the 'driver' window becomes less.

Looking further into the flight trajectory, Figure 4.18, at solar noon, where the vehicle appears to be flying a long sweeping turn, is actually a series of heading adjustments as the sun progresses. This can be seen when considering a 10 minute flight window at solar noon. Figure 4.20 below shows the progression of the vehicle's bank angle and power required in order to achieve maximum solar flux or solar power, as shown in the figure.

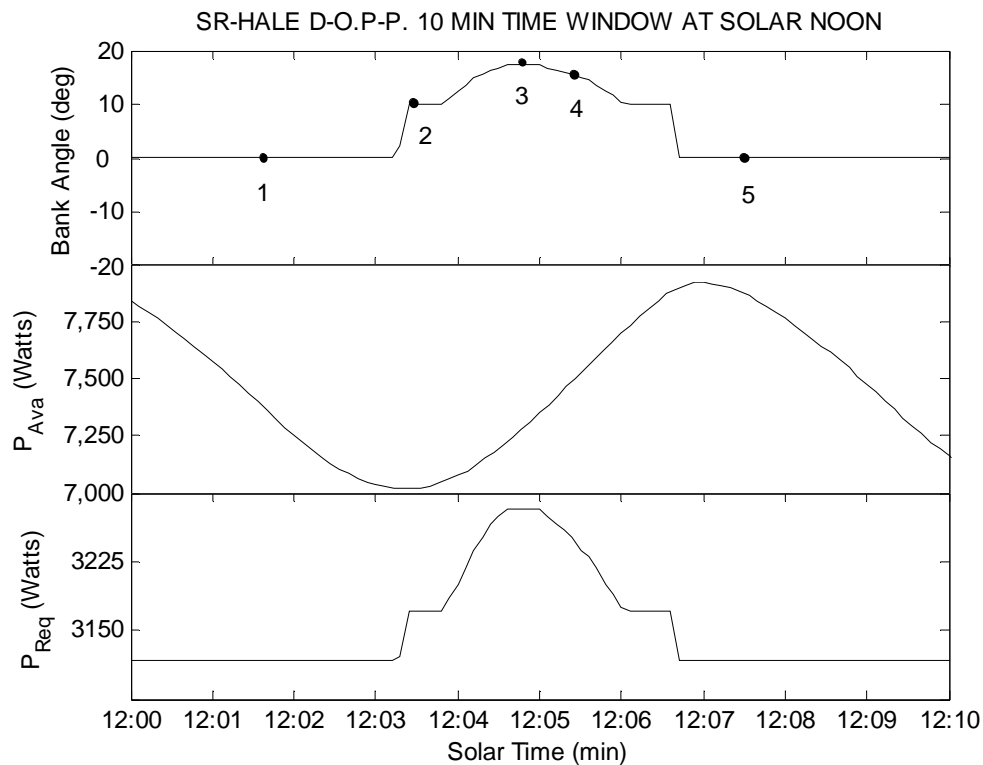


Figure 4.20: SR-HALE D-O.P-P. 10 Minute Time Window at Solar Noon

The maximum solar flux position along the 'driver' window adjusts the vehicle's heading by sweeping the bank angle from zero degrees on its original heading through 16 degrees and back, aligning the vehicle along its new direction. This process repeats throughout

mid-day, evident of the solar flux variations of Figure 4.18. The ‘driver’ windows, from -20 to +20 degrees of bank, measured solar flux for the locations marked on the 10 minute time window at solar noon are shown below in Figure 4.21. The maximum solar flux point is marked for each time location.

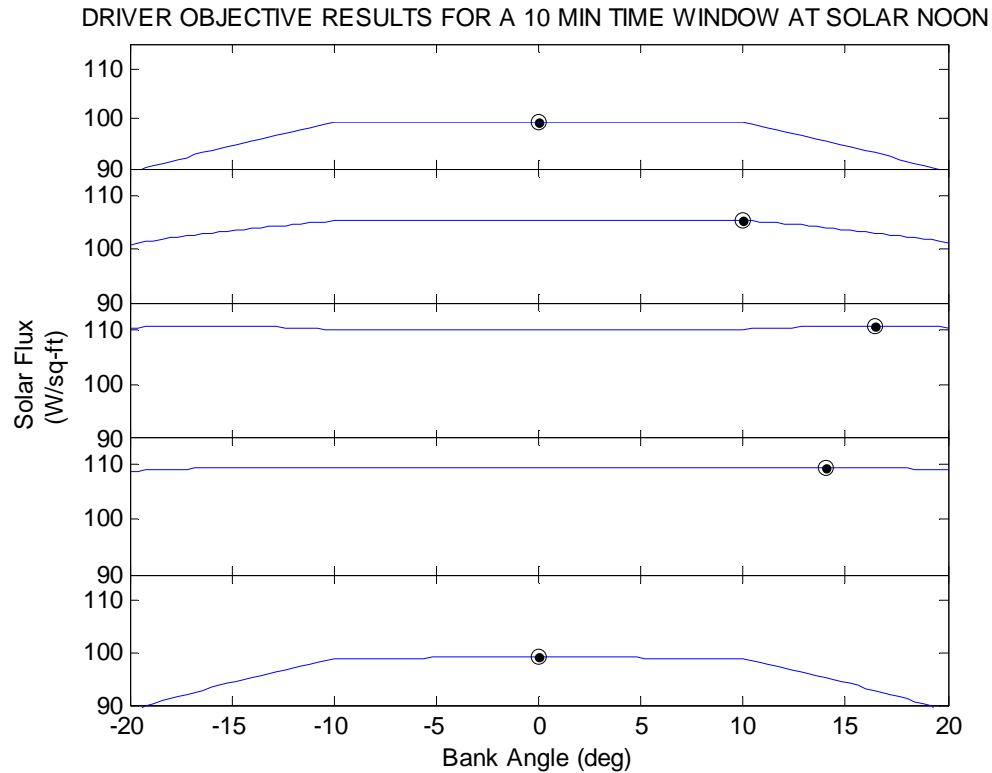


Figure 4.21 Driver Objective Results for 10 Minute Time Window at Solar Noon

Notice that as the vehicle is banking, during that time of day, the solar flux measured along the window becomes more uniform; with small differences between the vehicles condition for maximum solar flux and others in the ‘driver’ window. This is due to the location and time of day for the vehicle during the summer solstice. The effects of small differences within the flight window are more noticeable when and where geographically the solar zenith angle is small. The solar flux variations across the ‘driver’ window are more sensitive and noticeable when the zenith angle is large, like during the winter solstice over the case-study AOI.

Before continuing the analysis, consider two conditions that have an effect on the SR-HALE flight. First, determine the effects of distance in which the ‘driver’ window is projected forward of the SR-HALE UAV. The results shown above were for a projection window distance of 0.01 nautical-miles with N iterations. The effects on the maximum total available power and percent differences for varying the number of iterations is shown in Figure 4.22. The conditions shown in the figure are during the winter solstice, the worst case condition, showing the largest differences and the potential for most improvement.

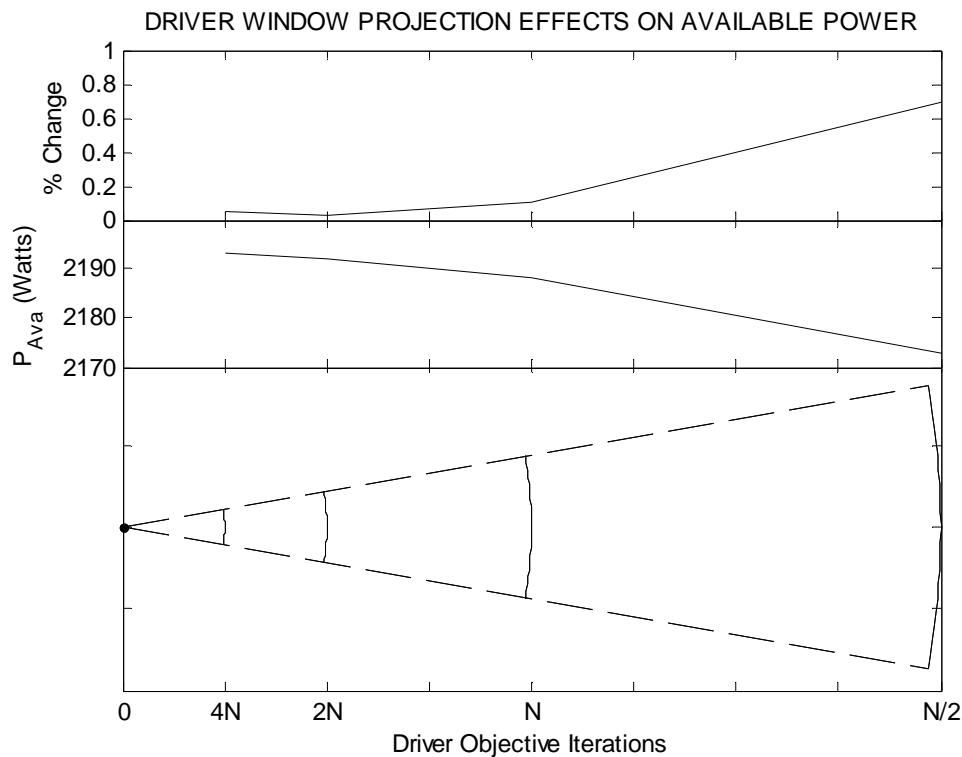


Figure 4.22: Driver Window Projection Effects on Available Power

The figure shows that with further increase in number of iterations, decreasing projection of ‘driver’ window, that the improvements determined are within less than 0.1% difference. The added computation time outweighed the minimal gain in performance. Other considerations must be accounted for when increasing the projection distance,

decreasing the number of iterations, other than the significant loss in improvement shown above. As the ‘driver’ window is projected farther, the ‘path’ for the vehicle does not become apparent; meaning, that the actual path for the vehicle to meet its destination may not be simply a sustained turn to meet its objective. For the remainder of the analysis, the projection window was maintained at its initial location.

Next, consider the effects of varying the bank angle limit for the SR-HALE UAV. Table 4.3 below shows the effects on total available solar flux and both the averaged power available and required for the flight using the D-O.P-P. Technique.

Table 4.3: Effects of Varying SR-HALE Bank Angle Limit

Columbus: Ohio: United States				
Longitude:	82 <sup>0</sup> 59' 56"	West	(-82.99889 W)	V = 50 knts
Latitude:	39 <sup>0</sup> 57' 40"	North	(39.96111 N)	
D-O-P-P. Technique		Summer Solstice	~21 June	% Increase Ava / Req
ϕ <sub>mx</sub> limit (deg)	F <sub>Total</sub> (W/sq-ft)	Ave P <sub>Ava</sub> (Watts)	Ave P <sub>Req</sub> (Watts)	
±10	11000	4325	3157	14% / 3.1% 10% / 8%
±20	12838	5065	3259	
±30	14349	5672	3530	

By increasing the bound from ±10 degrees to ±20 degrees there is a significant improvement (14%) in averaged available solar power with a relatively small increase in required power (3.1%). With further increase in bank angle limit, the tradeoff becomes less. If the vehicle structural integrity allowed for a bank angle limit of ±30 degrees, there would be a 10% improvement in available power, but subsequently an 8% increase in required power as well.

Continuing the analysis and comparisons, Table 4.4 are the summary results comparing the maximum obtainable solar power and the power required for sustained turn; and the average power required for the vehicle flying with the adaptive D-O.P-P. process. The summary results are during the equinoxes and summer and winter solstices over the case-study AOI.

Table 4.4: SR-HALE Flight Maneuvering Comparisons

Columbus: Ohio: United States				
Longitude:	82 <sup>0</sup> 59' 56" West	(-82.99889 W)	Sustained Turn $\phi$ = 20 <sup>0</sup>	50kts
Latitude:	39 <sup>0</sup> 57' 40" North	(39.96111 N)	D-O.P-P. $\phi$ = 0 <sup>0</sup> - $\pm$ 20 <sup>0</sup>	50kts
Maneuver	Averaged Available Power		Averaged Power Required	
Winter Solstice ~21Dec				
Sustained Turn	1604 W/sq-ft		3346 Watts	
D-O.P-P.	2214 W/sq-ft	27.6%	3268 Watts	-2.4%
Equinoxes ~21Mar & ~21Sept				
Sustained Turn	3221 W/sq-ft		3346 Watts	
D-O.P-P.	3838 W/sq-ft	16.1%	3259 Watts	-2.7%
Summer Solstice ~21Jun				
Sustained Turn	4093 W/sq-ft		3346 Watts	
D-O.P-P.	5100 W/sq-ft	19.7%	3280 Watts	-2.0%

The D-O.P-P. Technique increased the available solar power by 27% during the winter solstice, the time-of-year with minimum amount of daylight (09:09:00); while decreasing the power required for flight by two percent throughout the day. During the equinoxes and summer solstice similar improvements resulted, demonstrating the benefits of the path-planning technique and its application to solar regenerative high altitude long endurance surveillance flight.

The optimum flight patterns and the daily averaged solar flux / solar power gathered was analyzed and compared to the baseline sustained turn flight for an entire year over the AOI, Figure 4.23.

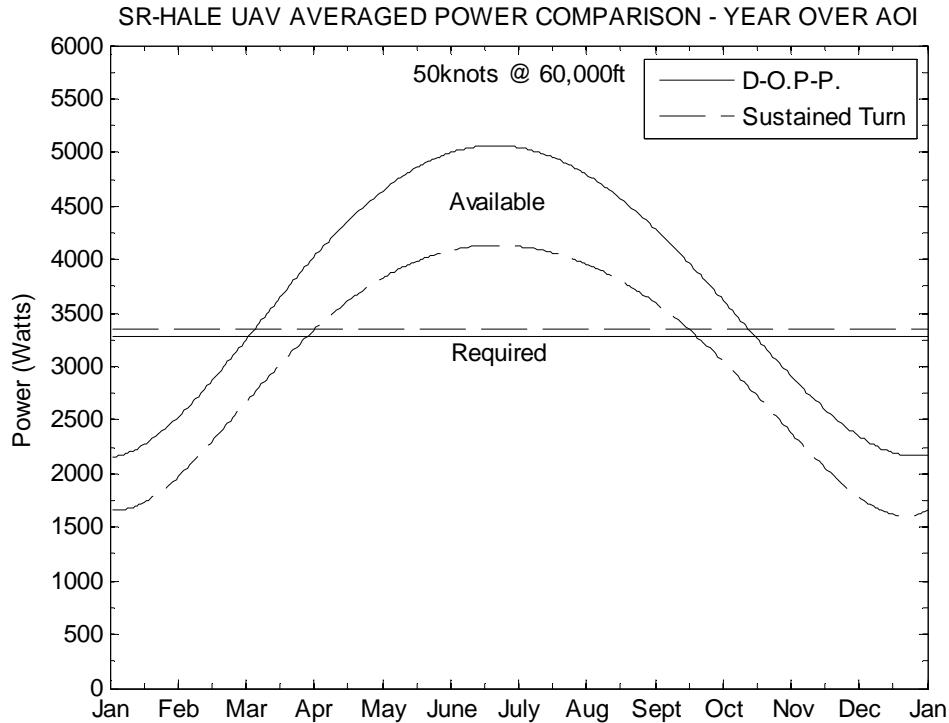


Figure 4.23: SR-HALE UAV Averaged Power Comparison – Year over AOI

For the SR-HALE UAV flying a sustained turn loiter over the AOI, the available flight time throughout the year for the vehicle to obtain enough solar power to maintain flight would be approximately between 1-April and 13-September; 165 days total. Using the D-O.P-P. Technique for generating the flight path, the available flight window over the AOI increased to total of 222 days; 4-March to 12-October. This is an additional 57 days of available flight for the year, a 26% improvement over the sustained turn loiter flight.

Similarly, the daily averaged available power for the optimum flight patterns was compared with the baseline sustained turn for variations in latitude from the equator to  $60^{\circ}$ , Figure 4.24.

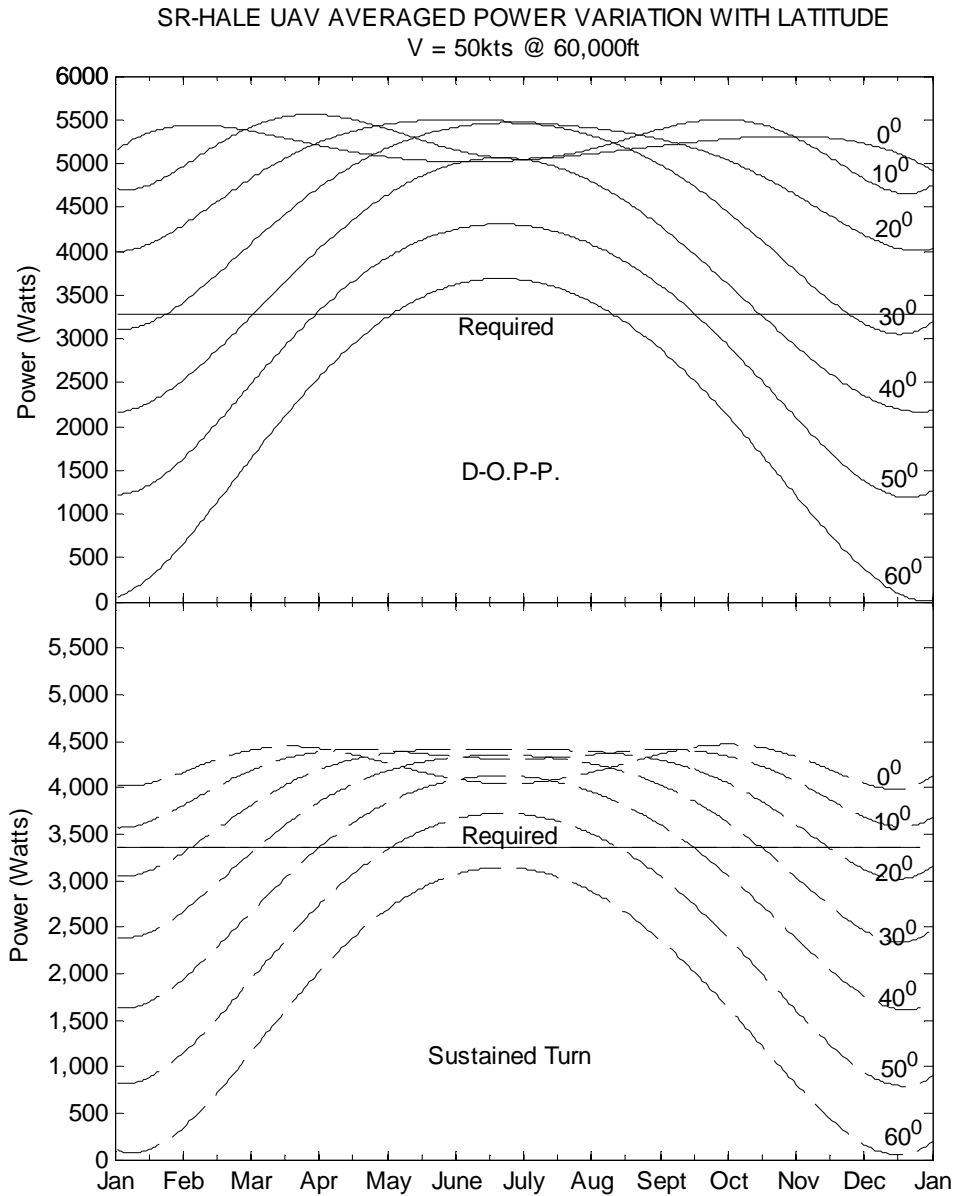


Figure 4.24: SR-HALE UAV Averaged Power Variation with Latitude

The analysis was limited to latitudes less than  $60^{\circ}$ . For latitudes greater than, there is not sufficient enough averaged available power to meet the required power for the representative SR-HALE UAV flight.

From Figure 4.24, flying a sustained turn loiter pattern was limited to  $50^{\circ}$  latitude or less. However, when flying the D-O.P-P. pattern, the vehicle is capable of increasing

the flight time at each latitude by approximately two months, including an approximate two month flight period at  $60^0$  latitude.

#### 4.3.1 High Altitude Wind Effects

Accounting for high altitude winds  $V_w$  in the SR-HALE kinematic modeling (4-1), Figure 4.25 is an example of the first hour of flight. This was compared with the still wind example (Figure 4.16) during sunrise.

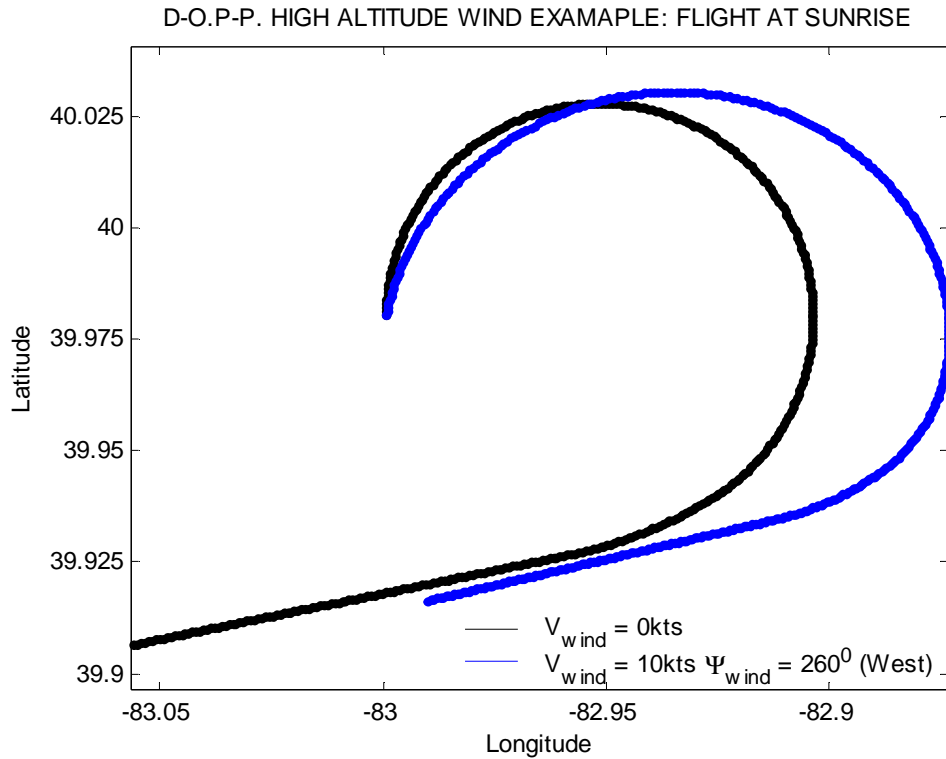


Figure 4.25: D-O.P-P. High Altitude Wind Example: Flight at Sunrise

The effects of a wind velocity of 10 knots at a W-S-W heading ( $\Psi_w = 260^0$  Inertial Earth frame) are shown – typical conditions that would be seen during the spring and summer months over the AOI. The vehicle has a Northerly-initial heading and the high altitude wind affected ‘driver’ window is shown to project the flight window, ‘pushing’ the vehicle further east. The SR-HALE UAV banks a positive 20 degrees, leaning the upper



solar panel wing surface into the sun's intensity, obtaining the maximum available solar flux during sunrise. When considering the entire day, for this example, the total solar flux available decreased (compared to Table 4.3) by -1.8%; and increased the averaged power required by less than 0.1%.

A few important comments on wind effects; First, the high altitude wind effects and the resultant available solar flux and averaged power required for SR-HALE UAV flight were determined to be a case-by-case study. There were no observable trends for either the increase or decrease in available solar flux with variations in time-of-year or high altitude wind conditions – another reason for requiring on-line adaptive capability for a high altitude solar powered flight path generation. Second, as the wind speed increased, an increase in vehicle speed was needed to compensate. For this condition, the increase in vehicle speed allowed for flexibility in vehicle movement for orientation increasing available solar power. However, this is not without the cost of increasing power required for faster flight. Finally, and most significant, there was always a noticeable increase in available solar flux for flight with D-O.P-P. process over the baseline sustained turn flight, regardless of wind conditions.

#### 4.4 SR-HALE UAV D-O.P-P. Summary

Flight while gathering solar power would benefit from on-line multi-objective optimum flight path generation capabilities to prolong the UAVs flight duration. The SR-HALE UAV case-study of optimum flight patterns for gathering solar energy was conducted to determine such benefits.

First, the requirements and limitations of solar powered flight were necessarily determined. This included ephemeris; equation of time, geocentric and local solar coordinates, surface obliquity and daylight hours. The characteristics of solar flux and the dependence on the surface location and orientation were established. Existing systems for SR-HALE UAVs were investigated that included solar panels, energy storage systems, and electric motors for powered flight. Surveillance equipment information was

gathered and used in order to set a flight window for the vehicle to maintain continual awareness. Finally, high altitude winds were defined for areas including the contiguous United States, the Norwegian Area, the Mediterranean area and Pacifica area from Alaska to Japan and surrounding regions.

A case-study location and existing equipment were established for demonstrating the requirements and limitations and UAV flight investigations. The flight mechanics of a representative SR-HALE UAV that has conducted flight tests, proving its potential for sustaining high altitude flight was also selected and defined.

Fixed flight maneuvers for the SR-HALE UAV were investigated. This was done in order to obtain a general understanding of the available solar flux for flight at a constant altitude, restricted within the flight window and to determine baseline conditions. The flight maneuvers consisted of static on-station flight, utilizing the high altitude winds; and sustained turn (circle) flight – a logical flight pattern for vehicles providing SA over an AOI or AOR. The effects of location and time-of-year were established along with the dependence of several flight variables which include: vehicle angle-of-attack, bank angle, velocity, radius of turn, heading direction or direction of flight – clockwise or counter-clockwise, as well as initial starting location (cardinal direction).

The D-O.P-P. Technique was adapted for optimizing flight paths for a SR-HALE UAVs. The objectives were to determine the minimum required power flight paths to the predetermined location and orientation for obtaining maximum solar flux. The flight path results were compared to sustained turning flight. Both still and high altitude constant wind conditions were investigated. The on-line path generation technique prolonged the flight duration by approximately two months for the year flight over the case-study AOI from the beginning of March through mid-October. This prolonged flight was consistent for all latitude locations, including two months of available flight at 60 degree latitude – where sustained turning flight was no longer capable. This was possible by increasing the averaged solar power available by as much as 26% while decreasing the averaged power required for flight.

This investigation demonstrated the potential to applying on-line optimum path generation capabilities; and the benefits for harnessing solar energy to unmanned air vehicle platforms in support of their various applications – military and civilian.

## CHAPTER 5

### ADDITIONAL D-O.P-P. TECHNIQUE APPLICATIONS

The use of the technique extends beyond solar powered UAV flight. The considerations and applicability are discussed for three environmentally-influenced flight conditions that a UAV would potentially confront.

#### 5.1 Cooperative Tactics

The cooperative tactics category of UAV-autonomy is the act of formulating an optimal sequence and spatial distribution of activities between agents in order to maximize chance of success in any given mission scenario. This would be apparent when several manned or unmanned vehicles are within the same arena providing one or multiple functions simultaneously. The D-O.P-P. Technique, under these flight conditions would be beneficial for adaptive trajectory generation of the UAV(s). The situation would require continually updated real-time information, remotely allocated to operational UAVs via the additional flight vehicles, manned or autonomous.

By relaying vehicle location, heading and flight velocity the UAVs within the vicinity could respond efficiently and adapt accordingly. The D-O.P-P. driver window would account for the other vehicle's flight conditions and determine in an adapting sequential manner the best intermediate-state parameters in order to perform the assigned task efficiently, while avoiding the potential for collision.

Further applications of the technique for cooperative (and uncooperative) tactics include the UAV in a dynamic target pursuit.

## 5.2 Dynamic Target Pursuit

Recently, a UAV has been designed with the capability for in-flight launch and recovery capability from a manned aircraft (mothership). While there have been many UAVs launched from aircraft in-flight, the capability for in-flight recovery has not been addressed. With the mothership relaying its location and flight conditions to the UAV, the vehicle could pursue, using the D-O.P-P. Technique autonomously; regardless if the mothership had to divert from its flight plan. The pursued mothership flight conditions would set the driver window for the UAV and would determine the UAV's flight path destination and orientation between intermediate-states.

In the case of UAV pursuit of an uncooperative dynamic target, an adaptive target state estimator using vision-based tracking has been developed (52). A single camera as the onboard vision sensor obtained real-time image processing to determine the relative bearing (azimuth and elevation angle). The adaptive target state estimator used a neural network augmented Kalman filter. A UAV equipped with this capability could process real-time imaging, determining the optimum D-O.P-P. Technique driver window(s) flight conditions for pursuit.

Insight into the application can be gained through considering the vehicle 'path' generation of the D-O.P-P. Technique. Using the notation in Table 2.1 with minimizing pursuit flight time, the performance index,  $J$ , is equal to the intercept time,  $T$ :

$$J = \int_0^{T_k} L dt = \int_0^T 1 dt = T \quad (5-1)$$

where the intercept time is the sum of the intermediate-state times,

$$T = \sum t_k, \quad (k = 1, \dots, N) \quad (5-2)$$

The vehicle's dynamics are adjoined to the performance index enforcing the minimum principle. Considering planar 2-D flight, the Hamiltonian, H can be formed using the vehicle dynamics shown in (4-1);

$$H(x, y, \psi, \lambda_1, \lambda_2, \lambda_3, \phi, V) = 1 + \lambda_1 V \cos \psi + \lambda_2 \sin \psi + \lambda_3 \frac{g \tan \phi}{V} \quad (5-3)$$

in still wind ( $V_w = 0$ ), where  $\lambda_i$ , ( $i = 1, 2, 3$ ) are the costates. In the presence of wind, the equations of motion can be expressed in a more compact way without the loss of generality by defining ( $\psi = 0$ ) in the direction of the wind and normalizing (18). The control constraints would be applied to the vehicles bank angle and speed.

The first and second order necessary and sufficient conditions for optimality of the Hamiltonian are dependent on the nature of the constraints. The conditions are explained in detail and listed in references (11-13). The intermediate-states initial and final boundary conditions for the D-O.P-P. Technique for this application are:

$$[\mathbf{x}(t_0)] = \begin{bmatrix} x(t_0) \\ y(t_0) \\ \psi(t_0) \end{bmatrix} = \begin{bmatrix} x_{k-1}^*(t_{k-1}) \\ y_{k-1}^*(t_{k-1}) \\ \psi_{k-1}^*(t_{k-1}) \end{bmatrix} = [\mathbf{x}_{k-1}^*(t_{k-1})], \quad (5-4)$$

$$[\mathbf{x}(t_f)] = \begin{bmatrix} x(t_f) \\ y(t_f) \\ \psi(t_f) \end{bmatrix} = \begin{bmatrix} x_k^*(t_k) \\ y_k^*(t_k) \\ \psi_k^*(t_k) \end{bmatrix} = [\mathbf{x}_k^*(t_k)]$$

The initial and final boundary condition would continually update and adapt on-line for the UAV in pursuit of the dynamic target until intercept.

The insight into the ‘path’ generation of the technique can also be applied to UAV flight in evading potential threats, where minimizing the obstacle avoidance flight time is of the essence.

### 5.3 Threat Evasion

With the increase of UAV flight in low altitude regimes of the battlefield, the possible threat to the UAV is inevitable. Work has been done investigating threat evasion techniques, specifically in defeating radar detection (45). The path-planning for unmanned combat air vehicles (UCAVs) in the presence of a surface-to-air missiles, requires the interaction between three subsystems; the UCAV, radar, and the missile. The integrated model features for the aircraft radar cross section (RCS) depends explicitly on the both the aspect and bank angles, hence coupled to the aircraft dynamics.

Numerous threat avoidance algorithms exist. Some make use of the search techniques, such as A\* to search pre-computed cost grid of the terrain. The D-O.P-P. Technique on-line efficiency would benefit the required fast response situation by eliminating the significant size in cost grid decision space required for off-line path search techniques. Due the nature of the RCS, by decoupling, letting the ‘driver’ condition determine the intermediate-state aspect and bank angle; and the ‘path’ contain minimal flight time, could prove to be advantageous.

## CHAPTER 6

### SUMMARY AND CONCLUSION

The following introduced a multi-objective (D-O.P-P.) technique for UAV path and trajectory autonomy generation, through task allocation and sensor fusion. The dynamic optimization technique generates on-line adaptive flight paths for UAVs based on available flight windows and environmental influenced objectives. The real-time path generation for UAVs considered multiple independent conflicting objectives without the necessity of developing artificial parameters. The on-line process was locally-optimal based and adaptive, reducing the significant size in decision space required for off-line path search techniques. The technique was not limited to individual methods or path planning algorithms, however, certain procedures, like A\* search, proved advantageous in real-time analysis.

Solar powered high altitude long endurance flight was investigated as a case-study of the D-O.P-P. Technique. A representative SR-HALE UAV, comparable to the Aerovironment Pathfinder, was defined and flight mechanics used; and a case-study example location in which to support continual SA was chosen. The case-study location details can be seen in Table 2.2 and Table 3.2. The SR-HALE UAV was limited to a constant altitude of 60,000 feet and high altitude winds for the AOI were considered. At that altitude the range-of-sight, i.e. the limited geographical flight window, was determined by the HISAR wide-area sensor system that has been used by surveillance aircraft at that altitude. The HISAR sensor system and the determined flight constraint window assured continual SA over the AOI or AOR, as seen in Figure 3.6. Solar panels, covering 80% of the upper UAV wing surface, electric motors, and energy storage



system were selected based on existing flight test demonstrated equipment – along with SR-HALE platform flight mechanics. The SR-HALE UAV performance characteristics and overall platform summary are shown in Figure 3.8 and Tables 3.5 and 3.6, respectively.

Fixed flight maneuvers for the SR-HALE UAV was analyzed first, to understand the effects of location, time-of-year and flight vehicle conditions; and to obtain a baseline for direct comparisons of the D-O.P-P. Technique. The first fixed flight condition considered was to utilize the high altitude winds by heading directly into the wind to obtain static on-station flight. The available solar flux was determined with the vehicle heading in the four main cardinal directions and for angles-of-attack up to 15 degrees for all latitudes and case-study location. For the case-study location high altitude wind conditions, it was determined that the SR-HALE UAV could not sustain static on-station constant altitude flight during the summer months; and only during 40 knot plus winds and more than 12 hours of available daylight – limiting the fixed flight maneuver.

The second fixed flight maneuver considered was the sustained turn loiter flight. Circle flight patterns are logical choice for persistent ISR vehicles and were selected as a baseline for comparisons. Sustained turn analysis consisted of varying location and time-of-year as well as the SR-HALE UAVs bank angle, flight velocity (revolutions per daylight), turn radius, direction of flight, and initial starting cardinal location. The variation of each flight condition was individually considered to determine the trends, if any; and their effects for solar powered flight. It was shown, as expected that the latitude location and time-of-year varied the available solar flux significantly. The other, vehicle dependent flight conditions were determined over the case-study AOI. It was determined that variations in flight velocity and the turning radius trends were consistent, a result that was utilized not only in determining baseline conditions but in D-O.P-P. modeling and analysis as well.

The objectives of the D-O.P-P. Technique were to determine the minimum required power flight paths to the predetermined location and orientation for obtaining maximum solar flux established by the ‘driver.’ This was done for still wind and constant wind conditions at altitude over the AOI and the variations in latitude. The SR-

HALE UAV kinematics was used to develop the flight maneuvering window and was constrained by a maximum bank angle of 20 degrees. It was determined that minimum power required occurred at the vehicles stall speed. To account for this the flight velocity was set to a constant 50 knots, 20% safety margin; while maintaining minimum power required. The projection of the flight window was set at one nautical-mile, assuring sufficient response time of the vehicle. The D-O.P-P. Technique in its general form can be seen in Table 2.1; and applied for solar powered flight with the SR-HALE UAV in Table 4.2. The vehicles flight maneuvering window can be seen in Figure 4.16.

The path-planning technique increased the total available solar flux by 10 to 20% and decreased the average power required for flight compared to the baseline sustained turn loiter flight for the case-study AOI over the time span of one year. This increased the total flight time over the AOI throughout the year by an additional 57 days, a 26% improvement over the baseline loiter flight. Considering latitude variations from the equator through 60 degrees, the technique increased the available flight time consistently by an approximate two months; including flight at 60 degree latitude where baseline flight was unattainable. These results can be seen in Figures 4.20 and 4.21. Finally, in terms of the example case-study, when considering high altitude wind effects, showed that the physical flight path was altered and that there were no noticeable trends – supporting the required on-line capability for such vehicles. However, regardless if high altitude wind effects were considered the D-O.P-P. Technique improved the flight capability over the baseline conditions.

Other applications of the D-O.P-P. Technique was discussed, that demonstrated the versatility of the process. These included, but not limited to, cooperative tactics between the UAV and other acting agents, the UAV in dynamic target pursuit, as well as evading potential threats. Each was discussed briefly, including the relevance and benefits the technique could provide for the selected scenarios.

In summary, the D-O.P-P. Technique provides an on-line real-time adaptive multi-objective environmentally influenced path-planning process for UAV-autonomy, through task allocation; eliminating the use of artificial parameters and reducing the

decision space. The potential of the technique was demonstrated through the application to the advancing field of solar-regenerative high altitude long endurance flight.

## LIST OF REFERENCES

1. Trefz, John L. Jr., "From Persistent ISR to Precision Strikes: The Expanding Role of UAVS" LCDR, U.S. Navy, Navy War College, Newport, R.I., May 2003.
2. "Unmanned Aerial Vehicle" from Wikipedia, the free encyclopedia ([http://en.wikipedia.org/wiki/Unmanned\\_air\\_vehicle](http://en.wikipedia.org/wiki/Unmanned_air_vehicle)), 15-April-2009.
3. Mittal, S., Deb, K. "Three-Dimensional offline Path Planning for UAVs Using Multiobjective Evolutionary Algorithms" Indian Institute of Technology Kanpur, India.
4. Weider, S. "An Introduction to Solar Energy for Scientists and Engineers" John Wiley & Sons, 1982.
5. Alemayehu, D. Eaton, E. Faruque, I., "HALE UAV: Aerovironment Pathfinder: Aerodynamic and Stability Analysis, Case-Study: Planform Optimization", ([http://www.aoe.vt.edu/~mason/Mason\\_f/pathfinder.pdf](http://www.aoe.vt.edu/~mason/Mason_f/pathfinder.pdf))
6. Pearson, J., Gregorek, G.M., Whitfield C.A., "High Altitude Morphing Aircraft (HAMAC)" AFRL-VA-WP-TR-2007-XXX– Final Report to USAF for Phase I Small Business Initiative, 2007.
7. "Global Hawk" Sensor Packages. Wikipedia. ([www.wikipedia.com](http://www.wikipedia.com)), 1-December-2008.
8. Strganac, T.W. "Wind Study for High Altitude Platform Design" NASA-RP-1044, N80-12661, December 1979.
9. Klesh, A.T., Kabamba, P.T., "Energy-Optimal Path Planning for Solar-Powered Aircraft in Level Flight" AIAA Guidance, Navigation and Control Conference and Exhibit" Hilton Head SC, 20-23 August 2007.
10. "Pathfinder and the Development of Solar Rechargeable Aircraft" E&TR July 1994. Department of Defense's Ballistic Missile Defense Organization. Contacts: Colella, N.J. or Wennecker, G.S. (LLNL, Carnegie Mellon University).

11. Arora, J.S., "Introduction to Optimum Design" Elsevier Academic Press, San Diego CA, 2004.
12. Bryson, A.E. Jr. "Dynamic Optimization" Addison-Wesley Longman Inc., Menlo Park CA, 1999.
13. Bryson, A.E. Jr., Ho, Y-C. "Applied Optimal Control: Optimization, Estimation, and Control" Taylor and Francis Group, New York, NY, 1975.
14. Deb, K. "Optimization for Engineering Design: Algorithms and Examples" New Delhi, Prentice Hall, 1995.
15. Nickol, Craig L. et. al., "High Altitude Long Endurance UAV Analysis of Alternatives and Technology Requirement Development" NASA/TP-2007-214861, March 2007.
16. Hall, D.W., Watson, D.A., Tuttle, R.P., Hall, S.A., "Mission Analysis of Solar Powered Aircraft" NASA Contractor Report 172583, July, 1985.
17. Reda, I., Andreas, A., "Solar Position Algorithm for Solar Radiation Applications" NREL/TP-560-34302, January 2008.
18. McGee, T.G., Spry, S., Hedrick, K., "Optimal Path Planning in a Constant Wind with a Bounded Turning Rate" Center for Collaborative Control for Unmanned Vehicles, University of California, Berkeley, CA.
19. McGee, T.G., Hedrick, K., "Optimal Path Planning with a Kinematic Airplane Model" Journal of Guidance, Control, and Navigation, Vol. 30 No. 2, March-April 2007.
20. Bestaoui, Y., Dahmani, H., Belharet, K., "Geometry of Translational Trajectories for an Autonomous Aerospace Vehicle with Wind Effect" 47<sup>th</sup> AIAA Aerospace Sciences Meeting Including The New Horizons Forum and Aerospace Exposition, Orlando, FA, 5-8 January 2009.
21. Shapira, I., Ben-Asher, J.Z., "Near-Optimal Horizontal Trajectories for Autonomous Air Vehicles" Journal of Guidance, Control, and Navigation, Vol. 20, No. 4, July-August 1997.
22. Erzberger, H., Lee, H., "Optimum Horizontal Guidance Techniques for Aircraft" Journal of Aircraft, Vol. 8, No. 2, February 1971.
23. Tsitsiklis, J.N. "Efficient Algorithms for Globally Optimal Trajectories" IEEE Trans. on Automatic Control, Vol. 40, No. 9, Sept 1995.

24. McManus, I.A., Walker, R.A. "Multidisciplinary Approach to Intelligent Unmanned-Airborne-Vehicle Mission Planning" *Journal of Aircraft*, Vol. 43, No. 2, March-April 2006.
25. Fahroo, F., Ross, I.M. "Direct Trajectory Optimization by a Chebyshev Pseudospectral Method" *Journal of Guidance, Control, and Dynamics*, Vol. 25, No. 1, January-February 2002.
26. Dogan, A., "Probabilistic Path Planning for UAVs", 2<sup>nd</sup> AIAA "Unmanned Unlimited" Systems, Technologies, and Operations, San Diego, CA, 15-18 September, 2003.
27. Lennon, J.A., Atkins, E.M., "Optimal Path-Planning with Behavior Based Cost Definition" AIAA 1<sup>st</sup> Intelligent Systems Technical Conference, Chicago, IL, 20-22 September, 2004.
28. Amin, J.N., Boskovic, J.D., Mehra, R.K., "A Fast and Efficient Approach to Path Planning for Unmanned Vehicles" AIAA Guidance, Navigation, and Control Conference and Exhibit, Keystone, CO, 21-24 August, 2006.
29. Geiger, B.R., Horn, J.F., DeLullo, A.M., Long, L.N., "Optimal Path Planning of UAVs Using Direct Collocation with Nonlinear Programming" AIAA Guidance, Navigation, and Control Conference and Exhibit, Keystone, CO, 21-24 August, 2006.
30. Geiger, B.R., Horn, J.F., "Neural Network Based Trajectory Optimization for Unmanned Aerial Vehicles" 47th AIAA Aerospace Sciences Meeting Including The New Horizons Forum and Aerospace Exposition, Orlando, FL, 5-8 January 2009.
31. Narayan, P., Campbell, D., Walker, R., "Multi-Objective UAS Flight Management in Time Constrained Low Altitude Local Environments" 46<sup>th</sup> AIAA Aerospace Sciences Meeting and Exhibit, Reno, NV, 7-10 January 2008.
32. Yokoyama, N., Ochi, Y., "Optimal Path Planning for Skid-to-Turn Unmanned Aerial Vehicle" AIAA Guidance, Navigation, and Control Conference and Exhibit, Honolulu, Hawaii, 18-21 August 2008.
33. Rippel, E., Bar-Gill, A., Shimkin, N., "Fast Graph-Search Algorithms for General Aviation Flight Trajectory Generation" Technion - Israel Institute of Technology, Israel.
34. Chang, W., Hsiao, F., Sheu, D., "Two-Point Flight Path Planning Using a Fast Graph-Search Algorithm" *Journal of Aerospace Computing, Information, and Communication*, Vol. 3, September 2006.

35. Schwartzenruber, L., Foo, J.L., Winer, E.H. "Three-Dimensional Multi-Objective UAV Path Planner Using Meta-Paths for Decision Making and Visualization" 12<sup>th</sup> AAIA/ISSMO Multidisciplinary Analysis and Optimization Conference, Victoria, British Columbia Canada, 10-12 September 2008.
36. Miele, A., Lee, Y.L., Wu, G.D., "Optimal Trajectories for an Aerospace Plane, Part 1: Formulation, Results, and Analysis" Aero-Astronautics Report No. 247, Rice University, 1990.
37. Chieng, W-Y., "The Study of Flight Path Planning for Multiple Target Visitations", Dissertation, Aeronautics & Astronautics, etd-0613107-115826.
38. Frazzoli, E., Dahleh, M.A., Feron, E., "Real-Time Motion Planning for Agile Autonomous Vehicles" Journal of Guidance, Control, and Navigation, Vol. 25, No. 1, January-February, 2002.
39. Pongpunwattana, A., Rysdyk, R., "Real-Time Planning for Multiple Autonomous Vehicles in Dynamic Uncertain Environments" University of Washington, Seattle, WA.
40. Richards, N., Sharma, N., Ward, D. "A Hybrid A\*/Automaton Approach to On-Line Path Planning with Obstacle Avoidance" AIAA 1st Intelligent Systems Technical Conference, Chicago IL, 20-22 September 2002.
41. Howlett, J.K., McLain, T.W., Goodrich, M.A., "Learning Real-Time A\* Path Planner for Unmanned Air Vehicle Target Sensing" Journal of Aerospace Computing, Information, and Communication, Vol. 3, March 2006.
42. Rathbun, D., Capozzi, B., "Evolutionary Approaches to Path Planning Through Uncertain Environments" AIAA's 1st Technical Conference and Workshop on Unmanned Aerospace Vehicles, Portsmouth VA, 20-23 May 2003.
43. Pettit, R.L., Homer, M.L., "An Autonomous Threat Evasion Response Algorithm for Unmanned Air Vehicles During Low Altitude Flight" AIAA 1st Intelligent Systems Technical Conference, Chicago IL, 20-22 September 2004.
44. Geyer, M.S., Johnson, E.N., "3D Obstacle Avoidance in Adversarial Environments for Unmanned Aerial Vehicles" AIAA Guidance, Navigation, and Control Conference and Exhibit, Keystone CO, 21-24 August 2006.
45. Kabamba, P.T., Meerkov, S.M., Zeitz III, F.H., "Optimal Path Planning for Unmanned Combat Aerial Vehicles to Defeat Radar Tracking" Journal of Guidance, Control, and Navigation, Vol. 29, No. 2, March-April 2006.

46. Park, J.B., Vorsmann, P., "Strategies for the Implementation of a Sense and Avoid System for Unmanned Air Vehicles" 3<sup>rd</sup> US-European Competition and Workshop on Micro Air Vehicle Systems & European Micro Air Vehicles, Conference and Flight Competition, Toulouse, France, 17-21 September 2007
47. Tooren, J., Heni, M., Knoll, A., Beck, J., "Development of an Autonomous Avoidance Algorithm for UAVs in General Airspace" EADS Defense & Security, Military Air Systems, D-18663 Munchen, Germany.
48. Jorris, T.R., Cobb, R.G., "Multiple Method 2-D Trajectory Optimization Satisfying Waypoints and No-Fly Zone Constraints" Journal of Guidance, Control, and Dynamics, Vol. 31, No. 3, May-June 2008.
49. Zengin, U., Dogan, A., "Dynamic Target Pursuit By UAVs In Probabilistic Threat Exposure Map" AIAA 3rd Unmanned Unlimited Technical Conference, Workshop and Exhibit, Chicago IL, 20-23 September 2004.
50. Caveney, D.K., Hedrick, J.K., "Path Planning for Targets in Close Proximity with a Bounded Turn-Rate Aircraft" AIAA Guidance, Navigation, and Control Conference and Exhibit, San Francisco CA, 15-18 August 2005.
51. Maj. Burns, B.S., Maj. Blue, P.A., Capt. Zollars, M.D., "Simulation of Real-Time Trajectory Generator For Automated Aerial Refueling with a Required Time of Arrival" AIAA Modeling and Simulation Technologies Conference and Exhibit, Hilton Head SC, 20-23 August 2007.
52. Sattigeri, R.J., Johnson, E., Calise, A.J., Ha, J., "Vision-based Target Tracking with Adaptive Target State Estimator" AIAA Guidance, Navigation and Control Conference and Exhibit, Hilton Head SC, 20-23 August 2007.
53. Cloutier, J.R., Lin, C.F., Yang, C., "Maneuvering Target Tracking VIA Smoothing and Filtering Through Measurement Concatenation" AIAA-91-2698-CP.
54. Han, J.D., Campbell, M., "Artificial Potential Guided Evolutionary Path Plan for Target Pursuit and Obstacle Avoidance" AIAA Guidance, Navigation, and Control Conference and Exhibit, Austin TX, 11-14 August 2003.
55. 1<sup>st</sup> Lt Larson, R.A., Mears, M.J., Maj. Blue, P.A., "Path Planning for Unmanned Air Vehicles to Goal States in Operational Environments" AIAA Infotech@Aerospace, Arlington VA, 26-29 September 2005.
56. Ousingsawat, J., Campbell, M.E., "On-line estimation and path planning for multiple vehicles in an uncertain environment" International Journal of Robust and Nonlinear Control, 2004.



57. Harl, N., "Coordinated Rendezvous of Unmanned Air Vehicles to a Formation: A Sliding Mode Approach" AIAA Guidance, Navigation and Control Conference and Exhibit, Honolulu Hawaii, 18-21 August 2008.
58. Bollino, K.P., Lewis, L.R., "Collision-free Multi-UAV Optimal Path Planning and Cooperative Control for Tactical Applications" AIAA Guidance, Navigation and Control Conference and Exhibit, Honolulu Hawaii, 18-21 August 2008.
59. Boissonnat, J.D., Cerezo, A., Leblond, J., "Shortest Paths of Bounded Curvature in the Plane" Journal of Intelligent and Robotic Systems" Kluwer Academic Publishers, Netherlands, 1994.
60. Mahmoudian, N., Woolsey, C.A., Geisbert, J., "Steady Turns and Optimal Paths for Underwater Gliders" AIAA Guidance, Navigation and Control Conference and Exhibit", Hilton Head SC, 20-23 August, 2007.
61. Gregorek, G.M., Gregorek, C., Bowen, F., Whitfield, C.A., "An Initiative to Produce Unmanned Air Vehicles in Ohio" *Confidential*, Orion America Technologies, LLC, March 2009.
62. Swartzentruber, L., Foo, J.L., Winer, E.H., "Three-Dimensional Multi-Objective UAV Path Planner using Terrain Information" AIAA/ASME/ASCE/ASC Structures, Structural Dynamics, and Materials Conference, Palm springs, California, 4-7 May 2009.
63. Foo, J.L., Knutzon, J.S., Oliver, J.H., Winer, E.H., "Three-Dimensional Multi-Objective Path Planning of Unmanned Aerial "Vehicles using Partial Swarm Optimization" AIAA/ASME/ASCE/ASC Structures, Structural Dynamics, and Materials Conference, Honolulu Hawaii, 23-16 April 2007.
64. Google Earth: Explore, Search, and Discover (<http://earth.google.com/>)
65. Hishinuma, Y., Chikahasa, T., Kagami, F., Ogawa, T., " The Design and Performance of a PEFC at a Temperature Below Freezing" JSME International Journal, Series B, Vol. 47, No. 2, 2004.

## APPENDIX

The D-O.P-P. Program Interface is shown below. The program was developed in MatLab R2008a and run on a Microsoft Window XP Professional Version 2002 operating system with an Intel® Core™2 CPU 6320 at 1.86GHz, 2.00 GB of RAM.

The program has six subroutines corresponding to the flow chart shown in Figure 4.15. The first subroutine (independent) is a user defined AOI location for continual SA, from which the range-of-sight is determined. The second subroutine (independent) builds the projected flight window for the ‘driver’ objective from the user defined UAV’s flight mechanics. The high altitude winds and initial location of the vehicle are inputted, and the D-O.P-P. Technique is implemented. The flight window is transformed into geocentric coordinates and the solar flux is determined throughout the possible destination for the vehicle corresponding to that instant in time. A separate subroutine determines the ‘local’ optimum within the transformed flight window results. The necessary destination conditions are then passed on for the development of the UAV’s optimum ‘path’ from its initial location to destination. This process is iterated from sunrise through sunset for the SR-HALE UAV.

The D-O.P-P. program’s computational time is less than order ( $N/10$  (seconds)), where  $N$  is the number of ‘driver’ iterations.  $N$  is determined on the projection distance of the ‘driver’ objective flight window and the UAV’s flight mechanics over the entire duration of flight. For the given example case-study and on the summer solstice (14:53:24), with a projection window of 0.1 nautical-miles, corresponded to 7,423 iterations.

```

%*** D-O-P-P. TECHNIQUE *****

%*****

%*** SR-HALE APPLICATION *****

%*** AREA OF INTEREST *****
n1=172; % [days] # of days from Jan 1
LonglocAOI=-82.9989; % [deg] (Case Study: Columbus Ohio)
LatlocAOI=39.9611; % [deg] (Case Study: Columbus Ohio)
LongstAOI=-75.0000; % [deg] (Case Study: Standard Meridian)
[Td1,ts,n2,AOIcoD,AOIcoL] = AOI(n1,LonglocAOI,LatlocAOI,LongstAOI);

%*** FLIGHT CONDITIONS AND FLIGHT WINDOW *****
pitch=10; % [deg] Cruise Pitch Angle
phimx=20; % [deg] Maximum Bank Angle
RFW=.1; % [nm] Projection of Driver Window
Vcruise=150; % [kts] Cruise True Velocity
[x_w,y_w,sigma_w,t_w,sigma_dot,Phi_w,T,time_i] =
FlightWindow(phimx,RFW,Vcruise,ts);

%*** HIGH ALITITUDE WINDS *****
Vwind=0; % [kts] Wind Velocity
Sigmawind=260; % [deg] Wind Heading Angle (Earth
frame)

%*** INTIAL LOCATION AND HEADING AT SUNRISE *****
Longloc_i=-82.9989; % [deg] Initial Vehicle Longitude
Latloc_i=39.9611; % [deg] Initial Vehicle Latitude
sigma_i=180; % [deg] Initial heading (Flight Coord)

%*** D-O-P-P. TECHNIQUE *****
for k=1:(time_i);
[sigma_k,Longloc_k,Latloc_k,Obliq,Z_k,step] =
DriverWindow(LonglocAOI,LatlocAOI,RFW,Longloc_i,Latloc_i,sigma_i,sigma_
dot,n2,theta,Phi_w,x_w,y_w,sigma_w,t_w,T,k,Vwind,Sigmawind);

%*** SOLAR FLUX (INTENSITY) *****
[Fdir] = SolarFlux(Obliq,Z_k,step);

%*** DRIVER *****
%*** MAXIMUM SOLAR FLUX/POWER AVAILABLE & LOC/ORIENT *****
[Fdir_mx,Wava_max,xk] = Driver(Fdir);

%*** PATH *****
%*** MINIMUM POWER REQUIRED FOR FLIGHT *****
[Wreq_mn] = Path(xk);
end
%*****

```